Development of an interface thickening method for the direct numerical simulation of compressible liquid-vapor flows in the framework of the Second Gradient theory

Davy Nayigizente, Sebastien Ducruix, Schmitt Thomas

To cite this version:

Davy Nayigizente, Sebastien Ducruix, Schmitt Thomas. Development of an interface thickening method for the direct numerical simulation of compressible liquid-vapor flows in the framework of the Second Gradient theory. Physics of Fluids, 2021, 33 (5), pp.052119. 10.1063/5.0048715. hal-03319859

HAL Id: hal-03319859

https://hal.science/hal-03319859v1

Submitted on 13 Aug 2021

HAL is a multi-disciplinary open access archive for the deposit and dissemination of scientific research documents, whether they are published or not. The documents may come from teaching and research institutions in France or abroad, or from public or private research centers.

L'archive ouverte pluridisciplinaire **HAL**, est destinée au dépôt et à la diffusion de documents scientifiques de niveau recherche, publiés ou non, émanant des établissements d'enseignement et de recherche français ou étrangers, des laboratoires publics ou privés.

ACCEPTED MANUSCRIPT

Physics of Fluids

This is the author's peer reviewed, accepted manuscript. However, the online version of record will be different from this version once it has been copyedited and typeset.

PLEASE CITE THIS ARTICLE AS DOI: 10.1063/5.0048715

AIP Publishing

Development of an interface thickening method for the direct numerical simulation of compressible liquid-vapor flows in the framework of the Second Gradient theory

Davy Nayigizente,[1, a)] Sébastien Ducruix,[1] and Thomas Schmitt[1, b)]
Laboratoire EM2C, CNRS, CentraleSupélec, Université Paris-Saclay
3, rue Joliot Curie, 91192 Gif-sur-Yvette cedex, France

(Dated: 3 May 2021)

This study presents a method to perform Direct Numerical Simulation (DNS), in the sense of turbulence, of two-phase flows with interfaces. It is based on the compressible diffuse interface model introduced by the Second Gradient theory. This model assumes a continuous variation of the thermodynamic variables in the interface and add to their description a dependency on the density gradient. The interface widths as predicted by the model fall way below the typical relevant turbulent scales. We propose here a thermodynamically consistent method to thicken the interface in order to perform calculations on typical DNS meshes. The modified model has been integrated and validated on canonical configurations. It has then been applied to more complex cases such as colliding three-dimensional droplets and the break-up of two-dimensional liquid jets.

Contemporary propulsion devices operate over ever growing ranges of temperature and pressure. Their investigation has become essential from economical, ecological as well as safety stand points. Different thermodynamic regimes are usually encountered in these systems thus complicating their study. In that prospect, numerical simulation stands as powerful tool with promising results, even if a large margin for improvement still remains.

The severe changes in thermodynamic regime likely to occur in devices like Diesel engines during compression, aeronautical engines during takeoff or rocket engines during ignition are one major cause of difficulty. To focus on the latter system, rocket engines, in particular cryogenic ones, mostly work in transcritical and supercritical conditions i.e. the pressure or the temperature for transcritical regimes or both for supercritical regimes exceed their critical values. Such regimes are usually treated with the use of appropriate equations of state (EoS) accounting for the non-ideality of the fluid and the invalidity of the assumptions used to derive the ideal gas law. The study of so called real gas flows in combustion chambers is still an active field of research, see 1–6. However, during the early moments of the ignition, fuel is injected at subcritical pressures often leading to the presence of a liquid phase, which necessitates an additional treatment to deal with two-phase flow effects such as the presence of interfaces, capillary phenomena and phase change. Two-phase flow models are usually separated in two classes with a distinct handling of the interface geometry and thermodynamics.

Sharp Interface Methods (SIM) consider the interface as a discontinuity that must be accurately located during the simulation. They are comprised of two main approaches. Interface tracking methods such as Arbitrary Lagrangian-Eulerian in 7 and 8, Boundary Integrals from 9 and 10, Front-Tracking by 11 and 12 or Marker-And-Cell of 13 and 14 rely on a specific mesh deforming with the flow or Lagrangian vortices/markers advected with the flow to locate its different constituents. These methods are usually extremely accurate for small and regular movements of the interface but struggle to deal with large scale and complex topological changes, in particular interface break-up and reconnection. In modern literature, interface capturing methods are often favored over the former, the most commonly used being the Level-Set 15 and 16 and the Volume-of-Fluid (VOF) 8 and 17 methods. Level-Set methods represent the interface as an iso-surface of the so-called level-set function, usually a signed distance function. Early Level-Set methods offered a simple yet precise representation of the interface topology but lacked conservative properties. Since then, several improvements have been made to achieve conservative Level-Set methods such as in 18 and 19. VOF methods reconstruct the interface geometry using a phase volume fraction advected on the computational mesh. They tend to offer better conservative properties than Level-Set methods but the interface reconstruction procedure displays an important complexity that grows rapidly with the dimension of the problem, the topology changes of the interface and the use of non-cartesian meshes. The coupling of VOF and Levet-Set is a promising way to take full advantage of both methods strengths while accommodating their drawbacks, see 20–23. For both Level-Set and VOF methods, adjusted jump conditions allow an accurate treatment of heat and mass fluxes through the interface to address phase change while surface tension is usually incorporated using the Convected-Distributed Force (CDF) model of Unverdi and and Tryggvason in 12 or the Continuous Surface Force (CSF) model of Brackbill in 24. Both CDF and CSF models require an accurate location of the interface thus the importance allocated to this task in the sharp methods. Despite the mentioned hurdles, both Level-Set and VOF methods have allowed groundbreaking numerical simulations such as in 18 or 25 and are now established as a standard to deal with incompressible flows. Moreover, their application to compressible flows has sustained substantial

---

[a)]Electronic mail: davy.nayigizente@centralesupelec.fr
[b)]Electronic mail: thomas.schmitt@ecp.fr

Physics of Fluids ACCEPTED MANUSCRIPT

This is the author's peer reviewed, accepted manuscript. However, the online version of record will be different from this version once it has been copyedited and typeset.

PLEASE CITE THIS ARTICLE AS DOI: 10.1063/5.0048715

AIP Publishing

improvements such as the ones proposed in 26 and 27 which foresees sufficient robustness and efficiency.

In the other class, the Diffuse Interface Methods (DIM), the interface is considered as a volumetric region within which the thermodynamic variables vary rapidly yet continuously. By principle, DIM do not require to locate the interface. The smoothing of the interface implies the creation of an interfacial region where classical thermodynamic treatments are no longer valid. The two approaches present among the DIM offer specific ways to treat the thermodynamics in the interface. They are particularly adapted to the study of compressible flows, as treated in this work, hence our focus on this class of methods. The Multi-Fluid methods (MFM), see 28–32, are based on a definition of an artificial mixture between the two phases in the interfacial region. Depending on the problem, additional equilibrium hypothesis can be enforced upon the two phases in the artificial mixture, for instance velocity, temperature, pressure and/or chemical equilibrium. From this Eulerian description ensues a set of four to seven equations to solve at once, usually involving a volume or a mass fraction. MFM have been introduced for shock capturing purposes and have been extended to other types of flows by 33–36. In particular, they articulate efficiently with the CSF model and allow the use of separate and more efficient EoS to describe the different phases. The second approach is formed by the Phase-Field methods (PFM) built after the work in 37–39, among others. In these methods, a phase parameter c is used to discriminate both phases, in a fashion similar to that of the Level-Set approach, the values of c varying continuously in the interface. However, the phase parameter definition is usually thermodynamically motivated: a component concentration for non-miscible fluids, the density for a two-phase compressible flows, etc... As such, the convection-diffusion equation of the phase parameter differs from the purely advective equation of the level-set function. Additionally, the phase parameter c is explicitly used to express the capillary forces, following the work of Korteweg in 40. An historical review of Korteweg's tensor derivation can be found in 41 and examples of use can be found in 42 and 43 or 44 . Interestingly, PFM combine quite easily with real gas thermodynamics as shown in 45 where the Peng-Robinson EoS has been used. Other applications can be found in 46 and 47 or 48. A key issue for DIM is controlling the interface width and in that prospect two points of view confront. Traditionally in MFM, the interface is maintained as sharp as possible using appropriate numerical treatments, as these methods were initially designed for shock capturing. Conversely, in PFM, the purpose is rather to have an interface wide enough to be resolved on the computational mesh because the capillary forces, expressed from the phase parameter gradients, need the latter to be properly evaluated. In that respect, the interface diffusion intrinsic to the DIM can act both as a help and an inconvenience. An early review of DIM presented by Anderson can be found in 49.

The Second Gradient (SG) theory, introduced by van der Waals in 39 qualifies as a Phase-Field method where the density ρ of the flow is chosen as the phase parameter, adding thermodynamic consistency to its derivation. This consistency shows through the values of the surface tension and the interface width that are physically predicted by the model, a feature that distinguishes it from other DIM, in particular PFM. Besides, the model can accommodate both subcritical and supercritical regimes indiscriminately. These particularities, along with the other distinctive features of the PF methods motivated the use of the SG theory for our study. Nonetheless, a major difficulty remains as the typical width of an interface, as predicted by the model, varies between a few Å and a few μm as soon as the temperature moves away from its critical value T_c. If one is to perform a straightforward numerical simulation of such systems, one must ensure that the mesh allows a decent mapping of the interface, of which width is not known *a priori*. This problem is shown prohibitive in terms of computational cost, even in simple 2D academic configurations. In the framework of a cryogenic rocket-engine, the system mostly works at high temperatures and high pressures once initiated. However, in order to simulate the complete ignition of the engine, one would encounter reduced temperatures with significantly lower values of interface width, hence the attention given to this issue in the present work.

In this study, the objective is to a achieve reasonable interface widths while maintaining its surface tension thus preserving its macroscopic behavior, as this is of paramount importance for our targeted cases. For Cahn-Hilliard systems, the interface width is imposed to the system as a parameter in the equations. Additionally, the surface tension is usually controlled by imposing a specific form (double-wheel) to the free energy of the fluid. This relation between the PFM choice and the interface surface tension and width has been detailed and explored, among others, in 50–52 or 47 where remarkable results have been obtained for theoretical cases. However, the lack of results fore more realistic cases in terms of fluid characteristics appeared as one major drawback to us. In particular, the double-wheel shape classically imposed to the free energy in these types of work seemed unfit for applications involving real gas flows where thermodynamic profiles strongly differs from the idealistic forms used in the previously mentioned studies. The choice has been made here to remain as close as possible to the thermodynamic foundations of real gas description while incorporating ideas coming from previous PFM studies. As already shown in 53, 33 or 54 the Second Gradient model provides a framework to achieve the thickening of an interface while controlling the surface tension, with thermodynamic consistency, hopefully allowing the latter to be captured on typical DNS meshes from the turbulence point of view. In this work, the SG theory is further investigated using a new thickening strategy based on a consistent thermodynamic modification of the interface.

The Second Gradient theory is recalled in Section 1 where its predictive capabilities regarding the saturation values (liquid and vapor densities, vapor pressure) as well as the unsteady response to mechanical perturbations applied to the interface are demonstrated. In Section 2, an in-depth analysis of the macroscopic variables of interest is proposed, namely

Physics of Fluids
ACCEPTED MANUSCRIPT
This is the author's peer reviewed, accepted manuscript. However, the online version of record will be different from this version once it has been copyedited and typeset.
PLEASE CITE THIS ARTICLE AS DOI: 10.1063/5.0048715
AIP Publishing

the surface tension and the interface width, since these are the variables one primarily wants to control when applying a thickening method to the interface. Our new thickening method is presented in Section 3 after a brief overview of the existing strategies and is then validated on canonical 2D configurations in Section 4. More advanced two and three-dimensional cases are computed using this method and are presented in Section 5. Finally we discuss the conclusions and the prospects of our study in Section 6.

I. THERMODYNAMICS OF A CAPILLARY FLUID

A. Equation of state

At very high pressures or in the liquid phase, the assumptions used to derive the ideal gas law, mostly that the components of the fluid merely interact which each other except through inelastic collisions, do not hold anymore. Since the equation of state (EoS) introduced by van der Waals in 55 several others have been proposed, relying on the molecular and kinetic theories of fluid, to achieve a better description of the real gas thermodynamics. With respect to these EoS, the state variables not only depend on the temperature but also on a secondary intensive variable such as the pressure or the density. The most commonly used EoS are the cubic ones as proposed in 55 and 56, or the Soave-Redlich-Kwong (SRK) EoS in 57 of which expression is given by:

$$P^{\mathrm{EoS}}(\rho,T)=\frac{\rho r T}{1-b\rho}-\frac{a(T)\rho^2}{1+b\rho} \tag{1}$$

where T and P^{EoS} are respectively the temperature and the thermodynamic pressure of the fluid, b is a constant and a is a function of the temperature of which definition solely depends on the fluid or the mixture characteristics. These EoS offer a good trade-off between accuracy and computational cost. As shown by the Clapeyron's diagram in Fig. (1) the SRK (and the other cubic) EoS faithfully transcribes the presence of the critical point, characterized by the pressure P_c and temperature T_c. The behavior of the fluid for temperatures above this point is also well-captured. No inflexion points are present on the isothermal pressure curves for all densities as the thermodynamics is continuous in supercritical conditions.

However, for temperatures lower than T_c, despite the ability of the cubic EoS to describe both liquid and vapor phases, it allows the existence of the spinodal region where the thermodynamics becomes unstable as explained by Giovangigli in 58. In practice, a state in this region corresponds to a two-phase regime where both the liquid and the vapor phases coexist, a distinctive feature for an interface. DIM offer multiple specific ways to describe the thermodynamics in the unstable region.

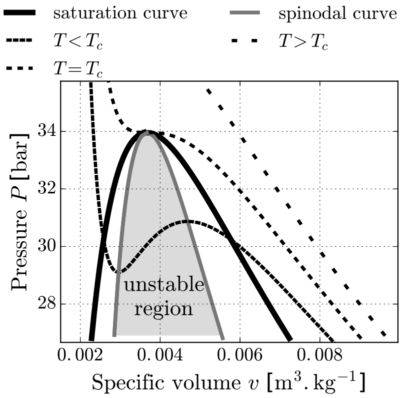

FIG. 1. Clapeyron's diagram of pressure versus specific volume for pure nitrogen N_2 with isothermal curves for different thermodynamic regimes calculated using the SRK equation of state

B. Second Gradient theory

Van der Waals demonstrated in 39 that the apparent thermodynamic instability in the spinodal region can be cleared up by improving the internal description of the fluid. The pressure curve in this region bears an actual physical meaning as a partial description of the internal constraints in the fluid, that must be completed. His strategy has been adapted afterwards to binary fluids by Cahn and Hilliard in 38 and 59 and 60. It was later used for DNS in 53 and 54 or 61 and is recalled in the next paragraphs.

1. Thermodynamic description

In the Second Gradient theory, the thermodynamics of the interface depends on the temperature T, the density ρ and additionally the density gradient $\nabla\rho$. The volumetric free energy F reads:

$$F(T,\rho,\nabla\rho)=F^{\mathrm{EoS}}(T,\rho)+\frac{\lambda}{2}(\nabla\rho)^2 \tag{2}$$

where F^{EoS} is the volumetric free energy as directly given by the EoS and λ is called the capillary coefficient. A more precise thermodynamic description, accounting for both density and entropy gradients can be found in 62 but will not be discussed in the present work.

From Eq. (2) one can write the modified Gibbs relation given by Eq. (3) where s is the specific entropy and derive the expression of the other variables like the thermodynamic pressure P^{th} in Eq. (4), the specific internal energy e_s in Eq. (5) and the specific free energy f in Eq. (6). Noticeably the expressions of the specific enthalpy h, the chemical potential μ and the specific isochoric heat capacity C_v are not modified

ACCEPTED MANUSCRIPT

Physics of Fluids

This is the author's peer reviewed, accepted manuscript. However, the online version of record will be different from this version once it has been copyedited and typeset.

PLEASE CITE THIS ARTICLE AS DOI: 10.1063/5.0048715

AIP Publishing

by this new thermodynamic description under the assumption, later justified, that λ is constant.

$$de_s = T\,ds + \frac{P}{\rho^2}\,d\rho + \lambda \boldsymbol{\nabla}\rho \cdot d\boldsymbol{\nabla}\rho \tag{3}$$

$$P^{\mathrm{th}} = P^{\mathrm{EoS}} - \lambda\,(\boldsymbol{\nabla}\rho)^2 \tag{4}$$

$$e_s = {e_s}^{\mathrm{EoS}} + \frac{\lambda}{2\rho}\,(\boldsymbol{\nabla}\rho)^2 \tag{5}$$

$$f = f^{\mathrm{EoS}} + \frac{\lambda}{2\rho}\,(\boldsymbol{\nabla}\rho)^2 \tag{6}$$

2. *Mechanical equations*

To remain consistent, this new thermodynamic description of the interfacial region must be coupled with a higher order modeling of the internal mechanical constraints as shown by 40 and 63 or 61. Using an Hamiltonian approach as in 64, the Thermodynamics of Irreversible Processes as in 33 or the Virtual Power Principle as in 65 it is possible to derive the new equations of motion for the fluid satisfying the first and second principles of thermodynamics:

$$\frac{\partial\rho}{\partial t} = -\boldsymbol{\nabla}\cdot\rho\mathrm{v} \tag{7a}$$

$$\frac{\partial\rho\mathrm{v}}{\partial t} = -\boldsymbol{\nabla}\cdot\left[\rho\mathrm{v}\otimes\mathrm{v} + p\underline{\underline{\mathbf{I}}} + \lambda\boldsymbol{\nabla}\rho\otimes\boldsymbol{\nabla}\rho - \underline{\underline{\tau}}^d\right] \tag{7b}$$

$$\begin{aligned}\frac{\partial\rho E}{\partial t} = -\boldsymbol{\nabla}\cdot\big[&(\rho E + p)\,\mathrm{v} + \lambda\,(\boldsymbol{\nabla}\rho\otimes\boldsymbol{\nabla}\rho)\cdot\mathrm{v} \\ &+ \lambda\rho\boldsymbol{\nabla}\rho\,(\boldsymbol{\nabla}\cdot\mathrm{v}) - \underline{\underline{\tau}}^d\cdot\mathrm{v} + \boldsymbol{q}\big]\end{aligned} \tag{7c}$$

where v, p, $\underline{\underline{\tau}}^d$, $\boldsymbol{q}$ are respectively the fluid velocity, mechanical pressure, viscous stress tensor and energy flux. Once given the expressions of $\underline{\underline{\tau}}^d$, $\boldsymbol{q}$ and the choice of an EoS, the previous system is closed. The mechanical pressure p and the pressure P^{EoS} from the EoS are linked by Eq. (8) and this denomination, inherited from 54, is justified by Eq. (7b) where p appears as the isotropic part of the non-viscous stress tensor.

$$p = P^{\mathrm{EoS}} - \frac{\lambda}{2}(\boldsymbol{\nabla}\rho)^2 - \rho\boldsymbol{\nabla}\cdot(\lambda\boldsymbol{\nabla}\rho) \tag{8}$$

To simplify this study, the thermal conduction and the viscous constraints are not taken into account as their proper integration into the method presented in this study is still an ingoing work. Here, we primary focus on the mechanical and thermodynamic behavior of the interface.

It should be mentioned that the expressions of Korteweg's tensor $\lambda\boldsymbol{\nabla}\rho\otimes\boldsymbol{\nabla}\rho - \frac{\lambda}{2}(\boldsymbol{\nabla}\rho)^2 - \rho\boldsymbol{\nabla}\cdot(\lambda\boldsymbol{\nabla}\rho)$ and the peculiar term $\lambda\rho\boldsymbol{\nabla}\rho\,(\boldsymbol{\nabla}\cdot\mathrm{v})$ in the Dunn and Serrin heat flux have been retrieved from the kinetic theory of gases by Giovangigli in 66 where the author has performed a second-order expansion of the pair distribution function to account for the new capillary terms.

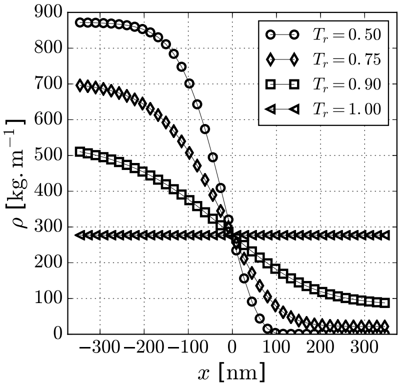

FIG. 2. Examples of density profiles for isothermal N_2 interfaces at different reduced temperature $T_r = T/T_c$ *(right)* with $\lambda = 1.0 \cdot 10^{-10}$ m^7.kg^{-1}.s^{-2}

C. Canonical isothermal interfaces

For an isothermal 1D planar interface at equilibrium ($\mathrm{v} = \mathbf{0}$) with no viscosity and thermal conduction, the system Eq. (7a) - Eq. (7c) reduces to the momentum equation in the form:

$$\frac{\partial P^{\mathrm{EoS}}}{\partial x} = \lambda\rho\frac{\partial^3\rho}{\partial x^3} \tag{9}$$

It can be shown, with thermodynamic arguments, that interfaces at equilibrium are actually compelled to be isothermal, as explained in 67 or in 68.

By solving this equation at a chosen temperature T_0 with a stationary solver, it is possible to retrieve the profiles of thermodynamic variables for a given interface.

Figure 2 shows density profiles acquired trough the resolution of Eq. (9) for different temperatures using a Newton solver. The interface width, calculated with Eq. (28) is also provided for a wide range of reduced temperature $T_r = T/T_c$. The resulting curves in Fig. 2 raise the following observations. The values of the saturation densities ρ_l and ρ_v are not given *a priori* to the solver but result from the computations. Besides, these values match those one would find with equilibrium calculations based on chemical potential balancing. These values solely depend on the temperature T_0 and not on the capillary coefficient λ. The width of the interface directly depends on the values of T_0 and λ. This result was expected and will be explained analytically in the next section. If T_0 is chosen above the critical temperature of the fluid T_c, the system independently converges towards a constant value for the density profile. This result concurs with the fact that no capillary effects spontaneously arise in trans/supercritical conditions given that, in these conditions, the heterogeneous system is no longer stable.

The results from the stationary solver can then be used as initial solutions for non stationary simulations where the sys-

Physics of Fluids

ACCEPTED MANUSCRIPT

This is the author's peer reviewed, accepted manuscript. However, the online version of record will be different from this version once it has been copyedited and typeset.

PLEASE CITE THIS ARTICLE AS DOI: 10.1063/5.0048715

AIP Publishing

tem Eq. (7a) - Eq. (7c) is solved in 1D and also act as a reference for the expected final solutions. Starting from an interface given by the stationary solver, a stretching or a compression is applied to introduce a mass unbalance. The interface can be convected at a constant speed. Eventually, both the deformation and the convection can be combined. In all those cases, we verified that the interface behaves as expected and effectively goes back to its initial width. These simulation served as a first validation of both the model and our numerical implementation (the numerical setup used is detailed in Sec. IV A 1).

II. SURFACE TENSION AND INTERFACE THICKNESS

A. Surface tension for capillary fluid

1. *Thermodynamic approach*

Considering a reference temperature $T_0 < Tc$, and the associated saturation densities ρ_l and ρ_v, it is well-established, see 69, that when the capillary forces are not accounted for, an unstable thermodynamic state instantaneously evolves toward the closest stable one between the liquid and vapor phases. For a 1D planar interface, this results in a discontinuity on the density profile between the values ρ_l and ρ_v. This is the description retained by the sharp interface methods. The position of that discontinuity is noted here x_{int} and is used to represent the position of the interface. The corresponding density profile, noted $\bar{\rho}$ and defined by $\bar{\rho}(x) = \rho_v$ if $\leqslant x_{\text{int}}$ and ρ_l if $x > x_{\text{int}}$, will be used as a reference. Following the idea proposed by Cahn in 38 one can express the surface tension σ of the interface taking into account the capillary forces. It corresponds to the extra free energy acquired by the diffuse interface comparatively to the discontinuous profile $\bar{\rho}$. This free energy gap writes:

$$\sigma = \int_{x_v}^{x_l} \left[F^* - \bar{F}\right] dx = \int_{x_v}^{x_l} \left[F(\rho^*) - F^{\text{EoS}}(\bar{\rho})\right] dx \tag{10}$$

where $\rho^*(x)$ is the equilibrium density profile of the interface when the capillary forces are considered, bounded between the positions x_v and x_l (meaning that $\rho^*(x) = \rho_v$ for $x \leqslant x_v$ and $\rho_l(x) = \rho_l$ for $x \geqslant x_l$), $F^* = F(\rho^*)$ the corresponding volumetric free energy profile and $\bar{F} = F^{\text{EoS}}(\bar{\rho})$ the volumetric free energy profile of the reference sharp interface. This definition of the surface tension is based on the notion of excess values introduced early on by van der Waals in 39 and more properly described by Edwards in 70 which is illustrated in Fig. (3).

The equilibrium profile of the interface will be the one minimizing the total free energy $\mathscr{F}$ of the system. However, since the total free energy of the canonical interface $\bar{\mathscr{F}}$ is a fixed quantity, the minimization of $\mathscr{F}$ is equivalent to the minimization of $\mathscr{F} - \bar{\mathscr{F}}$ leading to:

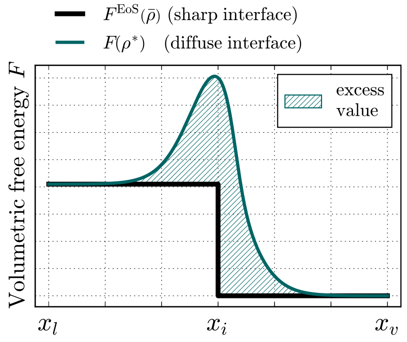

FIG. 3. Schematic representation of the excess volumetric free energy F

$$\begin{gathered}\min_{\rho} \mathscr{F}(\rho) = \min_{\rho} \int_{x_v}^{x_l} F(\rho)\, dx \\ \Longleftrightarrow \\ \min_{\rho} \left[\mathscr{F}(\rho) - \bar{\mathscr{F}}\right] = \min_{\rho} \int_{x_v}^{x_l} \left[F(\rho) - \bar{F}\right] dx\end{gathered} \tag{11}$$

Calling I the integrand in the right integral of Eq. (11) and using the expression of F in Eq. (2) one can write:

$$I = F(\rho) - \bar{F} = F^{\text{EoS}}(\rho) + \frac{\lambda}{2}\left(\frac{\partial \rho}{\partial x}\right)^2 - \bar{F} \tag{12}$$

Following the methodology proposed in 71, the integral minimization problem in Eq. (11) can be reformulated in terms of a partial derivative equation:

$$I - \left(\frac{\partial \rho}{\partial x}\right)\left(\frac{\partial I}{\partial\left(\frac{\partial \rho}{\partial x}\right)}\right)_{\rho} = a \tag{13}$$

Here a is a constant to be determined. For that, one can notice that $(\partial\rho/\partial x)^2$ is the only term in I in Eq. (12) with a formal dependency on the density gradient $\partial\rho/\partial x$. The relation in Eq. (13) is satisfied by the equilibrium profile. In any of the bulk phases, the density gradient is equal to zero. Both the reference sharp profile and the equilibrium profile have the same values of boundary densities ρ_l and ρ_v. Consequently, F^{EoS} and $\bar{F}$ are also equal in the bulk phases, resulting in $a = 0$ which allows to write:

$$F^{\text{EoS}}(\rho^*) - \bar{F} = \frac{\lambda}{2}\left(\frac{\partial \rho^*}{\partial x}\right)^2 \tag{14}$$

Physics of Fluids
ACCEPTED MANUSCRIPT
This is the author's peer reviewed, accepted manuscript. However, the online version of record will be different from this version once it has been copyedited and typeset.
PLEASE CITE THIS ARTICLE AS DOI: 10.1063/5.0048715
AIP Publishing

This new relation can then be injected in Eq. (10) to finally obtain the expression of the surface tension:

$$\sigma = \int_{x_v}^{x_l} \lambda \left(\frac{\partial \rho}{\partial x}\right)^2 dx \tag{15}$$

This result can be physically interpreted as follows. The minimization of the integral of I, leading to the equilibrium, will result from a balance between two terms. The first one is the integral of $\Delta F^{\mathrm{EoS}} = F^{\mathrm{EoS}}(\rho) - F^{\mathrm{EoS}}(\bar{\rho})$ and translates as the energetic cost necessary to diffuse the interface rather than to maintain it as a discontinuity. The second one is the integral of $\Delta F^{\mathrm{capi}} = \lambda/2\left(\partial\rho/\partial x\right)^2$ and is the energetic cost associated to the capillary forces themselves. To lower ΔF^{capi}, the interface will tend to diffuse itself to reduce its gradient but this will increase ΔF^{EoS}, the energy gap with the discontinuous profile, and vice versa. The equilibrium is achieved when these two terms are equal.

2. Relation between the thermodynamical and mechanical points of view

Eq. (15) has also been obtained by Jamet in 65 using Eq. (9). In particular, given the differential relation $d\mu^{\mathrm{EoS}} = -s\,dT + dP^{\mathrm{EoS}}/\rho$ which simplifies in $d\mu^{\mathrm{EoS}} = dP^{\mathrm{EoS}}/\rho$ in the isothermal case, Eq. (9) can be written as:

$$\left(\mu^{\mathrm{EoS}} - \mu^{\mathrm{sat}}\right)(x) = \lambda \frac{\partial^2 \rho}{\partial x^2}(x) \tag{16}$$

where μ^{EoS} is the chemical potential of the fluid as given by the equation of state and μ^{sat} is the value of this chemical potential at saturation. A classic result from thermodynamics is that at equilibrium, μ^{sat} has the same value in the liquid and the vapor phases. Thanks to the differential relation $dF^{\mathrm{EoS}} = -S\,dT + \mu^{\mathrm{EoS}}\,d\rho$ where S is the volumetric entropy, which simplifies in $dF^{\mathrm{EoS}} = \mu^{\mathrm{EoS}}\,d\rho$, it appears that Eq. (16) and Eq. (14) are equivalent.

These two equivalent differential equations ensure the uniqueness of the non-constant equilibrium interface profile for a chosen temperature (and a chosen λ). This in turn defines unique values for the surface tension σ and for the interface width h allowing to retrieve that both are only functions of the temperature at equilibrium. This link is further developed by the following derivations.

Firstly, one can notice that from Eq. (16):

$$\frac{\partial}{\partial x}\left(\left(\frac{\partial \rho}{\partial x}\right)^2\right) = 2\left(\mu^{\mathrm{EoS}} - \mu^{\mathrm{sat}}\right)\frac{\partial \rho}{\partial x} \tag{17}$$

and then introducing Υ by:

$$\Upsilon(\rho) = 2\int_{\rho_v}^{\rho} \left(\mu^{\mathrm{EoS}} - \mu^{\mathrm{sat}}\right)(\rho)\,d\rho \tag{18}$$

one can write the following equation, substituting the spatial variable $\varkappa$ with the density variable ρ:

$$\begin{aligned}\int_{x_v}^{x} \frac{\partial}{\partial \varkappa}\left(\lambda\left(\frac{\partial \rho}{\partial \varkappa}\right)^2\right)(\varkappa)\,d\varkappa &= 2\int_{x_v}^{x}\left(\mu^{\mathrm{EoS}} - \mu^{\mathrm{sat}}\right)(\varkappa)\frac{\partial \rho}{\partial \varkappa}\,d\varkappa \\ &= 2\int_{\rho_v}^{\rho}\left(\mu^{\mathrm{EoS}} - \mu^{\mathrm{sat}}\right)(\rho)\,d\rho\end{aligned} \tag{19}$$

$$\lambda\left(\frac{\partial \rho}{\partial \varkappa}\right)^2(x) = \Upsilon(\rho(x)) \tag{20}$$

The surface tension can therefore be linked to the chemical potential gap with:

$$\sigma = \int_{x_v}^{x_l} \Upsilon(\rho)\,dx \tag{21}$$

Here, Υ has been expressed as an integral that contains formally no dependency on the geometry of the interface but only on its intrinsic thermodynamic description through the expression of $\mu^{\mathrm{EoS}}(\rho)$. However, the integration that is necessary to obtain σ (Eq. (21)) shows a clear spatial dependency. Eq. (21) also shows that the surface tension depends on the energetic behavior of the interface through its propensity to store capillary energy driven by $\mu^{\mathrm{EoS}} - \mu^{\mathrm{sat}}$ (or likewise $P^{\mathrm{EoS}} - P^{\mathrm{sat}}$) and on its inherent geometry mostly controlled by λ and the interfacial constraints. This duality will play a preponderant role in the rest of the study.

B. Determination of the capillary coefficient

Given its role in Eqs. (14) and (16), it is clear that λ impacts the equilibrium profile of the interface. Since experimentally it is well established that σ and h solely depend on the temperature for pure fluids, λ should only depend on the temperature as well. This is confirmed by the expression derived by Roccard in 63:

$$\lambda = \frac{ad^2\eta}{RM^2} \tag{22}$$

where R is the gas constant, M the molar mass of the fluid and a, η, d coefficients depending on the microscopic distribution of the molecular central forces of interaction, which is indeed directly linked to the temperature of the fluid. However, this formula is not of practical use for us given the difficulty to estimate a, η and d.

Another way to evaluate λ is to use Eq. (15) backwards exploiting experimental measurements or analytical developments that allow to directly estimate the surface tension for

Physics of Fluids ACCEPTED MANUSCRIPT

This is the author's peer reviewed, accepted manuscript. However, the online version of record will be different from this version once it has been copyedited and typeset.

PLEASE CITE THIS ARTICLE AS DOI: 10.1063/5.0048715

AIP Publishing

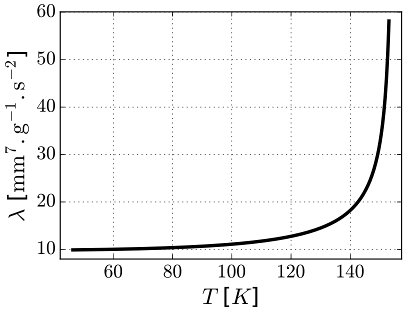

FIG. 4. Evolution of the capillary coefficient λ with the temperature for oxygen O_2 using SRK equation of state

pure fluids at a given temperature T. Knowing this reference value $\sigma(T)$ it is then possible to iterate on the value of λ to compute 1D planar interfaces until a match is reached using Eq. (15) to calculate $\sigma(\lambda)$. Such a comprehensive analysis has been proposed in 72 using the Volume Translated Peng-Robinson EoS and has even been extended to binary mixtures. We performed the same calculation using a simplier framework with the classical Soave-Redlich-Kwong EoS. For instance Fig. (4) shows the evolution of λ with the temperature for pure oxygen. The surface tension has been evaluated using the formula from 73 based on the corresponding state principle.

Both Lin's and our correlations give the same trend. For a wide range of temperature, λ can be considered constant with a limited loss of accuracy. However, the capillary coefficient diverges as the temperature approaches its critical value. For these temperatures, the constant λ hypothesis does not hold anymore. This divergence is a consequence of evaluating λ by fitting the surface tension with the cubic EoS. It can be explained by the fact that the interface keeps on widening as the temperature increases and is eventually infinitely wide once the regime becomes supercritical. However, by reverting to the fundamental definition Eq. (22), the use of kinetic theory of gases allows to show that the actual value of λ converges towards a constant as the temperature increases, as shown in 74 for the Lennard-Jones potential. Moreover, the energetic considerations made by the authors in 38 have no reasons to be discarded above critical conditions meaning that the contributions from λ should still be considered in said conditions despite no actual interface being present. It should be mentioned, as explained in 72, that surface tension values obtained evaluating λ with expressions from the kinetic theory of gases systematically lead to strong disparities with experimental data, thus motivating the extraction of correlations such as Lin's and our own.

However, since our primary concern is to ensure that the interface is wide enough to be captured on the simulation mesh, the simplified correlation shown in Fig. (4) can still be a useful simplification. Besides, this allows to transit from subcritical to supercritical temperatures without loss of generality. Therefore, for the rest of the study and for the sake of simplicity, λ will be considered as independent of the temperature.

C. Influence of the capillary coefficient

1. Auto-similarity of the plane interface profiles

Let us consider a 1D planar interface at equilibrium for a fixed temperature T_0 and ρ^0 the density profile of said interface calculated with the capillary coefficient λ_0. The corresponding EoS pressure profile is $P^0 = P^{\mathrm{EoS}}\left(\rho^0\right)$. The interface is supposed to be centered at $x_{\mathrm{int}} = 0$. Let ϕ be a strictly positive constant and $X = x/\phi$. Since ρ^0 satisfies Eq. (9), one can write:

$$\forall X, \quad \frac{\partial P^{0^{\mathrm{EoS}}}}{\partial x}(X) = \lambda_0 \rho^0(X)\frac{\partial^3\rho^0}{\partial x^3}(X) \tag{23}$$

Let ρ^ϕ be the density profile defined by:

$$\forall x, \quad \rho^\phi(x) = \rho^0(X = x/\phi) \tag{24}$$

which is an expansion if $\phi > 1$ (or a compression otherwise) of the initial profile ρ^0 by a factor ϕ. One can also define the associated pressure profile $P^\phi = P^{\mathrm{EoS}}\left(\rho^\phi(x)\right) = P^0(X)$ and obtain the following relations:

$$\frac{\partial P^\phi}{\partial x}(x) = \frac{1}{\phi}\frac{\partial P^0}{\partial x}(X) \tag{25}$$

$$\frac{\partial^3\rho^\phi}{\partial x^3}(x) = \frac{1}{\phi^3}\frac{\partial^3\rho^0}{\partial x^3}(X) \tag{26}$$

which, injected into Eq. (23), lead to:

$$\frac{\partial P^\phi}{\partial x}(x) = \phi^2\lambda_0\frac{\partial^3\rho^\phi}{\partial x^3}(x) \tag{27}$$

It clearly appears that the profile ρ^ϕ is the solution of Eq. (9) where the capillary coefficient has been multiplied by a factor ϕ^2. ϕ will play a major role in our thickening strategy and its impact will be detailed in the rest of the study.

2. Impact on the surface tension and the interface thickness

The previous result can be inverted by saying that solving Eq. (9), at a fixed temperature T_0, with two capillary coefficients λ and $\phi^2\lambda$ will give two density profiles, the second being an expansion (or compression) of the first one by a factor ϕ.

The thickness of an interface can be defined in multiple ways. In this study we choose the definition given by Eq. (28), which bears a meaning regarding numerical simulations since increasing or decreasing this thickness directly means

Physics of Fluids ACCEPTED MANUSCRIPT

This is the author's peer reviewed, accepted manuscript. However, the online version of record will be different from this version once it has been copyedited and typeset.

PLEASE CITE THIS ARTICLE AS DOI: 10.1063/5.0048715

changing how well the stiff gradients are resolved on a given mesh:

$$h = \frac{(\rho_l - \rho_v)}{\max|\nabla\rho|} \tag{28}$$

With this definition, calling h_0 the thickness of the interface calculated with a capillary coefficient λ_0, Eq. (25) applied to the densities ρ^0 and ρ^ϕ gives that $\max\left|\nabla\rho^\phi\right| = \max\left|\nabla\rho^0\right|/\phi$ for the interface calculated with $\lambda_\phi = \phi^2\lambda_0$. Therefore, with Eq. (28) it leads to $h_\phi = \phi h_0$.

To evaluate the surface tension, one can start by transforming Eq. (15), substituting the variables x and ρ in order to get an integral, of which limits do not depend on the geometry of the interface (which is affected by a modification of the capillary coefficient). For instance, ρ_l and ρ_v only depend on the temperature, and:

$$\sigma = \int_{x_v}^{x_l} \lambda \left(\frac{\partial\rho}{\partial x}\right)^2 dx = \int_{x_v}^{x_l} \lambda \frac{\partial\rho}{\partial x}\frac{\partial\rho}{\partial x} dx = \int_{\rho_v}^{\rho_l} \lambda \frac{\partial\rho}{\partial x} d\rho \tag{29}$$

Once again, calling σ_0 and σ_ϕ the surface tensions of the interfaces calculated with the capillary coefficients λ_0 and λ_ϕ, using Eq. (29) gives:

$$\sigma_\phi = \int_{\rho_v}^{\rho_l} \lambda_\phi \frac{\partial\rho^\phi}{\partial x} d\rho = \int_{\rho_v}^{\rho_l} \phi^2\lambda_0 \frac{1}{\phi}\frac{\partial\rho^0}{\partial x} d\rho \tag{30a}$$

$$= \phi \int_{\rho_v}^{\rho_l} \lambda_0 \frac{\partial\rho^0}{\partial x} d\rho = \phi\sigma^0 \tag{30b}$$

Finally, these two results can be summarized by the following dependencies:

$$h \propto \sqrt{\lambda} \qquad\qquad \sigma \propto \sqrt{\lambda} \tag{31}$$

These correlations have been retrieved analytically near the critical point in 54 and numerically by 33 and are confirmed in Fig. (5). In both series of curves displayed, the slope is $1/2$ in logarithmic scale, as expected from Eq. (31).

III. INTERFACE THICKENING STRATEGIES FOR DNS

A. On the need to thicken the interface

So far we have shown how the Second Gradient theory allows for an accurate representation of an interface, for temperatures relatively far from the critical point, both from a thermodynamical and mechanical point of view. However, the results previously shown rely on very fine meshes and the width of the interfaces is still far under the size we can afford to resolve for industrial applications given the current available computational power. From Fig. (6) the expected width using the Second Gradient theory would be comprised between a few nm and a few μm for the range of temperatures relevant to actual injectors. Conversely, the typical Kolmogorov's eddy scale for such flows varies between a few μm and a few mm, see 75, leading to a scaling factor between the smallest eddies scale and the interfaces width of at least 10^3.

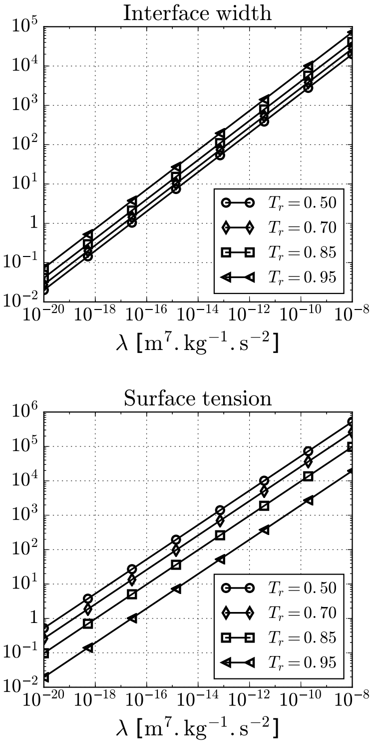

FIG. 5. Evolution of the interface thickness h and surface tension σ with the capillary coefficient λ for oxygen O_2 at different reduced temperature T/T_c in logarithmic scales

Given this observation, even for DNS configurations, the interface should be thickened to be resolved on more realistic meshes, even for academic applications. A first idea would be to increase the capillary coefficient λ. However the relations given in Eq. (31) showed that while the interface would indeed be thickened, the surface tension would also be augmented modifying the macroscopic behavior of the interface. We present here a novel method in oder to thicken the interface while avoiding this major drawback, the objective being to reach typical DNS mesh sizes without modifying the surface tension.

It should be noticed that the issue of thickening has already been addressed by Jamet. He proposed two different strategies of which principles are the foundations of the method we pro-

Physics of Fluids ACCEPTED MANUSCRIPT

This is the author's peer reviewed, accepted manuscript. However, the online version of record will be different from this version once it has been copyedited and typeset.

PLEASE CITE THIS ARTICLE AS DOI: 10.1063/5.0048715

AIP Publishing

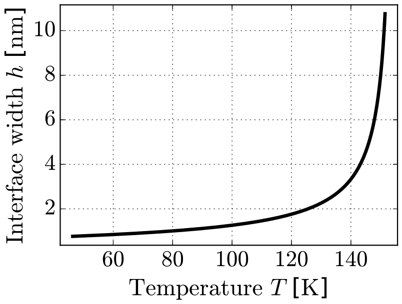

FIG. 6. Evolution of the interface width h with the temperature T as predicted by the Second Gradient theory for pure oxygen O_2, $T_c = 158.54$ K

posed in this study. In his first strategy from 54, Jamet shows that Eq. (16) has an analytical solution. This allowed him to express both the interface width and the surface tension with:

$$\begin{cases} h = \dfrac{4}{\rho_l - \rho_v}\sqrt{\dfrac{\lambda}{2A}} & \text{(32a)} \\ \sigma = \dfrac{(\rho_l - \rho_v)^3}{3}\sqrt{2A\lambda} & \text{(32b)} \end{cases}$$

The physical meaning of coefficient A can be found in Jamet's work 54 and 76. It is related to the isothermal compressibility in the bulk phases. In Eqs. (32a) and (32b), the dependencies $h \propto \sqrt{\lambda}$ and $\sigma \propto \sqrt{\lambda}$ previously found are visible again. The key point here is the dependency of the interface width h and the surface tension σ with A, namely $h \propto 1/\sqrt{A}$ and $\sigma \propto \sqrt{A}$. This reversed dependency allows to play on both λ and A to obtain any desired values for σ and h simultaneously. This method, although simple to apply, presents three main drawbacks. Firstly, in order to apply the relations in Eqs. (32a) and (32b) the values of the saturation densities ρ_l and ρ_v must be obtained beforehand. This is however achievable using for instance a thermodynamic equilibrium solver. Secondly, the range of application for this method is extremely narrow around the critical conditions. In practice this method seems to fail for reduced temperatures below $T_r = 0.99$ and therefore is not suited for industrial application in its current formulation. Lastly, modifying the coefficient A leads in fact to a modification of the compressibility coefficients in the bulk phases and may jeopardize the thermodynamic consistency since it may in turn modify the heat capacities and the sound speed. Through this study, Jamet showed that a second coefficient could be introduced to modulate the macroscopic behavior.

Following this first idea, Jamet proposed in 54 and 76 a more complex and complete procedure, by modifying directly the functional $\Psi(\rho) \hat{=} \rho' = \partial\rho/\partial x$ in the interface. Given this definition of Ψ, he derived the following six equations, the meaning of which is discussed hereunder:

$$\Psi(\rho_v) = 0 \tag{33a}$$

$$\Psi(\rho_l) = 0 \tag{33b}$$

$$\left(\frac{d\Psi}{d\rho}(\rho_v)\right)^2 = \frac{1}{\lambda}\frac{1}{\rho_v}\frac{dP}{d\rho}(\rho_v) \tag{33c}$$

$$\left(\frac{d\Psi}{d\rho}(\rho_l)\right)^2 = \frac{1}{\lambda}\frac{1}{\rho_l}\frac{dP}{d\rho}(\rho_l) \tag{33d}$$

$$\max\Psi = \frac{\rho_l - \rho_v}{h} \tag{33e}$$

$$\lambda\int_{\rho_v}^{\rho_l}\Psi(\rho)\,d\rho = \sigma \tag{33f}$$

One must notice that the derivative $dP/d\rho$ is directly given by the chosen equation of state (T being fixed for the study) and its definition is not modified by the Second Gradient theory. First Eqs. (33a) and (33b) account for the fact that there is no density gradient in the bulk phases. Eqs. (33c) and (33d) impose the thermodynamics to be differentiable at the boundaries between the bulk phases and the binodal region. Finally Eqs. (33e) and (33f) link Ψ to the interface width as defined by Eq. (28) and the surface tension as expressed in Eq. (15)

This method ensures the thermodynamic consistency of the system. In particular the heat capacities and the latent heat are continuous throughout the interface. However, one must find a profile function Ψ that satisfies all these constraints, which reveals to be intricate for Eqs. (33c), (33d) and (33e) where the use of a Newton-like solver is required, at each time step on every mesh points. Using this method in 76, Jamet studied several typical capillary phenomena such as the disappearance or the coalescence of bubbles and the dynamical hysteresis in the contact angle with a wall.

This second thickening method is both powerful and consistent. However we spotted two major drawbacks when it comes to its application in our targeted simulations. Firstly, the method requires to geometrically locate and qualify the interface in order to be applied because it relies on a local geometrical modification of the interface shape, while the first method only needed the values of the saturation densities. Secondly, most of the thermodynamic variables have to be recalculated multiple times at every step for every point because of the calculations required by the Newton-like solving procedure. One could argue that some of the results could be tabulated to save computational time, however this tabulation would be mixture-dependent which also constitutes a drawback regarding future complex simulations.

B. The Thickened Interface Method (TIM)

1. *Foundations of the method*

Changing uniformly the value of λ has been shown to be insufficient to thicken the interface without augmenting the sur-

Physics of Fluids

ACCEPTED MANUSCRIPT

This is the author's peer reviewed, accepted manuscript. However, the online version of record will be different from this version once it has been copyedited and typeset.

PLEASE CITE THIS ARTICLE AS DOI: 10.1063/5.0048715

AIP Publishing

face tension. The addition of a second parameter has proven to be a good idea in order to choose both σ and h as in Jamet's first thickening strategy. Using this paradigm, the purpose is therefore to derive a method that allows such flexibility. Moreover, in his second method, Jamet showed the necessity to consistently modify the thermodynamics jointly with the mechanics in the interfacial region. Essentially, we would like to introduce here a coefficient ϕ_s so that $h \propto \sqrt{\phi_s}$ and $\sigma \propto 1/\sqrt{\phi_s}$ (the same effect as when modifying A in Eqs. (32a) and (32b)). The impact of ϕ_s should allow to mitigate the effect of modifying λ on both h and σ. From *Eq.*(21), reducing σ by a certain factor can be done in a thermodynamically consistent manner by dividing Υ by a constant. Moreover, from the definition given by Eq. (18), a straightforward way to do so is to divide a priori $\mu^{\mathrm{EoS}} - \mu^{\mathrm{sat}}$ by this constant. This modification has the advantage of not being performed on λ and therefore should avoid the associated drawbacks. As done to address the impact of a modification of λ in II C, the impact of the thermodynamic modification in Eq. (34) is studied in the next paragraph, where η is a constant of which value will be chosen depending on the desired outcome.

$$\left(\mu^{\mathrm{EoS}} - \mu^{\mathrm{sat}}\right) \to \left(\mu^{\mathrm{EoS}} - \mu^{\mathrm{sat}}\right)/\eta \tag{34}$$

2. *Modification of the equation of state*

The modification introduced by the substitution in Eq. (34) presumably allows to diminish the surface tension of the interface in a controlled manner. However, by itself, it suffers two shortcomings. Firstly, this modification inherently assumes the interface to be isothermal as μ^{sat} is actually a function of the temperature. Secondly, this modification of the chemical potential must be carried on and applied to the other thermodynamic variables to achieve a consistent model. In essence, Eq. (34) is to be understood as a modification of the EoS describing the fluid. In the following, we present the expression of the thermodynamic variables induced by this modification of the EoS. Here, for a variable χ, χ^{EoS} still refers to the variable as provided directly by the initial EoS and χ^{η} to the expression with the modified EoS induced by Eq. (34).

The starting modification is applied upon the chemical potential. Its full expression showing density and temperature dependencies reads:

$$\mu^{\eta}(\rho,T) = \mu^{\mathrm{sat}}(T) + \frac{\mu^{\mathrm{EoS}}(\rho,T) - \mu^{\mathrm{sat}}(T)}{\eta} \tag{35}$$

The chemical potential μ^{η} and the volumetric free energy F^{η} are linked by $\mu^{\eta} = (\partial F^{\eta}/\partial\rho)_T$. Enforcing the condition $F^{\eta}(\rho_v(T),T) = F^{\mathrm{EoS}}(\rho_v(T),T)$ and noticing $F^{\mathrm{EoS}}(\rho_v(T),T) = \rho_v(T)\mu^{\mathrm{sat}}(T)P^{\mathrm{sat}}(T)$, F^{η} can be expressed by:

$$F^{\eta}(\rho,T) = F_*^{\mathrm{sat}}(\rho,T) + \frac{F^{\mathrm{EoS}}(\rho,T) - F_*^{\mathrm{sat}}(\rho,T)}{\eta} \tag{36}$$

where $F_*^{\mathrm{sat}}(\rho,T) = \rho\mu^{\mathrm{sat}}(T) - P^{\mathrm{sat}}(T)$ (the same expression is obtained enforcing $F^{\eta} = F^{\mathrm{EoS}}$ in the liquid).

The new EoS pressure is then defined by $P^{\eta} = \rho\mu^{\eta} - F^{\eta}$. Given Eqs. (35) and (36), one gets:

$$P^{\eta}(\rho,T) = P^{\mathrm{sat}}(T) + \frac{P^{\mathrm{EoS}}(\rho,T) - P^{\mathrm{sat}}(T)}{\eta} \tag{37}$$

The specific entropy is defined by $s^{\eta} = -(1/\rho)(\partial F^{\eta}/\partial T)_{\rho}$. Using Eq. (36) it can be written:

$$\begin{aligned} s^{\eta}(\rho,T) = \bar{s}(T) &+ \frac{s^{\mathrm{EoS}}(\rho,T) - \bar{s}(T)}{\eta} \\ &+ \left(1 - \frac{1}{\eta}\right)\left(\frac{1}{\rho} - \frac{1}{\bar{\rho}(T)}\right)\frac{dP^{\mathrm{sat}}}{dT}(T) \end{aligned} \tag{38}$$

where the notation $\bar{\chi}(T)$ designates the saturation value of a thermodynamical variable χ^{EoS} calculated indifferently in the liquid or the vapor phase for the temperature T as long as the same criteria is used to chose this value for all the thermodynamic variables.

Eventually, using ${e_s}^{\eta} = \mu^{\eta} + Ts^{\eta} - P^{\eta}/\rho$, the specific internal energy can also be expressed by:

$$\begin{aligned} {e_s}^{\eta}(\rho,T) = \bar{e_s}(T) &+ \frac{{e_s}^{\mathrm{EoS}}(\rho,T) - \bar{e_s}(T)}{\eta} \\ &+ \left(1 - \frac{1}{\eta}\right)\left(\frac{1}{\rho} - \frac{1}{\bar{\rho}(T)}\right)\left(T\frac{dP^{\mathrm{sat}}}{dT}(T) - P^{\mathrm{sat}}(T)\right) \end{aligned} \tag{39}$$

Practically, if for some computational node the value of $\bar{\chi}(T)$ is chosen in the liquid phase then $\bar{s}(T)$, $\bar{\mu}(T)$, $\bar{e_s}(T)$, etc... also have to be chosen in the liquid phase and vice versa. Noticeably though, the criterion to decide in which phase the value of $\bar{\chi}$ is evaluated can differ from one point to the other in the computational domain and can change from one iteration to the other. The only condition is the local consistency of this choice throughout the calculation of the thermodynamic variables at one point and at one instant. Conveniently, this lead to the useful following results (where $\rho_k = \rho_l$ or ρ_v) ensuring the continuity of the thermodynamics through the saturation bell independently of η:

$$\lim_{\rho\to\rho_k} e^{\eta}(\rho,T) = e^{\mathrm{EoS}}(\rho_k(T),T) \tag{40}$$

$$\lim_{\rho\to\rho_k} s^{\eta}(\rho,T) = s^{\mathrm{EoS}}(\rho_k(T),T) \tag{41}$$

The expression of other variables such as the specific isochoric heat capacity ${C_V}^{\eta}$, thermal expansion coefficient α^{η}, the isothermal compressibility coefficient β^{η} and the specific isobaric heat capacity ${C_P}^{\eta}$ are also to be derived. The aspect of P^{η}, μ^{η}, ${e_s}^{\eta}$ and s^{η} are given in Fig. (7) for different values of η.

3. *Impact on the isothermal interface*

Now that all the thermodynamic variables have been expressed for the modified EoS, the momentum equation can be

ACCEPTED MANUSCRIPT

Physics of Fluids

This is the author's peer reviewed, accepted manuscript. However, the online version of record will be different from this version once it has been copyedited and typeset.

PLEASE CITE THIS ARTICLE AS DOI: 10.1063/5.0048715

AIP Publishing

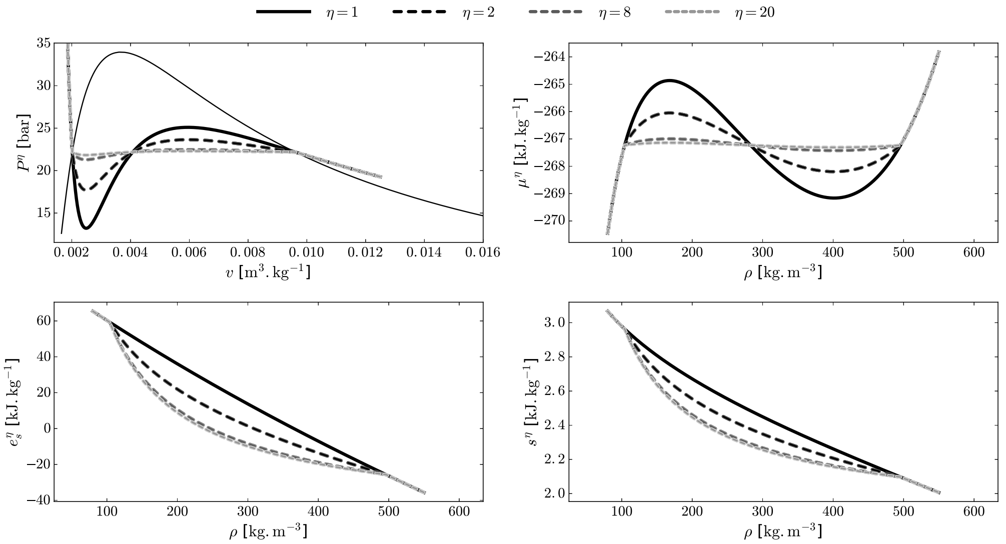

FIG. 7. Pressure from EoS, chemical potential, specific internal energy and speficic entropy of nitrogen N_2 at $T = 117$ *mathrmK* as modified by Eq. (34) for different values of η

written for an isothermal interface at equilibrium, still using a reference capillary coefficient λ_0. From Eq. (9), it reads:

$$\frac{\partial P^\eta}{\partial x} = \lambda_0 \rho^\eta \frac{\partial^3 \rho^\eta}{\partial x^3} \tag{42}$$

Here, we took care to reference the density profile by ρ^η as it mays also be impacted by the EoS modification. Since for an isothermal interface $P^{\text{sat}}(T)$ is a constant, the previous equation simplifies in

$$\frac{\partial P^{\text{EoS}}(\rho^\eta)}{\partial x} = \eta \lambda_0 \rho^\eta \frac{\partial^3 \rho^\eta}{\partial x^3} \tag{43}$$

From the study presented in II C and in particular Eq. (27), one can recognize from Eq. (43) that ρ^η is the density profile solution of Eq. (9) with a capillary coefficient $\eta\lambda_0$, that is to say, the reference interface for a capillary coefficient λ_0 thickened by a factor $\sqrt{\eta}$. In particular, this means that using the variable switching $X = x/\sqrt{\eta}$, one has $\rho^\eta(X) = \rho(x)$. Moreover, Eq. (18) and Eq. (35) allow to write $\Upsilon(\rho^\eta) = \Upsilon(\rho^0)/\eta$. With that, the new value of σ can also be obtained using Eq. (21), it gives:

$$\sigma_\eta = \int_{X_l}^{X_v} \frac{\Upsilon(\rho^\eta)}{d} X = \int_{x_l}^{x_v} \frac{\Upsilon(\rho^0(X))}{\sqrt{\eta}} dx = \frac{\sigma^0}{\sqrt{\eta}} \tag{44}$$

The impact of the EoS modification induced by Eq. (34) and consistently carried over the other thermodynamic variables in the previous paragraph has been established for h and σ. The dependency on η observed for both values matches the one targeted for the parameter ϕ_s. Therefore, this modification of the EoS will be adopted for our method by formally using ϕ_s in place of η in the new equation of state (and the notation χ^η by χ^{ϕ_s} for a variable χ).

4. Complete modifications of the TIM

By itself, the EoS modification is not sufficient to achieve the desired action for the TIM. However, by introducing the coefficient ϕ_l applied to the capillary coefficient such as $\lambda = \phi_l \lambda_0$, one can obtain the dependencies $h \propto \sqrt{\phi_l}$ and $\sigma \propto \sqrt{\phi_l}$. When combined with the modification associated with ϕ_s, the final dependencies read:

$$h \propto \sqrt{\phi_l \phi_s} \qquad \sigma \propto \sqrt{\phi_l / \phi_s} \tag{45}$$

As expected, the combined action of modifying the capillary coefficient and the EoS in the interface makes it possible to act independently on h and σ. An additional precaution as to be taken to complete the method. Indeed, for non isothermal cases, the TIM must leave the behavior of the fluid unchanged in the bulk phases. In that respect, all the modifications of the thermodynamics and mechanics of the interface are to be restrained to the binodal region only. The final expression of the variables in the TIM method, refereed to with the exponent $^{\text{TIM}}$, can be detailed. First, the variables that are not impacted by capillary contributions, such as P, s, μ, etc...,

Physics of Fluids
ACCEPTED MANUSCRIPT
This is the author's peer reviewed, accepted manuscript. However, the online version of record will be different from this version once it has been copyedited and typeset.
PLEASE CITE THIS ARTICLE AS DOI: 10.1063/5.0048715
AIP Publishing

only endure the modification from the EoS. For instance, the new EoS pressure and specific entropy are given by:

$$P^{\mathrm{TIM}} = \begin{cases} P^{\mathrm{sat}} + \dfrac{P^{\mathrm{EoS}} - P^{\mathrm{sat}}}{\phi_s} = P^{\phi_s} & \text{in the binodal region} \\ P^{\mathrm{EoS}} & \text{otherwise} \end{cases}$$

$$s^{\mathrm{TIM}} = \begin{cases} s^{\phi_s} & \text{in the binodal region} \\ s^{\mathrm{EoS}} & \text{otherwise} \end{cases}$$

As previously mentioned, the coefficient ϕ_l is applied to the capillary coefficient leading to the expression:

$$\lambda^{\mathrm{TIM}} = \begin{cases} \phi_l \lambda_0 & \text{in the binodal region} \\ \lambda_0 & \text{otherwise} \end{cases}$$

Therefore, thermodynamic variables impacted by both λ and the EoS, such as P^{th}, p, e_s, etc... endure both modifications. For instance, the new mechanical pressure and specific internal energy are given by

$$p^{\mathrm{TIM}} = \begin{cases} P^{\phi_s} - \dfrac{\phi_l \lambda_0}{2} \left[(\boldsymbol{\nabla} \rho)^2 + 2\rho \boldsymbol{\Delta} \rho \right] & \text{in the bin. reg.} \\ P^{\mathrm{EoS}} - \dfrac{\lambda_0}{2} \left[(\boldsymbol{\nabla} \rho)^2 + 2\rho \boldsymbol{\Delta} \rho \right] & \text{otherwise} \end{cases}$$

$${e_s}^{\mathrm{TIM}} = \begin{cases} {e_s}^{\phi_s} + \dfrac{\phi_l \lambda_0}{2\rho} (\boldsymbol{\nabla} \rho)^2 & \text{in the bin. reg.} \\ {e_s}^{\mathrm{EoS}} + \dfrac{\lambda_0}{2\rho} (\boldsymbol{\nabla} \rho)^2 & \text{otherwise} \end{cases}$$

All things considered, the new Euler equations can be formulated in the framework of the TIM. Practically, no formal modification is applied to the set Eqs.(7a)-(7c). It is only the global thermodynamic modification of the TIM that has to be included in order to get the new system. This is achieved by substituting p, λ^0 and E with p^{TIM}, λ^{TIM} and $E^{\mathrm{TIM}} = {e_s}^{\mathrm{TIM}} + \mathrm{v}^2/2$, to get the following equations:

$$\frac{\partial \rho}{\partial t} = -\boldsymbol{\nabla} \cdot [\rho \mathrm{v}] \tag{46a}$$

$$\frac{\partial \rho \mathrm{v}}{\partial t} = -\boldsymbol{\nabla} \cdot \left[\rho \mathrm{v} \otimes \mathrm{v} + p^{\mathrm{TIM}} \underline{\underline{\mathbf{I}}} + \lambda^{\mathrm{TIM}} \boldsymbol{\nabla} \rho \otimes \boldsymbol{\nabla} \rho \right] \tag{46b}$$

$$\frac{\partial \rho E^{\mathrm{TIM}}}{\partial t} = -\boldsymbol{\nabla} \cdot \left[\left(\rho E^{\mathrm{TIM}} + p^{\mathrm{TIM}} \right) \mathrm{v} + \lambda^{\mathrm{TIM}} (\boldsymbol{\nabla} \rho \otimes \boldsymbol{\nabla} \rho) \cdot \mathrm{v} + \lambda^{\mathrm{TIM}} \rho \boldsymbol{\nabla} \rho (\boldsymbol{\nabla} \cdot \mathrm{v}) \right] \tag{46c}$$

This result is of a high importance from a numerical point of view because it implies that only the thermodynamic routines of the code have to be modified to transit from the native Second Gradient to the TIM-modified system, thus greatly reducing the implementation difficulties.

5. Additional considerations on the TIM

As both Jamet's thickening methods, the Thickened Interface Method (TIM) requires the calculation of the saturation values (pressure and densities) together with a manner to discriminate the stable/unstable nature of the current thermodynamic regime and detect whether the modification is to be applied or not. This is done using a thermodynamic equilibrium solver: the saturation values are retrieved by equalizing the chemical potential of the liquid and vapor states at a given temperature.

Finally, since most of the time one wants to keep the surface tension unmodified while applying a thickening factor F to the interface, the dependencies Eq. (45) becomes $\sqrt{\phi_l/\phi_s} = 1$ and $\sqrt{\phi_l \phi_s} = \mathrm{F}$. It leads to the following expressions for ϕ_l and ϕ_s which will remain unchanged in the rest of the study:

$$\phi_l = \phi_s = \sqrt{\mathrm{F}} \tag{47}$$

IV. NUMERICAL VALIDATIONS OF THE TIM

A. Setup

1. Numerical setup

The Second Gradient theory model has been implemented in the semi-academic code AVBP developed jointly by CERFACS and IFPEN with specific modules from EM2C laboratory. It is designed to solve the Euler/Navier-Stokes equations on 2D/3D unstructured meshes for compressible flows with real gas thermodynamics. We used the SRK EoS given by Eq. (1), a third order Galerkin spatial discretization and a second order Runge-Kutta time integration. The Navier-Stokes Characteristic Boundary Conditions from 77 are used at inlets and outlets. Additionally, a high order conservative selective filter, inspired by 78, has been applied to suppress the point-to-point numerical oscillations.

2. Physical setup

In the objective of validating the approach described in the TIM, a wide variety of tests have been carried out in one and two dimensional configurations using different sets of equations accounting for more or less physical phenomenon. For the sake of conciseness, canonical one-dimensional cases are omitted in order to focus on the more interesting two-dimensional cases. These one-dimensional cases include the advection of isothermal and non-isothermal interfaces with and without viscosity, the return to equilibrium of deformed (either compressed or stretched) interfaces in the same diverse conditions and the vanishing through evaporation, and creation through condensing, of conductive interfaces.

As the validation of the TIM is done mostly via comparisons with theoretical results and given that these results are exclusively derived under isothermal conditions, for which the saturation values and surface tension are fixed, most of the two-dimensional configurations presented hereafter are computed solving isothermal sets of equations unless mentioned otherwise. In these isothermal cases, the energy equation is to

Physics of Fluids
ACCEPTED MANUSCRIPT
This is the author's peer reviewed, accepted manuscript. However, the online version of record will be different from this version once it has been copyedited and typeset.
PLEASE CITE THIS ARTICLE AS DOI: 10.1063/5.0048715
AIP Publishing

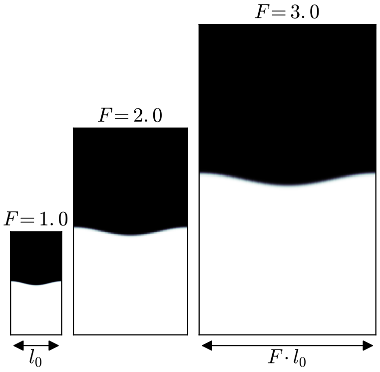

FIG. 8. Evolution of the initial density profiles for interfaces with different thickening factors, a fixed relative interface perturbation and a proportionally expanded geometry. In this figure, for the sake of clarity, the relative scales of the different configurations are respected and thus represented for small factors only. However, for the results presented hereafter, the methodology is used for factors up to F $= 10^4$

be discarded and the system (46a)-(46c) reduces to the mass and momentum equations.

3. *Case design*

The selected validation case is an oscillating plane interface initially deformed by a harmonic longitudinal perturbation as illustrated in Fig. (8) for low thickening factors. The wavelength of the perturbation is reduced to one period in the domain so that the local curvature radius of the interface remains substantially higher than the interface thickness. Moreover, the amplitude A of the perturbation has been kept low in order to remain in the linear deformation regime. With these settings, the interface is expected to oscillate almost indefinitely since no dissipation, apart from the numerical diffusion, is integrated in the equations.

The test cases exposed in Fig. (8), have been carefully designed to ensure the validity of the comparisons. First, we established a reference case on a numerically affordable mesh, the amplitude $A \approx 0.05l$ allowed for substantial oscillations without stepping out of the linear regime. The other cases were then obtained by applying an expansion $\delta =$ F to the whole geometry while simultaneously thickening the interface by a factor F. The relative amplitude of the imposed deformation (5%) remained unchanged. The fluid used is nitrogen and the full set of parameters used for this configuration is compiled in Tab. (III) where w_0 and l_0 are the interface and domain width when no thickening is applied.

Since we ensured that all the cases were homothetic, they are expected to mimic the reference case. Besides, by applying the same expansion to the mesh step size, we ensured a constant computational time for the same number of iterations throughout all cases. Though at first sight this design is expected to alter the oscillation period, theoretical correlations allow to predict the evolution of said period with the modification of the geometry. This strategy was eventually adopted to validate the 2D implementation of the Second Gradient model in the solver but also the behavior of the TIM regarding the dynamics of the interface.

TABLE I. Simulation parameters used for the additional tests of an oscillating two dimensional N_2 planar interface thickened with the TIM

T [K]	119.88	λ $\left[\mathrm{m}^7.\mathrm{kg}^{-1}.\mathrm{s}^{-2}\right]$	$\lambda_0 = 1.0 \cdot 10^{-16}$
P^{sat} [bar]	25.20	w_0 [nm]	6.34
ρ_l $\left[\mathrm{kg} \cdot \mathrm{m}^3\right]$	458.94	σ $\left[\mathrm{mN} \cdot \mathrm{m}^{-1}\right]$	1.18
ρ_v $\left[\mathrm{kg} \cdot \mathrm{m}^3\right]$	125.22	points in int.	≈ 10

B. Non-viscous simulations

1. *Isothermal simulations*

Solving the non-viscous isothermal equations, the overall expected behavior of the interface is properly retrieved as shown in Fig. (9) for F $= 50$ where the profile undergoes a well-defined oscillatory motion. The period of oscillation has been extracted by monitoring the time evolution of the density at the center of the domain, with an example given for F $= 50$ in Fig. (10).

From the authors in 79 one gets that the expected frequency of the oscillations ω obeys Eq. (48) where ρ_{u} (resp. ρ_{d}) and h_{u} (resp. h_{d}) are the density and width of the upper (res. lower) fluid, σ the surface tension of the interface, g the gravity acceleration and k the wavenumber of the deformation. Noticeably, it does not depend on the amplitude of the initial deformation.

$$\omega^2 = \frac{(\rho_{\mathrm{d}} - \rho_{\mathrm{u}})\, gk + \sigma k^3}{\rho_{\mathrm{d}} \coth kh_{\mathrm{d}} + \rho_{\mathrm{u}} \coth kh_{\mathrm{u}}} \tag{48}$$

In our configuration, no gravity is considered, the upper and lower densities are the saturation densities ρ_v and ρ_l, only one period of a sine is used for the deformation therefore $k = 2\pi/l$ where l is the domain width i.e. the length of the interface when no perturbation is applied and the upper and lower widths h_{u}, h_{d} have been chosen so that $h_{\mathrm{u}} = h_{\mathrm{d}} = 1.5l$. The simplified expression for the period is now given by Eq. (49).

$$\tau = \frac{l^{3/2}}{\sigma^{1/2}} \sqrt{\frac{\coth(1.5)\,(\rho_l + \rho_v)}{2\pi}} \tag{49}$$

The simulations have been performed for different values of the thickening factor F ranging from 1 to 10^4. Each

Physics of Fluids
ACCEPTED MANUSCRIPT
This is the author's peer reviewed, accepted manuscript. However, the online version of record will be different from this version once it has been copyedited and typeset.
PLEASE CITE THIS ARTICLE AS DOI: 10.1063/5.0048715

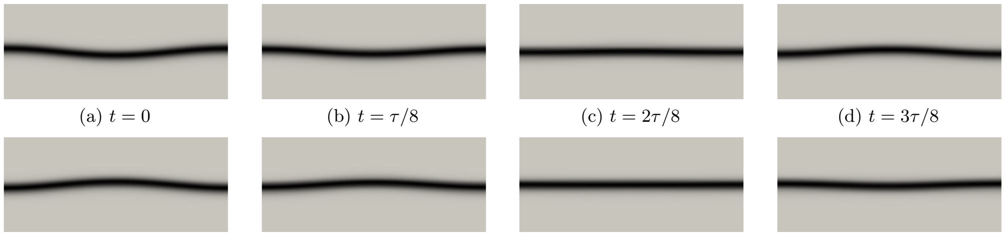

(a) $t = 0$ (b) $t = \tau/8$ (c) $t = 2\tau/8$ (d) $t = 3\tau/8$

(e) $t = 4\tau/8$ (f) $t = 5\tau/8$ (g) $t = 6\tau/8$ (h) $t = 7\tau/8$

FIG. 9. Zoom on the normalized density gradient profiles at different instants for the oscillation of an initially harmonically perturbed plane nitrogen N_2 interface with $T_{init} = 119.88$ K, $\lambda_0 = 1.0 \cdot 10^{-16}$ m^7.kg^{-1}.s^{-2} and F = 50

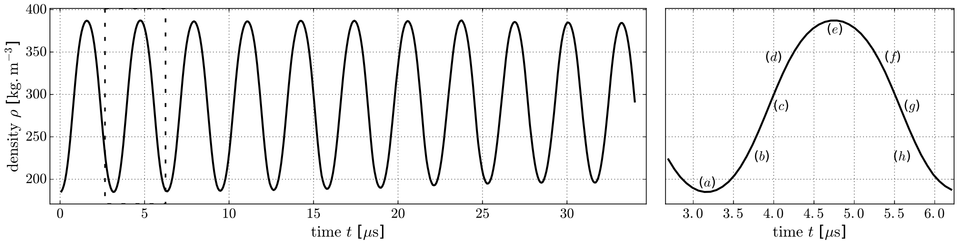

FIG. 10. Time evolution of the density at the center of the domain for the oscillation of an initially harmonically perturbed plane nitrogen N_2 interface with $T_{init} = 119.88$ K, $\lambda_0 = 1.0 \cdot 10^{-16}$ m^7.kg^{-1}.s^{-2} and F = 50

time, the thickening of the interface has been achieved in two different ways: firstly by only multiplying the capillary coefficient λ by ${\phi_l}^2$ and secondly by using the TIM with the combined actions of ϕ_s and ϕ_l. The results are given in Fig. (11).

From Eq. (31) one knows that thickening the interface by a factor F using only the coefficient ϕ_l will result in the same factor being applied to the surface tension and therefore, from Eq. (49) it can be concluded that the period should behave as shown by Eq. (50). This expected result is symbolized by the dashed line in Fig. (11). The adjective "inconsistent" will be used in the following to qualify this method as it should not conserve the value of σ.

$$\frac{\tau^{\phi_l}}{\tau_0} = \frac{(\mathrm{F}l_0)^{3/2}}{(\mathrm{F}\sigma_0)^{1/2}}\frac{{\sigma_0}^{1/2}}{{l_0}^{3/2}} = \mathrm{F} \tag{50}$$

The same *a priori* estimation of the period evolution can be done with Eq. (49) for the TIM supposed to thicken the interface by a factor F without modifying its surface tension, obtaining Eq. (51). This expected behavior is symbolized with a solid line in Fig. (11).

$$\frac{\tau^{\mathrm{TIM}}}{\tau_0} = \frac{(\mathrm{F}l_0)^{3/2}}{{\sigma_0}^{1/2}}\frac{{\sigma_0}^{1/2}}{{l_0}^{3/2}} = \mathrm{F}^{3/2} \tag{51}$$

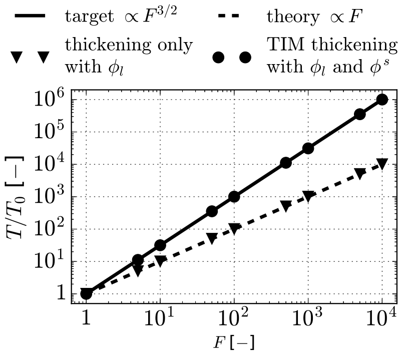

FIG. 11. Evolution of the interface oscillation period normalized by $T_{\mathrm{F}=1}$, with the thickening coefficient F (in log scale) for consistent and inconsistent thickening strategies, comparison with numerical results using the inconsistent and TIM methods

a. The two behaviors obtained with Eqs. (50) and (51) are accurately retrieved in the simulations. The results for the "inconsistent" thickening method using only ϕ_l further

Physics of Fluids ACCEPTED MANUSCRIPT
This is the author's peer reviewed, accepted manuscript. However, the online version of record will be different from this version once it has been copyedited and typeset.
PLEASE CITE THIS ARTICLE AS DOI: 10.1063/5.0048715
AIP Publishing

demonstrate the predictive capabilities of the native Second Gradient model and its proper implementation in the code AVBP. Likewise, the results obtained with the TIM offer an additional validation for its mechanical consistency. The exact numerical values of these different periods for both thickening approaches are compiled in Tab. (II) and the relative errors between the theory and the simulations never exceed 5 % which represents a very satisfactory result.

Given the manner the TIM has been derived, its application is not restrained to pure fluid or to temperatures extremely close to T_c. Besides, the shape of the pressure/chemical potential is not analytically prescribed in the binodal region. This should ensure the applicability to mixtures for which the pressure/chemical potential cannot be obtained analytically due to the complex dependencies with the mixture fractions.

2. Non-isothermal simulations

Despite the lack of theoretical results, attempts have been made to qualify the behavior of the TIM in non-isothermal configurations. To that effect, the same previous cases have been computed, using the same isothermal initial solutions but this time by solving the complete system of equations as expressed in Eqs. (46a)-(46c), i.e. including the energy equation. The central density oscillation curves are given in Fig. (12) for $\mathrm{F} = 10$ and $\mathrm{F} = 1000$.

Noticeably, the curves superimpose satisfyingly, meaning that the correlation for the surface tension preservation from Eq. (51) is still observed by the model.

To widen the range of application of the method, simulations with non-isothermal initial solutions have been carried out. The same framework as in Sec. IV A 3 has been used however this time a non-constant temperature evolution is imposed outside of the interfacial zone so as to get an actual non-isothermal configuration as shown in Fig. (13). Essentially, the liquid is over-cooled while the vapor is overheated to create bulk phases outside the edges of the binodal region. The initial solutions are designed so as to get a constant pressure outside the interface, equal to the saturation pressure associated to the interface temperature, to prevent acoustics driven movements.

The evolution of the central density in this configuration is similar to that of the case with an isothermal initial solution with the addition of mild numerical noise. We suspect this noise to be caused by the imperfections of the initial solutions given the difficulty to produce a perfectly isobaric interface and to consistently thicken a non-isothermal interface.

Nonetheless, whether an isothermal or a non-isothermal initial solution is used, when solving the non-isothermal set of equations, the periods of oscillation follow the same trend as the one observed for the fully isothermal configuration. This result is visible in the graphs of Fig. (14) where the nondimensionalized periods have been extracted for different thickening factors, the correlation $\tau \propto \mathrm{F}^{1.5}$ is mostly retrieved. Overall, these simplified non-isothermal cases showcased a good agreement with the theory and further validated the TIM methodology.

C. Viscous simulations

To further the quantitative comparisons with the literature, dissipation has been introduced in the simulations via the addition of physical viscosity, using the same design of an oscillating planar interface, now with damping. The available theoretical results require a specific set of conditions, namely: an isothermal setting, an important liquid-to-vapor density ratio and a constant value of kinematic viscosity $\nu = \mu/\rho$. To comply with these conditions, a slightly modified configuration has been preferred with an oxygen interface at a lower temperature using the parameters compiled in Tab. (III) where w_0 and l_0 are the interface and domain width when no thickening is applied.

Accordingly, the momentum equation in Eq. (46b) becomes:

$$\begin{aligned}\frac{\partial \rho \mathrm{v}}{\partial t} = -\boldsymbol{\nabla}\cdot\Big[&\rho\mathrm{v}\otimes\mathrm{v} + p^{\mathrm{TIM}}\underline{\underline{\mathbf{I}}} + \lambda^{\mathrm{TIM}}\boldsymbol{\nabla}\rho\otimes\boldsymbol{\nabla}\rho \\ &+\rho\nu\left(\left(\boldsymbol{\nabla}\mathrm{v} + \boldsymbol{\nabla}\mathrm{v}^{\mathrm{T}}\right) - \left(\boldsymbol{\nabla}\cdot\mathrm{v}\right)\underline{\underline{\mathbf{I}}}\right)\Big]\end{aligned} \tag{52}$$

With this configuration and set of equations, three series of simulations have been performed using three values of thickening coefficients $\mathrm{F} = 1$, $\mathrm{F} = 100$ and $\mathrm{F} = 10000$, applying the TIM to thicken the interface while simultaneously increasing the dimensions of the domain following the principle exposed in Fig. (8). For all thickening factors, three values of kinematic viscosity, compiled in Tab. (IV), have been chosen to obtain the same Laplace numbers $La = (\sigma l)/(\rho\nu^2)$ from one thickening to the other.

The time evolution of the central density for all thickening factors is similar to that of Fig. (12) where a noticeable damping of the oscillation can be observed, as expected from the added viscosity. The correlation $\tau \propto \mathrm{F}^{1.5}$ is still perfectly preserved and for the same Laplace number, the curves for different thickening factors using the adjusted abscissa $t/\mathrm{F}^{1.5}$ are essentially indistinguishable from one another. These encouraging initial observations are strengthened once the values of the oscillation period τ and characteristic damping time δ are extracted by following the interface during its movement, i.e. the time evolution of the position for the central point of the interface.

From Prosperetti in 80, approximate values of the oscillation pulsation and damping in presence of viscosity, respectively ω_ν and δ_ν, can be obtained using Eqs. (53)-(54) where $k = 2\pi/l$ is the spacial period and ω_0 the non-viscous pulsation is given by Eq. (48).

$$\omega_\nu^2 = \omega_0^2 - 4\nu^2 k^4 \tag{53}$$

$$\delta_\nu = \frac{1}{2\nu k^2} \tag{54}$$

The simulation and theoretical values for the period τ and characteristic damping time δ are compiled and compared in

ACCEPTED MANUSCRIPT
Physics of Fluids
This is the author's peer reviewed, accepted manuscript. However, the online version of record will be different from this version once it has been copyedited and typeset.
PLEASE CITE THIS ARTICLE AS DOI: 10.1063/5.0048715
AIP Publishing

TABLE II. Comparison between theoretical and simulation oscillating periods for the "inconsistent" and TIM thickening strategies

F	1	5	10	50	100	500	1000	5000	10000
$\tau_{\phi_l\,\mathrm{th}}$ [ns]	17.14	85.7	171.4	857.0	$1.714\cdot10^3$	$8.57\cdot10^3$	$17.14\cdot10^3$	$85.70\cdot10^3$	$17.14\cdot10^3$
$\tau_{\phi_l\,\mathrm{sim}}$ [ns]	17.98	89.79	179.8	898.7	$1.80\cdot10^3$	$8.98\cdot10^3$	$17.9\cdot10^3$	$89.8\cdot10^3$	$179.7\cdot10^3$
error_{ϕ_l} [%]	3.62	4.77	4.87	4.87	4.86	4.83 %	4.85	4.82	4.83
$\tau_{\mathrm{TIM\,th}}$ [ns]	17.14	191.6	542.0	$6.06\cdot10^3$	$17.14\cdot10^3$	$191.6\cdot10^3$	$542.0\cdot10^3$	$6.06\cdot10^6$	$17.14\cdot10^6$
$\tau_{\mathrm{TIM\,sim}}$ [ns]	17.9	200.7	569.4	$6.37\cdot10^3$	$18.02\cdot10^3$	$201.1\cdot10^3$	$559.2\cdot10^3$	$6.36\cdot10^6$	$18.01\cdot10^6$
error_{ϕ_l} [%]	3.63	4.75	5.05	5.12	5.16	4.93	3.18	4.75	5.12

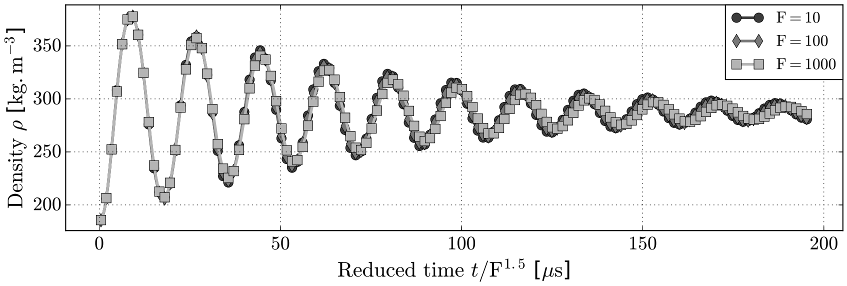

FIG. 12. Time evolution of the density at the center of the domain for the oscillation of an initially harmonically perturbed plane N_2 interface with $T_i = 100$ K, $\lambda_0 = 1.0\cdot10^{-16}$ m^7.kg^{-1}.s^{-2}. The intial solution is isothermal but the non-isothermal equations system is solved for different thickening factors

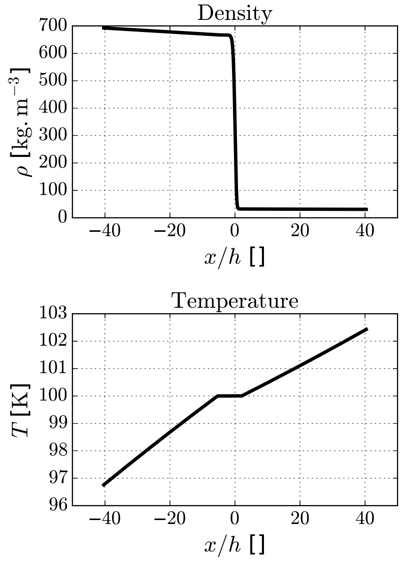

FIG. 13. 1D density *(left)* and temperature *(right)* profiles for initially isobaric oscillating N_2 planar interface with $P^{\mathrm{sat}} = 7.85$ bar and $\lambda_0 = 1.0\cdot10^{-16}$ m^7.kg^{-1}.s^{-2}

TABLE III. Simulation parameters used for the additional tests of an oscillating two dimensional O_2 planar interface thickened with the TIM

T [K]	110	λ [m^7.kg^{-1}.s^{-2}]	$\lambda_0 = 1.173\cdot10^{-17}$
P^{sat} [bar]	5.45	w_0 [nm]	0.97
ρ_l [kg$\cdot$m^3]	1017.7	σ [mN$\cdot$m^{-1}]	8.37
ρ_v [kg$\cdot$m^3]	21.4	$L_{x,0} = L_{y,0}/3 = l_0$ [nm]	26
points in int.	≈ 8	N_x	218

TABLE IV. Laplace numbers and corresponding values of kinematic viscosity to perform simulation-theory comparisons for an oscillating isothermal oxygen interface at 110 K using different thickening factors in the TIM

La	$2.0\cdot10^5$	$2.0\cdot10^4$	$2.0\cdot10^3$
$\nu_{\mathrm{F}=1}$ [m$^2\cdot$s^{-1}]	$1.0\cdot10^{-9}$	$3.3\cdot10^{-9}$	$1.0\cdot10^{-8}$
$\nu_{\mathrm{F}=100}$ [m$^2\cdot$s^{-1}]	$1.0\cdot10^{-8}$	$3.3\cdot10^{-8}$	$1.0\cdot10^{-7}$
$\nu_{\mathrm{F}=10000}$ [m$^2\cdot$s^{-1}]	$1.0\cdot10^{-7}$	$3.3\cdot10^{-7}$	$1.0\cdot10^{-6}$

Tabs. V, VI and VII for thickening factors $\mathrm{F} = 1$, $\mathrm{F} = 100$ and $\mathrm{F} = 10000$ respectively. The comparisons are very satisfactory overall, in particular for the oscillation period, which lend a maximal error lower than 5% for all thickening factors. For

Physics of Fluids

ACCEPTED MANUSCRIPT

This is the author's peer reviewed, accepted manuscript. However, the online version of record will be different from this version once it has been copyedited and typeset.

PLEASE CITE THIS ARTICLE AS DOI: 10.1063/5.0048715

AIP Publishing

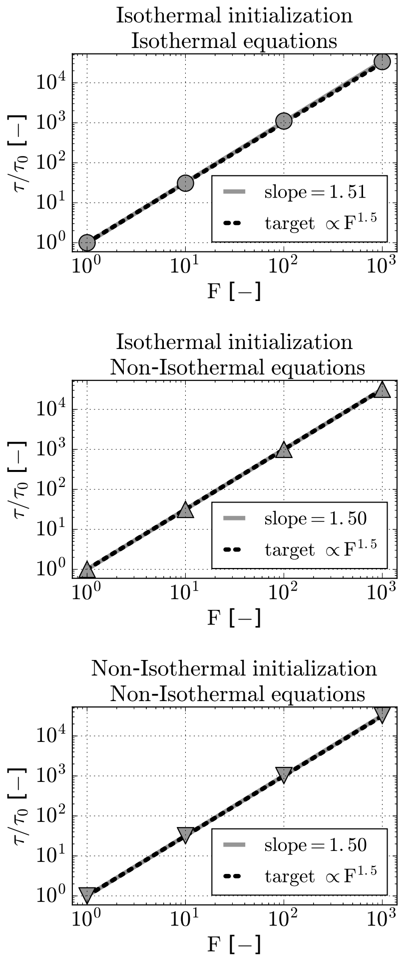

FIG. 14. Evolution of the normalized interface oscillation period, with the thickening coefficient F (in log scale) for different types of initialization and equations solving

the characteristic damping time, the errors place around 20% in average which still constitutes a very satisfactory result.

TABLE V. Oscillation periods and characteristic damping times, from theory and simulations, for an oscillating isothermal oxygen interface at 110 K for different values of kinematic viscosity

ν $[\mathrm{m}^2\cdot\mathrm{s}^{-1}]$	$1.0\cdot10^{-9}$	$3.3\cdot10^{-9}$	$1.0\cdot10^{-8}$
$\tau_{\nu,\mathrm{th}}$ [ns]	0.589	0.591	0.599
$\tau_{\nu,\mathrm{sim}}$ [ns]	0.566	0.568	0.586
error_τ [%]	4.1	4.0	2.6
$\delta_{\nu,\mathrm{th}}$ [ns]	9.04	2.87	1.03
$\delta_{\nu,\mathrm{sim}}$ [ns]	8.73	2.54	0.916
error_δ [%]	3.5	13.0	12.7

TABLE VI. Oscillation periods and characteristic damping times, from theory and simulations, for an oscillating isothermal oxygen interface at 110 K for different values of kinematic viscosity. Results obtained with a thickening factor $F = 100$ applied following the TIM

ν $[\mathrm{m}^2\cdot\mathrm{s}^{-1}]$	$1.0\cdot10^{-8}$	$3.3\cdot10^{-8}$	$1.0\cdot10^{-7}$
$\tau_{\nu,\mathrm{th}}$ [μs]	0.589	0.591	0.599
$\tau_{\nu,\mathrm{sim}}$ [μs]	0.566	0.568	0.585
error_τ [%]	4.1	4.0	2.5
$\delta_{\nu,\mathrm{th}}$ [μs]	9.04	2.87	1.03
$\delta_{\nu,\mathrm{sim}}$ [μs]	7.62	2.30	0.868
error_δ [%]	18.6	25.1	18.9

Going a step further, the author in 80 derives the actual analytical expression of the time evolution for the normalized interface displacement when the constant kinematic viscosity condition is respected. Fig. (15) presents the time evolution of said normalized interface displacement comparing the theory and the simulations for a thickening factor $F = 10000$. As expected from the errors in Tab. (VII), the results are very satisfying, even more so since no approximation is used for the calculation of these theoretical curves. This quality in the accordance between the theory and the simulations is the same for the other thickening factors $F = 1$ and $F = 100$. It represents a strong argument in favor of the Second Gradient theory and more specifically the TIM regarding its ability to describe the behavior of isothermal interfaces even in presence of viscosity and reinforces its pertinence and consistency as a tool to model realistic interfaces in such conditions.

V. APPLICATIONS OF THE TIM

Based on the promising comparative results of the previous section, we propose in the following to apply the TIM to two more challenging configurations, both oriented towards the modeling of liquid-gas spray which is one of the ultimate objective pursued by the derivation of this new model. We

TABLE VII. Oscillation periods and characteristic damping times, from theory and simulations, for an oscillating isothermal oxygen interface at 110 K for different values of kinematic viscosity. Results obtained with a thickening factor $F = 10000$ applied following the TIM

ν $[\mathrm{m}^2\cdot\mathrm{s}^{-1}]$	$1.0\cdot10^{-7}$	$3.3\cdot10^{-7}$	$1.0\cdot10^{-6}$
$\tau_{\nu,\mathrm{th}}$ [s]	0.589	0.591	0.599
$\tau_{\nu,\mathrm{sim}}$ [s]	0.567	0.568	0.585
error_τ [%]	4.1	4.0	2.4
$\delta_{\nu,\mathrm{th}}$ [s]	9.04	2.87	1.03
$\delta_{\nu,\mathrm{sim}}$ [s]	7.73	2.31	0.874
error_δ [%]	16.9	24.3	17.9

Physics of Fluids

ACCEPTED MANUSCRIPT

This is the author's peer reviewed, accepted manuscript. However, the online version of record will be different from this version once it has been copyedited and typeset.

PLEASE CITE THIS ARTICLE AS DOI: 10.1063/5.0048715

AIP Publishing

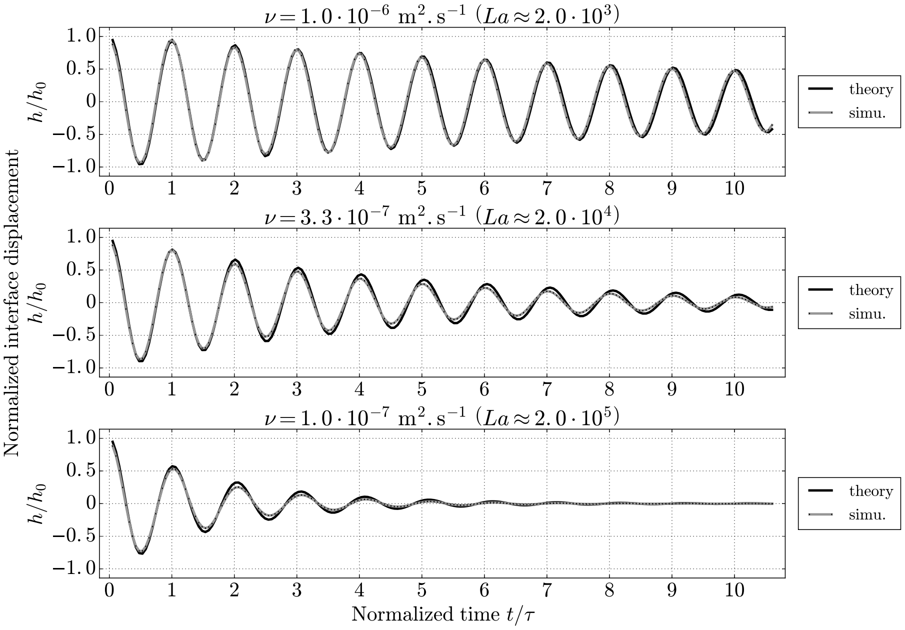

FIG. 15. Comparison between the theory and simulation results for the normalized displacement of a two-dimensional isothermal planar oscillating oxygen interface. A thickening factor F = 10000 is applied following the TIM.

recall that all the results presented in this section have been obtained solving the full set of non-isothermal Navier-Stokes equations with the TIM-modified Second Gradient model as described in Eqs. (46a) - (46c). Physical diffusion is also introduced in the form of viscosity in both the momentum and energy equations and thermal conduction in the energy equation. The system is eventually given by Eqs. (55a)-(55c) where the model from Chung presented in 81 is used to evaluate the diffusion coefficients, i.e. the dynamic viscosity and the thermal conduction coefficients.

$$\frac{\partial \rho}{\partial t} = -\boldsymbol{\nabla} \cdot [\rho \mathrm{v}] \tag{55a}$$

$$\frac{\partial \rho \mathrm{v}}{\partial t} = -\boldsymbol{\nabla} \cdot \Big[\rho \mathrm{v} \otimes \mathrm{v} + p^{\mathrm{TIM}} \underline{\underline{\mathbf{I}}} + \lambda^{\mathrm{TIM}} \boldsymbol{\nabla}\rho \otimes \boldsymbol{\nabla}\rho - \underline{\underline{\boldsymbol{\tau}}}^{d}\Big] \tag{55b}$$

$$\frac{\partial \rho E^{\mathrm{TIM}}}{\partial t} = -\boldsymbol{\nabla} \cdot \Big[\left(\rho E^{\mathrm{TIM}} + p^{\mathrm{TIM}}\right) \mathrm{v} + \lambda^{\mathrm{TIM}} \left(\boldsymbol{\nabla}\rho \otimes \boldsymbol{\nabla}\rho\right) \cdot \mathrm{v} + \lambda^{\mathrm{TIM}} \rho \boldsymbol{\nabla}\rho \left(\boldsymbol{\nabla} \cdot \mathrm{v}\right) - \underline{\underline{\boldsymbol{\tau}}}^{d} : \mathrm{v} + \boldsymbol{q}\Big] \tag{55c}$$

A. Colliding droplets

1. Case design

Among the important characteristics of a spray, the mechanisms controlling the droplets creation and their size distribution are of particular interest. As such, the ability to simulate the dynamic behavior of droplets is primordial in order to access more macroscopic configurations and it has motivated the simulation scenario presented in the next paragraph. The configuration consists in the collision of two three-dimensional droplets as represented in Fig. (16).

The outcome of such collisions has been thoroughly investigated experimentally by the likes of 82–86 and has been shown to be, for the most part, controlled by the size ratio $\Delta = R_1/R_2$ between the droplets, the liquid Weber number $We = \rho_l D_2 (2\mathrm{v})^2/\sigma$ associated with the bigger droplet (v is the norm of the velocity of both droplets) and the impact parameter $\delta = d/(R_1+R_2)$. Our simulations are limited to head-on collisions ($\delta = 0$) of same-sized ($R_1 = R_2 = R$ or equivalently $\Delta = 1$) oxygen droplets. The corresponding three-dimensional initial solution (density isosurface at $\rho = 500\ \mathrm{kg \cdot m^3}$) with the relevant two-dimensional fields of reference (density, pressure, normalized velocity) are given in

Physics of Fluids

ACCEPTED MANUSCRIPT

This is the author's peer reviewed, accepted manuscript. However, the online version of record will be different from this version once it has been copyedited and typeset.

PLEASE CITE THIS ARTICLE AS DOI: 10.1063/5.0048715

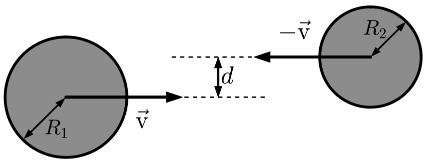

FIG. 16. Schematic representation of the configuration used to study the collision of two droplets

TABLE VIII. Parameters used for the three-dimensional simulations of colliding O_2 droplets

T_i [K]	110.0	P^{sat} [bar]	5.45
λ_0 $\left[\mathrm{mm}^7 \cdot \mathrm{g}^{-1} \cdot \mathrm{s}^{-2}\right]$	11.73	w [μm]	0.97
ρ_l $\left[\mathrm{kg} \cdot \mathrm{m}^3\right]$	1017.7	μ_l [Pa.s]	$1.05 \cdot 10^{-5}$
ρ_v $\left[\mathrm{kg} \cdot \mathrm{m}^3\right]$	21.4	μ_v [Pa.s]	$8.20 \cdot 10^{-6}$
σ $\left[\mathrm{mN} \cdot \mathrm{m}^{-1}\right]$	8.37	D [μm]	20
$\Delta_x = \Delta_y$ [μm]	0.184	$L_y = L_x/2$ [μm]	55.0
points in diam.	≈ 150	$N_y = Nz = N_x/2$	300

Fig. (17).

The generic parameters used for the simulations are compiled in Tab. (VIII), periodic boundary conditions are used in the direction parallel to the droplets movement and partially relaxing inlets are used on the two other sides, perpendicularly to the droplets movement.

For such a configuration, several experimental results are available. However, the fluid considered is often water or occasionally some type of hydrocarbon. Using water, a precise We - δ regime graph has been produced by Ashgriz and Poo in 85.

To access the different collision regimes exposed in 85, several droplets velocities have been used, all the other characteristics of the configuration remaining equal. These velocities have led to different values of liquid Weber number $We = \rho_l \left(2\mathrm{v}\right)^2 D/\sigma$ and Reynolds number $Re = \rho_l \mathrm{v} D/\mu_l$. The Laplace number $La = \rho_l \sigma D/\mu_l$, which is not impacted by the changes in velocity, remains constant at $La = 1.545 \cdot 10^6$. The values of all these characteristic numbers are compiled in Tab. (IX). The full set of non-isothermal Navier-Stokes equations, modified by the TIM, are solved for all cases.

2. *Simulation results*

The results for the first simulation, done using Weber $We = 20$ (v $= 1.43$ m.s^{-1}), is presented in Fig. (18). The impact torus, the elongated cylinder and the final droplet, typical of the impacting coalescence regime, can be observed.

TABLE IX. Description of the three configurations simulated for the head-on collision of oxygen droplets in terms of velocity, Weber and Reynolds numbers

v $\left[\mathrm{m} \cdot \mathrm{s}^{-1}\right]$	1.43	2.03	2.87
We	20	40	80
Re	556	790	1100

In an effort to emulate the case from 85 at $We = 23$ and $\delta = 0.05$ where a satellite-free reflexive separation occurs, a second simulation, for which results are shown in Fig. (19), has been performed at Weber number $We = 40$ (v $= 2.03$ m.s^{-1}). For the most part, the scenario of the collision is well retrieved in the simulation. The persistence of a small satellite droplet between the post-collision departing droplets, which does not appear in the experiments, can however be noticed.

The question of obtaining reflexive separation without satellite droplets does not seem to be directly addressed in the literature. Such outcomes have been observed experimentally for water in air in 85 and numerically, still for water, using either LS methods in 87 and 88 or VOF methods in 89. Most other results involving different fluids, either experimentally or numerically, showcase reflexive separation with creation of at least a very small droplet in the center. In 85, the authors observed the same satellite-free reflexive separation over the range $19 \leqslant We \leqslant 23$.

To obtain a clearly defined single satellite droplet, reminiscent of the head-on collision at $We = 40$ from 85, a third simulation at $We = 80$ (v $= 2.87$ m.s^{-1}) has been performed, the comparative results are shown in Fig. (20).

As it was the case in Fig. (19), a very strong agreement is obtained, in terms of behavior, between the simulation and the experiment. The relative sizes of the two departing and the stagnant satellite droplets are also well predicted.

B. Periodic liquid jets

1. *Case design*

A second application case is presented, motivated by the introduction of more complexity. The configuration consists in a symmetrical nitrogen mixing layer that takes the aspect of a liquid jet in its own vapor. The surrounding vapor is initially at rest whereas the liquid has a constant descending vertical velocity v_l. The simulations are performed on a regular cartesian mesh. The domain, as depicted in Fig. (21), is periodic vertically and non-reflecting boundary conditions are used on the left and right boundaries. The useful parameters used for the simulations are compiled in Tab. (X) where D_0 and w_0 are the reference jet diameter and interface width for the reference thickening coefficient $\mathrm{F}_0 = 1000$ and the mesh resolution $\Delta_{x0} = 0.133$ μm

While the initial density, pressure and temperature profiles have remained unchanged for all cases, four different values of liquid velocity, compiled in Tab. (XI), have been used so

Physics of Fluids
ACCEPTED MANUSCRIPT
This is the author's peer reviewed, accepted manuscript. However, the online version of record will be different from this version once it has been copyedited and typeset.
PLEASE CITE THIS ARTICLE AS DOI: 10.1063/5.0048715

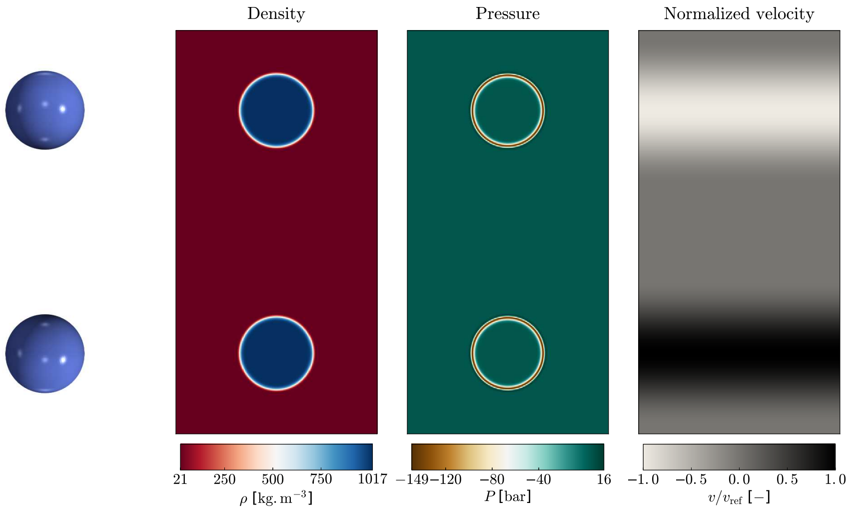

FIG. 17. Initial solution used to study the collision of same sized initially isothermal oxygen droplets in their own vapor. The three-dimensional $\rho = 500$ kg $\cdot$ m^3 isosurface and the reference two dimensional density, pressure and normalized density fields are provided.

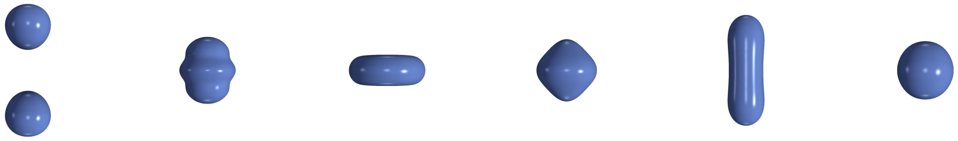

FIG. 18. Head-on collision of liquid droplets, simulation results with oxygen droplets at $We = 20$ ($Re_l = 556$) using the TIM

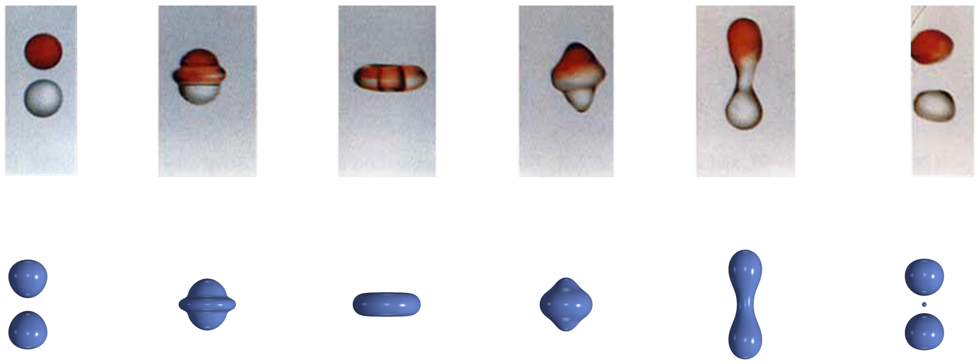

FIG. 19. Head-on collision of liquid droplets, comparison between experiments with water droplets at $We = 23$ from 85 and simulation results with oxygen droplets at $We = 40$ ($Re_l = 790$) using the TIM

ACCEPTED MANUSCRIPT

Physics of Fluids

This is the author's peer reviewed, accepted manuscript. However, the online version of record will be different from this version once it has been copyedited and typeset.

PLEASE CITE THIS ARTICLE AS DOI: 10.1063/5.0048715

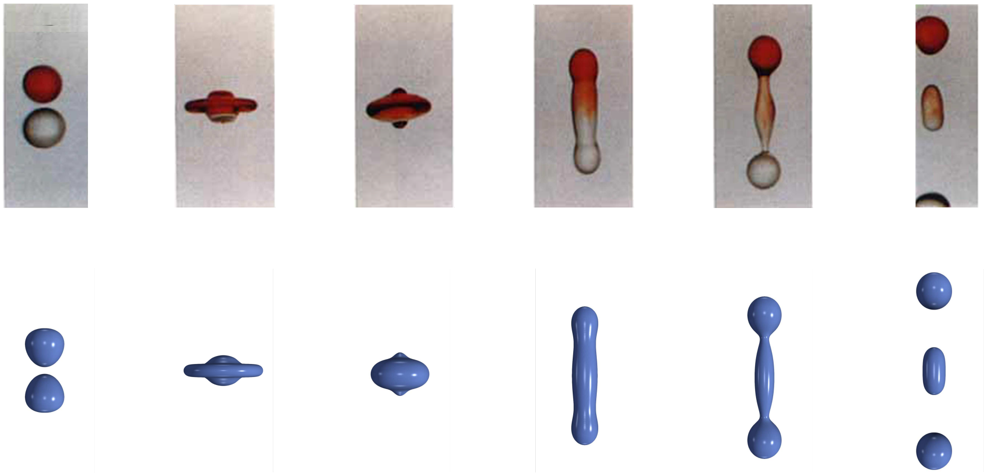

FIG. 20. Head-on collision of liquid droplets, comparison between experiments with water droplets at $We = 40$ from 85 and simulation results with oxygen droplets at $We = 80$ ($Re_l = 1100$) using the TIM

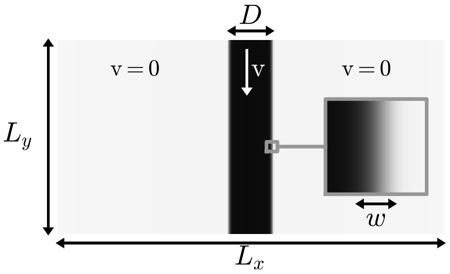

FIG. 21. Schematic representation of the density field for the simulation configuration

TABLE X. Simulation parameters used for the two-dimensional N_2 jets (reference mesh resolution and interface thickening leading to about nine points in the interface)

T_i [K]	100.0	$\lambda_{\mathrm{F}=0}$ $\left[\mathrm{mm}^7 \cdot \mathrm{g}^{-1} \cdot \mathrm{s}^{-2}\right]$	19.6
P^{sat} [bar]	7.85	σ $\left[\mathrm{mN} \cdot \mathrm{m}^{-1}\right]$	4.134
ρ_l $\left[\mathrm{kg} \cdot \mathrm{m}^3\right]$	667.14	F_0	1000
ρ_v $\left[\mathrm{kg} \cdot \mathrm{m}^3\right]$	31.6	$L_y = L_x/2$ [μm]	90.0
w_0 [μm]	1.31	$N_{y0} = N_{x0}/2$	675
D [μm]	20	$\Delta_{x0} = \Delta_{y0}$ [μm]	0.133

TABLE XI. Simulation velocities and corresponding liquid Reynolds, Weber and Ohnesorge numbers used for the two dimensional N_2 jets with a liquid viscosity $\mu_l = 3.25 \cdot 10^{-4}$ kg $\cdot$ m$^{-1} \cdot$ s^{-1}

v [m $\cdot$ s^{-1}]	11.3	17.9	25.4	35.9
Re	460	730	1040	1470
We	412	1030	2080	4150
Oh	$4.38 \cdot 10^{-2}$	$4.38 \cdot 10^{-2}$	$4.38 \cdot 10^{-2}$	$4.38 \cdot 10^{-2}$

as to get four different liquid Weber numbers $We = \rho_l v^2 D/\sigma$ and liquid Reynolds number $Re = \rho_l v D/\mu_l$ typical of different atomization regimes. With the physical parameters from the simulations, the resulting liquid Ohnesorge number $Oh = \mu_l/\sqrt{\rho_l \sigma D}$ number is constant at $4.38 \cdot 10^{-2}$.

The results from the simulation can be compared to the chart from Shimasaki and Taniguchi 90 and adapted in Fig. (22)) which provides insight on the jet behavior relatively to the couple (*Re* - *Oh*). The regime for the case with the lower *Re* number (460) corresponds to the first wind-induced regime while the case at $Re = 1470$ is laying in the second wind-induced regime.

We mention that the conditions in Tab. (X), in particular the liquid dynamic viscosity coefficient μ_l and the mesh step size Δ_{x0} have been chosen to ensure that the more extreme case at $Re = 1470$ leads to a Kolmogorov length scale of 0.153 μm, i.e. slightly greater than the mesh resolution Δ_{x0}.

2. Simulation results

Reference cases

The first aspect addressed with these simulations is the

Physics of Fluids ACCEPTED MANUSCRIPT

This is the author's peer reviewed, accepted manuscript. However, the online version of record will be different from this version once it has been copyedited and typeset.

PLEASE CITE THIS ARTICLE AS DOI: 10.1063/5.0048715

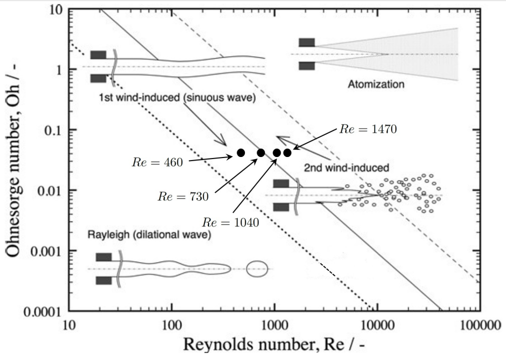

FIG. 22. Breakup regimes in the parameter space $\mathrm{Re}_l - \mathrm{Oh}$ extracted for a hydrocarbons-air mixture. Reproduced from S. Shimasaki and S. Taniguchi, "Formation of uniformly sized metal droplets from a capillary jet by electromagnetic force," Applied Mathematical Modelling 35, 1571-1580 (2011), with the permission of Elsevier.

impact of the jet velocity on its topology and behavior. A time evolution of the two-dimensional density profiles for all Reynolds numbers is presented in Fig. (23) for the reference spatial resolution. For $Re = 460$ $(We = 412)$ the jet faces a mild macroscopic deformation with no clear breakup in accordance with the first wind-induced regime in Fig. (22). For $Re = 730$ $(We = 1030)$, the deformation gets stronger and macroscopic ligaments start to form. For $Re = 1040$ $(We = 2080)$, these macroscopic structures also form and eventually start separating and coalescing. Both results are consistent with regimes in-between the first and second wind-induced regimes in Fig. (22). For $Re = 730$, a small number of big droplets are generated whereas for $Re = 1040$ only very large filaments are created and can be expected to quickly recombine without formation of smaller droplets.

With the case $Re = 1470$ $(We = 4150)$, a great modification occurs in the jet topology. Long macroscopic ligaments form and quickly break-up to form droplets among which the biggest ones also tend to experience a secondary break-up giving birth to smaller droplets. This result properly follows the behavior of a fully installed second wind-induced regime as predicted by Fig. (22).

Impact of the interface resolution

In a second aspect, the impact of the resolution has also been addressed in order to assess the response of the model to coarsely resolved interface in terms of quality of the results. To modify the interface resolution, two mechanisms can be used : either augmenting the mesh size while using the same interface width i.e. a preserved thickening coefficient or, conversely, reducing the thickening coefficient i.e. sharpening the interface with a preserved mesh size. Both approaches have been used following the parameters compiled in Tab. (XII) where the mesh size and thickening coefficient used are specified. The reference configuration is recalled and two coarser interface resolutions of approximately five and three points (i.e. factors a half and a third) have been used, compared to the reference interface resolution of approximately nine points. The two coarsening factors $1/2$ and $1/3$ have been obtained either by reducing the mesh size or the thickening factor.

TABLE XII. Mesh resolutions and thickening factor used to study the impact of the interface resolution on the simulations results for a two-dimensional N_2 jet in its own vapor

N_y	675	338	224	675	675
F	1000	1000	1000	500	333
Δ_x [μm]	0.133	0.267	0.404	0.133	0.133
points in int.	≈ 9	≈ 5	≈ 3	≈ 5	≈ 3

A brief time evolution of the density fields is provided in Figs. 24 and 25, for the three mesh resolutions and for the Reynolds numbers $Re = 1470$ $(We = 4150)$ and $Re = 730$ $(We = 1030)$ respectively when the thickening coefficient is maintained at $\mathrm{F} = 1000$.

The two immediate observations are that for the case $Re = 730$ $(We = 1030)$, the mesh resolution has little to no impact whereas in the more dynamic case $Re = 1470$ $(We = 4150)$, the interface diffusion that was merely noticeable, is now largely amplified by the use of a coarser mesh resolution to the point where a substantial part of the liquid has essentially disappeared by the end of the simulation on this coarser mesh. Even if the Second Gradient model introduces some new terms in the flow equations that can be interpreted as diffusive, its actual expected action is to diffuse the interface when it is submitted to a mechanical thinning, but conversely, to become anti-diffusive if the interface is mechanically stretched. From the point of view of the Second Gradient model, a diffusion as intense as seen in Fig. (24) should only apply if actual thermal diffusion and/or temperature increase justified the interface to actually become wider. Besides, not only the interface enlarges but the liquid eventually vanishes while the total mass of fluid is conserved. The complete mechanism behind this apparent diffusion is not well understood and constitutes an important focal point for further studies.

The same simulations have been performed reducing the thickening coefficient on the reference mesh size.

Some results are provided in Fig. (26) where the density fields at $Re = 1470$ $(We = 4150)$ are presented for the two strategies used to lower the interface resolution: a mesh resolution or a thickening factor divided by two to obtain a 5-point interface resolution (results in the leftmost images) and a mesh resolution or a thickening factor divided by three to obtain a 3-point interface resolution (results in the rightmost images).

A first major observation that can be made is that the visual quality of the results is essentially unchanged by the modification of the thickening factor, which has been confirmed for all Reynolds numbers, even in the most demanding case of Fig. (26). In particular, the very strong interface diffusion observed for the coarser mesh resolution $r = 1/3$ is not present

Physics of Fluids ACCEPTED MANUSCRIPT

This is the author's peer reviewed, accepted manuscript. However, the online version of record will be different from this version once it has been copyedited and typeset.

PLEASE CITE THIS ARTICLE AS DOI: 10.1063/5.0048715

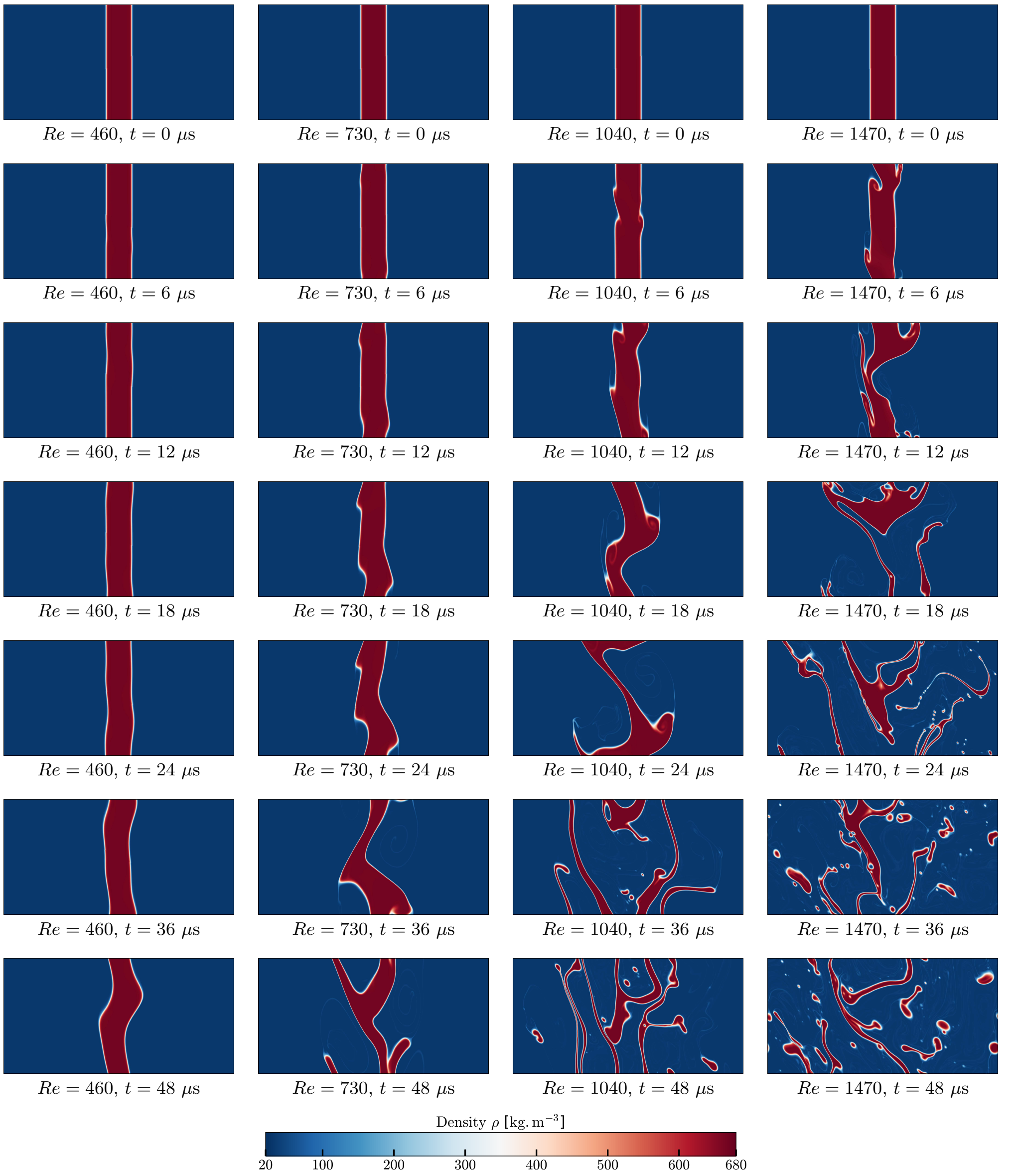

$Re = 460$, $t = 0$ μs
$Re = 730$, $t = 0$ μs
$Re = 1040$, $t = 0$ μs
$Re = 1470$, $t = 0$ μs
$Re = 460$, $t = 6$ μs
$Re = 730$, $t = 6$ μs
$Re = 1040$, $t = 6$ μs
$Re = 1470$, $t = 6$ μs
$Re = 460$, $t = 12$ μs
$Re = 730$, $t = 12$ μs
$Re = 1040$, $t = 12$ μs
$Re = 1470$, $t = 12$ μs
$Re = 460$, $t = 18$ μs
$Re = 730$, $t = 18$ μs
$Re = 1040$, $t = 18$ μs
$Re = 1470$, $t = 18$ μs
$Re = 460$, $t = 24$ μs
$Re = 730$, $t = 24$ μs
$Re = 1040$, $t = 24$ μs
$Re = 1470$, $t = 24$ μs
$Re = 460$, $t = 36$ μs
$Re = 730$, $t = 36$ μs
$Re = 1040$, $t = 36$ μs
$Re = 1470$, $t = 36$ μs
$Re = 460$, $t = 48$ μs
$Re = 730$, $t = 48$ μs
$Re = 1040$, $t = 48$ μs
$Re = 1470$, $t = 48$ μs

FIG. 23. Evolution in time of the density profiles for two-dimensional periodic Nitrogen liquid jets in their vapor. Three cases have been carried out with the reference spatial resolution for different Weber numbers, from left to right: *Re* = 460, *Re* = 730, *Re* = 1040 and *Re* = 1470

Physics of Fluids

ACCEPTED MANUSCRIPT

This is the author's peer reviewed, accepted manuscript. However, the online version of record will be different from this version once it has been copyedited and typeset.

PLEASE CITE THIS ARTICLE AS DOI: 10.1063/5.0048715

AIP Publishing

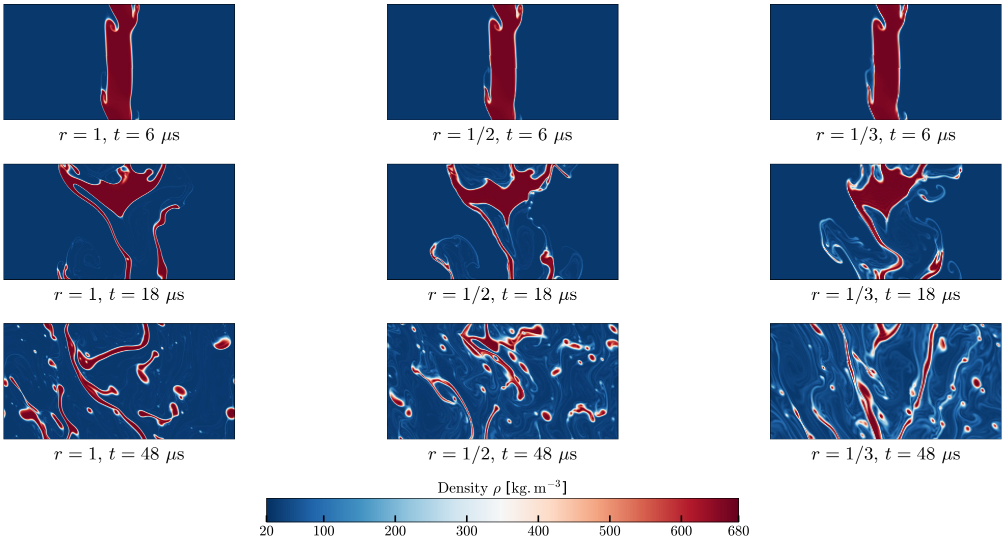
$r = 1,\ t = 6\ \mu$s
$r = 1/2,\ t = 6\ \mu$s
$r = 1/3,\ t = 6\ \mu$s
$r = 1,\ t = 18\ \mu$s
$r = 1/2,\ t = 18\ \mu$s
$r = 1/3,\ t = 18\ \mu$s
$r = 1,\ t = 48\ \mu$s
$r = 1/2,\ t = 48\ \mu$s
$r = 1/3,\ t = 48\ \mu$s

FIG. 24. Evolution in time of the density profiles for two-dimensional periodic Nitrogen liquid jets in their vapor. Three cases have been carried out for $Re = 1470$ $(We = 4150)$ with the reference thickening factor $\mathrm{F} = 1000$ and three different spatial resolutions (*left*: reference $r = 1$, *center*: coarse $r = 1/2$, *right*: very coarse $r = 1/3$).

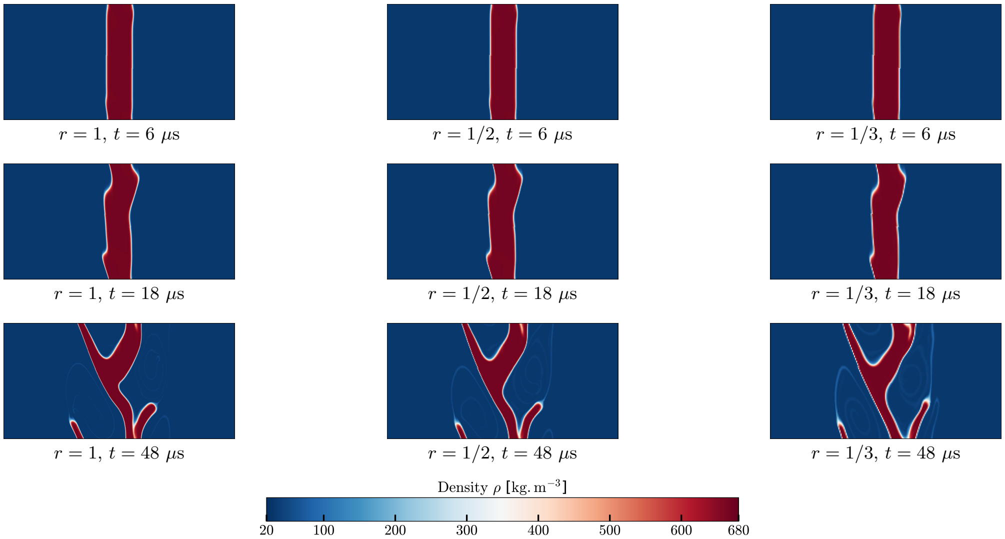
$r = 1,\ t = 6\ \mu$s
$r = 1/2,\ t = 6\ \mu$s
$r = 1/3,\ t = 6\ \mu$s
$r = 1,\ t = 18\ \mu$s
$r = 1/2,\ t = 18\ \mu$s
$r = 1/3,\ t = 18\ \mu$s
$r = 1,\ t = 48\ \mu$s
$r = 1/2,\ t = 48\ \mu$s
$r = 1/3,\ t = 48\ \mu$s

FIG. 25. Evolution in time of the density profiles for two-dimensional periodic Nitrogen liquid jets in their vapor. Three cases have been carried out at $Re = 730$ $(We = 1030)$ with the reference thickening factor $\mathrm{F} = 1000$ and three different spatial resolutions (*left*: reference $r = 1$, *center*: coarse $r = 1/2$, *right*: very coarse $r = 1/3$)

Physics of Fluids

ACCEPTED MANUSCRIPT

This is the author's peer reviewed, accepted manuscript. However, the online version of record will be different from this version once it has been copyedited and typeset.

PLEASE CITE THIS ARTICLE AS DOI: 10.1063/5.0048715

AIP Publishing

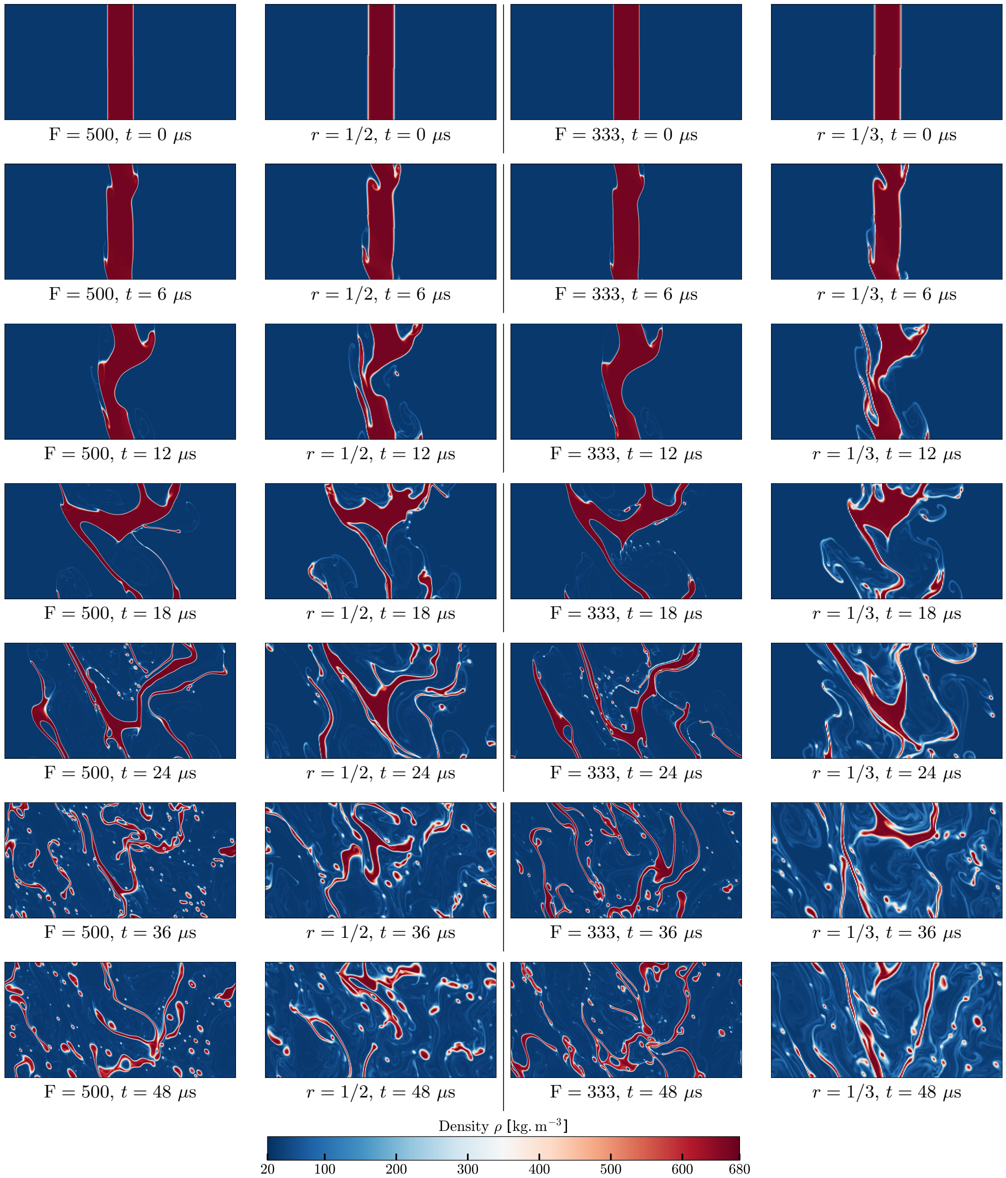

$\mathrm{F} = 500,\ t = 0\ \mu\mathrm{s}$ | $r = 1/2,\ t = 0\ \mu\mathrm{s}$ | $\mathrm{F} = 333,\ t = 0\ \mu\mathrm{s}$ | $r = 1/3,\ t = 0\ \mu\mathrm{s}$

$\mathrm{F} = 500,\ t = 6\ \mu\mathrm{s}$ | $r = 1/2,\ t = 6\ \mu\mathrm{s}$ | $\mathrm{F} = 333,\ t = 6\ \mu\mathrm{s}$ | $r = 1/3,\ t = 6\ \mu\mathrm{s}$

$\mathrm{F} = 500,\ t = 12\ \mu\mathrm{s}$ | $r = 1/2,\ t = 12\ \mu\mathrm{s}$ | $\mathrm{F} = 333,\ t = 12\ \mu\mathrm{s}$ | $r = 1/3,\ t = 12\ \mu\mathrm{s}$

$\mathrm{F} = 500,\ t = 18\ \mu\mathrm{s}$ | $r = 1/2,\ t = 18\ \mu\mathrm{s}$ | $\mathrm{F} = 333,\ t = 18\ \mu\mathrm{s}$ | $r = 1/3,\ t = 18\ \mu\mathrm{s}$

$\mathrm{F} = 500,\ t = 24\ \mu\mathrm{s}$ | $r = 1/2,\ t = 24\ \mu\mathrm{s}$ | $\mathrm{F} = 333,\ t = 24\ \mu\mathrm{s}$ | $r = 1/3,\ t = 24\ \mu\mathrm{s}$

$\mathrm{F} = 500,\ t = 36\ \mu\mathrm{s}$ | $r = 1/2,\ t = 36\ \mu\mathrm{s}$ | $\mathrm{F} = 333,\ t = 36\ \mu\mathrm{s}$ | $r = 1/3,\ t = 36\ \mu\mathrm{s}$

$\mathrm{F} = 500,\ t = 48\ \mu\mathrm{s}$ | $r = 1/2,\ t = 48\ \mu\mathrm{s}$ | $\mathrm{F} = 333,\ t = 48\ \mu\mathrm{s}$ | $r = 1/3,\ t = 48\ \mu\mathrm{s}$

FIG. 26. Evolution in time of the density profiles for two-dimensional periodic Nitrogen liquid jets in their vapor at $Re = 1470$ $(We = 4150)$. Two thickening factors and two mesh resolutions are used to get the same interface resolutions of five points (F = 500 / $r = 1/2$, *left images*) and three points (F = 333 / $r = 1/3$, *right images*)

Physics of Fluids ACCEPTED MANUSCRIPT
This is the author's peer reviewed, accepted manuscript. However, the online version of record will be different from this version once it has been copyedited and typeset.
PLEASE CITE THIS ARTICLE AS DOI: 10.1063/5.0048715
AIP Publishing

in its counterpart case with the thickening coefficient F = 333 despite the two approaches leading to the same interface resolution of about three points.

The second important observation that can be made is that although the thickening factor has a limited impact on the results visual quality, it has conversely a greater impact on the jet topology than that of the overall mesh resolution. Despite the strong interface diffusion, the results in Fig. (24) showcase a very visible similarity from one mesh to the other. Essentially, the results for the lower mesh resolutions are "simply diffused" versions of the results on the reference mesh. This similarity does not seem to apply anymore when the thickening factor is varying. Although the regime of the jet is properly retrieved for F = 666 and F = 333, the aspect of the jet, from one factor to the other, can been seen to strongly vary. This has been observed even for lower values of Reynolds number. More specifically, it seems that the lower the thickening factor is, i.e. the thinner the interface is, the smaller are the structures that are created during the atomization. This could be explained by the fact that the sizes of said structures apportion to the interface thickness meaning that these structures cannot appear spontaneously and/or cannot be sustained by the system thus leading to bigger droplets and thicker filaments for F = 1000. This hypothesis would however require further analysis to be assessed.

VI. CONCLUSIONS AND FUTURE WORK

In this study, we confirmed the predictive capabilities of the Second Gradient theory regarding the simulation of real gas flows under subcritical conditions where capillary effects lead to the presence of interfaces. It is possible to retrieve the saturation values for a given temperature, matching the ones otherwise obtained through classical equilibrium considerations as well as the interface width and the surface tension.

The TIM, a thermodynamically consistent thickening method, has been proposed and should allow to resolve interfaces on DNS (in the sense of turbulence) grids for a wide range of temperatures representative of cryogenic rocket engines at a relatively low computational cost. It preserves the interface dynamics through the conservation of its surface tension.

All the validation cases have been performed using the AVBP code solving the compressible Euler equations with real gas thermodynamics further cementing the applicability of both the Second Gradient theory and the TIM for more complex academic purposes and industrial configurations. The isothermal cases displayed the expected mechanical and thermodynamic behaviors, confirming the consistency of the model. The application to non isothermal cases also proved quite satisfactory : simulations of the collision of tree-dimensional droplets have provided results obtained experimentally with good accuracy and the TIM has been successful in simulating two-dimensional cases approaching that of an actual liquid jet injection. The results demonstrate the capability of the model to simulate such cases.

Some relevant questions still have to be treated and stand as primary concerns regarding our future work. The impact of the TIM on the dynamics of transitory phenomena should be further investigated as it could result on a modified characteristic response time of a deformed interface when trying to return to its equilibrium state. A slowed response of the interface could permit a longer persistence of unstable thermodynamic points which could, in part, be correlated to the excessive interface diffusion observed for ill-resolved liquid jets on the coarser meshes. This issue has not been met with a satisfactory explanation so far. Additionally, the interaction of the method with thermal conduction and viscosity must be addressed to resolve the full set of Navier-Stokes equations and get closer to practical configurations. Finally, the behavior of the method during the transition between subcritical and supercritical regimes should be looked at since the applicability of the method to such a thermodynamic change has been a driving concern for this study.

ACKNOWLEDGMENTS

The authors acknowledge funding from ANR through project ANR-14-CE22-0014 (SUBSUPERJET). This work was granted access to the HPC resources of CINES made available by GENCI (Grand Equipement National de Calcul Intensif) under the allocation A0042B06176. A part of this work was performed using HPC resources from the mésocentre computing center of Ecole CentraleSupélec and Ecole Normale Supérieur Paris-Saclay supported by CNRS and région Île-de-France. The simulations have been performed thanks to solver AVBP kindly provided by CERFACS. The authors would also like to thank D. Jamet, R. Saurel and M. Pelletier for fruitful discussions and insightful inputs.

DATA AVAILABILITY

The data that support the findings of this study are available from the corresponding author upon reasonable request.

[1] J. Bellan, "Supercritical (and subcritical) fluid behavior and modeling: drops, streams, shear and mixing layers, jets and sprays," Progress in energy and combustion science **26**, 329–366 (2000).
[2] R. N. Dahms and J. C. Oefelein, "Liquid jet breakup regimes at supercritical pressures," Combustion and Flame **162**, 3648–3657 (2015).
[3] J. C. Oefelein and V. Yang, "Modeling high-pressure mixing and combustion processes in liquid rocket engines," Journal of Propulsion and Power **14** (1998), https://doi.org/10.2514/2.5349.
[4] N. A. Okong'o and J. Bellan, "Direct numerical simulation of a transitional supercritical binary mixing layer: heptane and nitrogen," Journal of Fluid Mechanics **464**, 1–34 (2002).
[5] T. Schmitt, L. Selle, A. Ruiz, and B. Cuenot, "Large-eddy simulation of supercritical-pressure round jets," AIAA journal **48**, 2133–2144 (2010).
[6] V. Yang, "Modeling of supercritical vaporization, mixing, and combustion processes in liquid-fueled propulsion systems," Proceedings of the Combustion Institute **28**, 925–942 (2000).
[7] R. K.-C. Chan, "A generalized arbitrary lagrangian-eulerian method for incompressible flows with sharp interfaces," Journal of Computational Physics **17**, 311–331 (1975).

AIP Publishing Physics of Fluids ACCEPTED MANUSCRIPT
This is the author's peer reviewed, accepted manuscript. However, the online version of record will be different from this version once it has been copyedited and typeset.
PLEASE CITE THIS ARTICLE AS DOI: 10.1063/5.0048715

[8] C. Hirt, A. A. Amsden, and J. Cook, "An arbitrary lagrangian-eulerian computing method for all flow speeds," Journal of computational physics **14**, 227–253 (1974).

[9] G. Birkhoff, "Helmholtz and taylor instability," in *Proceedings of Symposia in Applied Mathematics*, Vol. 13 (1962) pp. 55–76.

[10] L. Rosenhead, "The formation of vortices from a surface of discontinuity," Proceedings of the Royal Society of London A: Mathematical, Physical and Engineering Sciences **134**, 170–192 (1931), http://rspa.royalsocietypublishing.org/content/134/823/170.full.pdf.

[11] G. Tryggvason, B. Bunner, A. Esmaeeli, D. Juric, N. Al-Rawahi, W. Tauber, J. Han, S. Nas, and Y.-J. Jan, "A front-tracking method for the computations of multiphase flow," Journal of Computational Physics **169**, 708 – 759 (2001).

[12] S. O. Unverdi and G. Tryggvason, "A front-tracking method for viscous, incompressible, multi-fluid flows," Journal of computational physics **100**, 25–37 (1992).

[13] F. H. Harlow, J. E. Welch, *et al.*, "Numerical calculation of time-dependent viscous incompressible flow of fluid with free surface," Physics of fluids **8**, 2182 (1965).

[14] J. Welch, F. Harlow, J. Shannon, and B. Daly, "The mac method - a computing technique for solving viscous, incompressible, transient fluid-flow problems involving free surfaces," Tech. Rep. (Los Alamos Scientific Lab., Univ. of California, N. Mex., 1965).

[15] S. Osher and R. P. Fedkiw, "Level set methods: an overview and some recent results," Journal of Computational physics **169**, 463–502 (2001).

[16] S. Osher and J. A. Sethian, "Fronts propagating with curvature-dependent speed: algorithms based on hamilton-jacobi formulations," Journal of computational physics **79**, 12–49 (1988).

[17] C. W. Hirt and B. D. Nichols, "Volume of fluid (vof) method for the dynamics of free boundaries," Journal of computational physics **39**, 201–225 (1981).

[18] O. Desjardins, V. Moureau, and H. Pitsch, "An accurate conservative level set/ghost fluid method for simulating turbulent atomization," Journal of Computational Physics **227**, 8395–8416 (2008).

[19] M. Owkes and O. Desjardins, "A discontinuous galerkin conservative level set scheme for interface capturing in multiphase flows," Journal of Computational Physics **249**, 275–302 (2013).

[20] N. Balcázar, O. Lehmkuhl, L. Jofre, J. Rigola, and A. Oliva, "A coupled volume-of-fluid/level-set method for simulation of two-phase flows on unstructured meshes," Computers & Fluids **124**, 12–29 (2016).

[21] D. Sun and W. Tao, "A coupled volume-of-fluid and level set (voset) method for computing incompressible two-phase flows," International Journal of Heat and Mass Transfer **53**, 645–655 (2010).

[22] M. Sussman and E. G. Puckett, "A coupled level set and volume-of-fluid method for computing 3d and axisymmetric incompressible two-phase flows," Journal of computational physics **162**, 301–337 (2000).

[23] Z. Wang, J. Yang, B. Koo, and F. Stern, "A coupled level set and volume-of-fluid method for sharp interface simulation of plunging breaking waves," International Journal of Multiphase Flow **35**, 227–246 (2009).

[24] J. U. Brackbill, D. B. Kothe, and C. Zemach, "A continuum method for modeling surface tension," J. Comput. Phys. **100**, 335–354 (1992).

[25] T. Ménard, S. Tanguy, and A. Berlemont, "Coupling level set/vof/ghost fluid methods: Validation and application to 3d simulation of the primary break-up of a liquid jet," International Journal of Multiphase Flow **33**, 510–524 (2007).

[26] X. Hu, B. Khoo, N. Adams, and F. Huang, "A conservative interface method for compressible flows," Journal of Computational Physics **219**, 553 – 578 (2006).

[27] H. Terashima and G. Tryggvason, "A front-tracking/ghost-fluid method for fluid interfaces in compressible flows," Journal of Computational Physics **228**, 4012 – 4037 (2009).

[28] G. Allaire, S. Clerc, and S. Kokh, "A five-equation model for the simulation of interfaces between compressible fluids," Journal of Computational Physics **181**, 577 – 616 (2002).

[29] M. Baer and J. Nunziato, "A two-phase mixture theory for the deflagration-to-detonation transition (ddt) in reactive granular materials," International Journal of Multiphase Flow **12**, 861 – 889 (1986).

[30] A. Kapila, R. Menikoff, J. Bdzil, S. Son, and D. S. Stewart, "Two-phase modeling of deflagration-to-detonation transition in granular materials: Reduced equations," Physics of fluids **13**, 3002–3024 (2001).

[31] J. Powers, D. Stewart, and H. Krier, "Theory of two-phase detonation—part ii: structure," Combustion and Flame **80**, 280–303 (1990).

[32] R. Saurel, A. Forestier, D. Veyret, and J.-C. Loraud, "A finite volume scheme for two-phase compressible flows," International journal for numerical methods in fluids **18**, 803–819 (1994).

[33] P. Gaillard, *Interfaces diffuses et flammes transcritiques LOX/H2*, Ph.D. thesis, Université Pierre et Marie Curie-Paris VI (2015).

[34] A. Murrone, *Modèles bi-fluides à six et sept équations pour les écoulements diphasiques à faible nombre de Mach*, Ph.D. thesis, Université de Provence-Aix-Marseille I (2003).

[35] G. Perigaud and R. Saurel, "A compressible flow model with capillary effects," Journal of Computational Physics **209**, 139 – 178 (2005).

[36] M. Pelletier, T. Schmitt, and S. Ducruix, "A multifluid taylor-galerkin methodology for the simulation of compressible multicomponent separate two-phase flows from subcritical to supercritical states," Computers & Fluids , 104588 (2020).

[37] S. M. Allen and J. W. Cahn, "A microscopic theory for antiphase boundary motion and its application to antiphase domain coarsening," Acta Metallurgica **27**, 1085–1095 (1979).

[38] J. W. Cahn and J. E. Hilliard, "Free energy of a nonuniform system. i. interfacial free energy," The Journal of Chemical Physics **28**, 258–267 (1958).

[39] J. D. van der Waals, "The thermodynamic theory of capillarity under the hypothesis of a continuous variation of density (Verhandel/Konink. Akad. Weten., 1893, vol. 1, English Translation)," Journal of Statistical Physics **20** (1893), https://doi.org/10.1007/BF01011514.

[40] D. J. Korteweg, "Sur la forme que prennent les équations du mouvement des fluides si l'on tient compte des forces capillaires causées par des variations de densité considérables mais continues et sur la théorie de la capillarité dans l'hypothese d'une variation continue de la densité," Archives Néerlandaises des Sciences exactes et naturelles **6**, 265 (1901).

[41] D. Joseph, "Fluid dynamics of two miscible liquids with diffusion and gradient stresses," European journal of mechanics. B, Fluids **9**, 565–596 (1990).

[42] D. Anderson and G. B. McFadden, "A diffuse-interface description of internal waves in a near-critical fluid," Physics of Fluids (1994-present) **9**, 1870–1879 (1997).

[43] R. Borcia and M. Bestehorn, "Phase-field simulations for drops and bubbles," Physical Review E **75**, 056309 (2007).

[44] D. N. Sibley, A. Nold, N. Savva, and S. Kalliadasis, "The contact line behaviour of solid-liquid-gas diffuse-interface models," Physics of Fluids **25**, 092111 (2013).

[45] J. Kou and S. Sun, "An adaptive finite element method for simulating surface tension with the gradient theory of fluid interfaces," Journal of Computational and Applied Mathematics **255**, 593–604 (2014).

[46] H. G. Lee and J. Kim, "An efficient numerical method for simulating multiphase flows using a diffuse interface model," Physica A: Statistical Mechanics and its Applications **423**, 33–50 (2015).

[47] Y. Li, D. Jeong, J. Shin, and J. Kim, "A conservative numerical method for the cahn-hilliard equation with dirichlet boundary conditions in complex domains," Computers & Mathematics with Applications **65**, 102–115 (2013).

[48] Y. Li, J.-I. Choi, and J. Kim, "A phase-field fluid modeling and computation with interfacial profile correction term," Communications in Nonlinear Science and Numerical Simulation **30**, 84 – 100 (2016).

[49] D. Anderson, G. B. McFadden, and A. Wheeler, "Diffuse-interface methods in fluid mechanics," Annual review of fluid mechanics **30**, 139–165 (1998).

[50] D. Jacqmin, "Calculation of two-phase navier-stokes flows using phase-field modeling," Journal of Computational Physics **155**, 96–127 (1999).

[51] V. Badalassi, H. Ceniceros, and S. Banerjee, "Computation of multiphase systems with phase field models," Journal of Computational Physics **190**, 371–397 (2003).

[52] P. Yue, J. J. Feng, C. Liu, and J. Shen, "A diffuse-interface method for simulating two-phase flows of complex fluids," Journal of Fluid Mechanics **515**, 293–317 (2004).

[53] C. Fouillet, *Généralisation à des mélanges binaires de la méthode du Second Gradient et application à la simulation numérique directe de l'ébulition nucléée*, Ph.D. thesis, Ecole Centrale Paris (2003).

[54] D. Jamet, *Etude des potentialités de la théorie du Second Gradient pour la simulation numérique directe des écoulements liquide-vapeur avec change-*

Physics of Fluids
ACCEPTED MANUSCRIPT
AIP Publishing
This is the author's peer reviewed, accepted manuscript. However, the online version of record will be different from this version once it has been copyedited and typeset.
PLEASE CITE THIS ARTICLE AS DOI: 10.1063/5.0048715

ment de phase, Ph.D. thesis, Ecole Centrale Paris (1998).

[55] J. D. van der Waals, *La continuité des états gazeux et liquides*, Ph.D. thesis (1894).

[56] D.-Y. Peng and D. B. Robinson, "A new two-constant equation of state," Industrial & Engineering Chemistry Fundamentals **15**, 59–64 (1976).

[57] G. Soave, "Equilibrium constants from a modified redlich-kwong equation of state," Chemical Engineering Science **27**, 1197 – 1203 (1972).

[58] V. Giovangigli, *Multicomponent flow modeling. Modeling and Simulation in Science, Engineering and Technology* (Birkhäuser Boston Inc., Boston, MA, 1999).

[59] J. W. Cahn, "Free energy of a nonuniform system. ii. thermodynamic basis," The Journal of Chemical Physics **30**, 1121–1124 (1959).

[60] J. W. Cahn and J. E. Hilliard, "Free energy of a nonuniform system. iii. nucleation in a two-component incompressible fluid," The Journal of Chemical Physics **31**, 688–699 (1959).

[61] P. Seppecher, *Etude d'une modelisation des zones capillaires fluides: interfaces et lignes de contact*, Ph.D. thesis, Ecole Nationale Superieure de Techniques Avancees (1987).

[62] P. Casal and H. Gouin, "Invariance properties of inviscid fluids of grade n," in *PDEs and Continuum Models of Phase Transitions: Proceedings of an NSF-CNRS Joint Seminar Held in Nice, France, January 18–22, 1988*, edited by M. Rascle, D. Serre, and M. Slemrod (Springer Berlin Heidelberg, Berlin, Heidelberg, 1989) pp. 85–98.

[63] Y. Rocard, *Thermodynamique II* (Masson et Ode, 1967).

[64] P. Casal and H. Gouin, "Relation entre l'équation de l'énergie et l'équation du mouvement en théorie de korteweg de la capillarité," Comptes-rendus des séances de l'Académie des sciences. Série 2, Mécanique-physique, chimie, sciences de l'univers, sciences de la terre **300**, 231–234 (1985).

[65] D. Jamet, O. Lebaigue, J.-M. Delhaye, and N. Coutris, "A numerical description of a liquid-vapor interface based on the second gradient theory," International Journal of Fluid Mechanics Research **22**, 1–14 (1995).

[66] V. Giovangigli, "Kinetic derivation of diffuse-interface fluid models," Physical Review E **102**, 012110 (2020).

[67] D. Jamet, "Diffuse interface models in fluid mechanics," GdR CNRS documentation, see pmc. polytechnique. fr/mp/GDR/docu/Jamet. pdf (2010).

[68] P. Gaillard, V. Giovangigli, and L. Matuszewski, "A diffuse interface lox/hydrogen transcritical flame model," Combustion Theory and Modelling **20**, 486–520 (2016).

[69] V. Carey, *Liquid Vapor Phase Change Phenomena: An Introduction to the Thermophysics of Vaporization and Condensation Processes in Heat Transfer Equipment, Second Edition* (Taylor & Francis, 2007).

[70] D. A. Edwards, H. Brenner, and D. T. Wasan, "{CHAPTER} 15 - a surface-excess theory of interfacial transport processes," in *Interfacial Transport Processes and Rheology*, edited by D. A. Edwards, H. Brenner, and D. T. Wasan (Butterworth-Heinemann, Boston, 1991) pp. 370 – 432.

[71] H. Margenau and G. M. Murphy, *The mathematics of physics and chemistry*, Vol. 1 (van Nostrand Princeton, NJ, 1943).

[72] H. Lin, Y.-Y. Duan, and Q. Min, "Gradient theory modeling of surface tension for pure fluids and binary mixtures," Fluid Phase Equilibria **254**, 75 – 90 (2007).

[73] R. F. Curl and K. Pitzer, "Volumetric and thermodynamic properties of fluids - enthalpy, free energy, and entropy," Industrial & Engineering Chemistry **50**, 265–274 (1958), http://dx.doi.org/10.1021/ie50578a047.

[74] B. McCoy, L. Scriven, and H. Davis, "Comparison of molecular models of the liquid–vapor interface," The Journal of Chemical Physics **75**, 4719–4726 (1981).

[75] A. Ruiz, *Unsteady Numerical Simulations of Transcritical Turbulent Combustion in Liquid Rocket Engines*, Ph.D. thesis, Toulouse, INPT (2012).

[76] D. Jamet, O. Lebaigue, N. Coutris, and J. Delhaye, "The second gradient method for the direct numerical simulation of liquid-vapor flows with phase change," Journal of Computational Physics **169**, 624–651 (2001).

[77] T. J. Poinsot and S. K. Lele, "Boundary conditions for direct simulations of compressible viscous flows," Journal of Computational Physics **101**, 104–129 (1992).

[78] J. Mathew, R. Lechner, H. Foysi, J. Sesterhenn, and R. Friedrich, "An explicit filtering method for large eddy simulation of compressible flows," Physics of fluids **15**, 2279–2289 (2003).

[79] D. Fyfe, E. Oran, and M. Fritts, "Surface tension and viscosity with lagrangian hydrodynamics on a triangular mesh," Journal of Computational Physics **76**, 349 – 384 (1988).

[80] A. Prosperetti, "Motion of two superposed viscous fluids," The Physics of Fluids **24**, 1217–1223 (1981).

[81] T. H. Chung, M. Ajlan, L. L. Lee, and K. E. Starling, "Generalized multiparameter correlation for nonpolar and polar fluid transport properties," Industrial & engineering chemistry research **27**, 671–679 (1988).

[82] J. Adam, N. Lindblad, and C. Hendricks, "The collision, coalescence, and disruption of water droplets," Journal of Applied Physics **39**, 5173–5180 (1968).

[83] R. W. Park, *Behavior of water drops colliding in humid nitrogen.*, Ph.D. thesis (1970).

[84] A. Podvysotsky and A. Shraiber, "Coalescence and break-up of drops in two-phase flows," International journal of multiphase flow **10**, 195–209 (1984).

[85] N. Ashgriz and J. Poo, "Coalescence and separation in binary collisions of liquid drops," Journal of Fluid Mechanics **221**, 183–204 (1990).

[86] Y. Jiang, A. Umemura, and C. K. Law, "An experimental investigation on the collision behaviour of hydrocarbon droplets," Journal of Fluid Mechanics **234**, 171–190 (1992).

[87] S. Tanguy and A. Berlemont, "Application of a level set method for simulation of droplet collisions," International journal of multiphase flow **31**, 1015–1035 (2005).

[88] Y. Pan and K. Suga, "Numerical simulation of binary liquid droplet collision," Physics of Fluids **17**, 082105 (2005).

[89] M. Rieber and A. Frohn, "Navier-stokes simulation of droplet collision dynamics," in *Proc. 7th Int. Symp. On Comp. Fluid Dynamics,(ed. by Zhuang, FG) Beijing, China* (1997) pp. 520–525.

[90] S. Shimasaki and S. Taniguchi, "Formation of uniformly sized metal droplets from a capillary jet by electromagnetic force," Applied Mathematical Modelling **35**, 1571–1580 (2011).

[91] S. Aland, "Time integration for diffuse interface models for two-phase flow," Journal of Computational Physics **262**, 58–71 (2014).

[92] H. A. Amiri and A. Hamouda, "Evaluation of level set and phase field methods in modeling two phase flow with viscosity contrast through dual-permeability porous medium," International Journal of Multiphase Flow **52**, 22–34 (2013).

Physics of Fluids ACCEPTED MANUSCRIPT
AIP Publishing
This is the author's peer reviewed, accepted manuscript. However, the online version of record will be different from this version once it has been copyedited and typeset.
PLEASE CITE THIS ARTICLE AS DOI: 10.1063/5.0048715

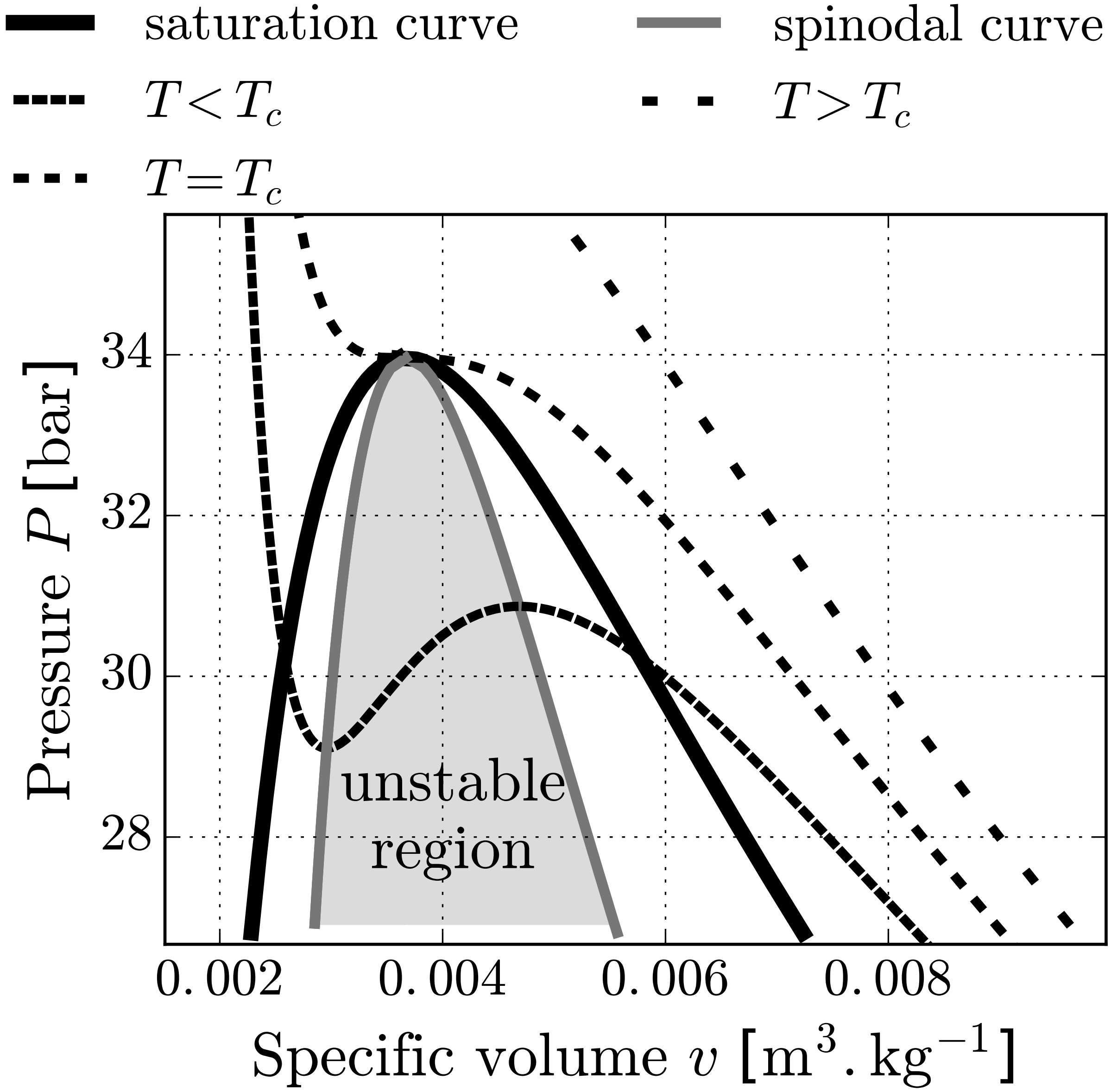

ACCEPTED MANUSCRIPT

Physics of Fluids

This is the author's peer reviewed, accepted manuscript. However, the online version of record will be different from this version once it has been copyedited and typeset.

PLEASE CITE THIS ARTICLE AS DOI: 10.1063/5.0048715

AIP Publishing

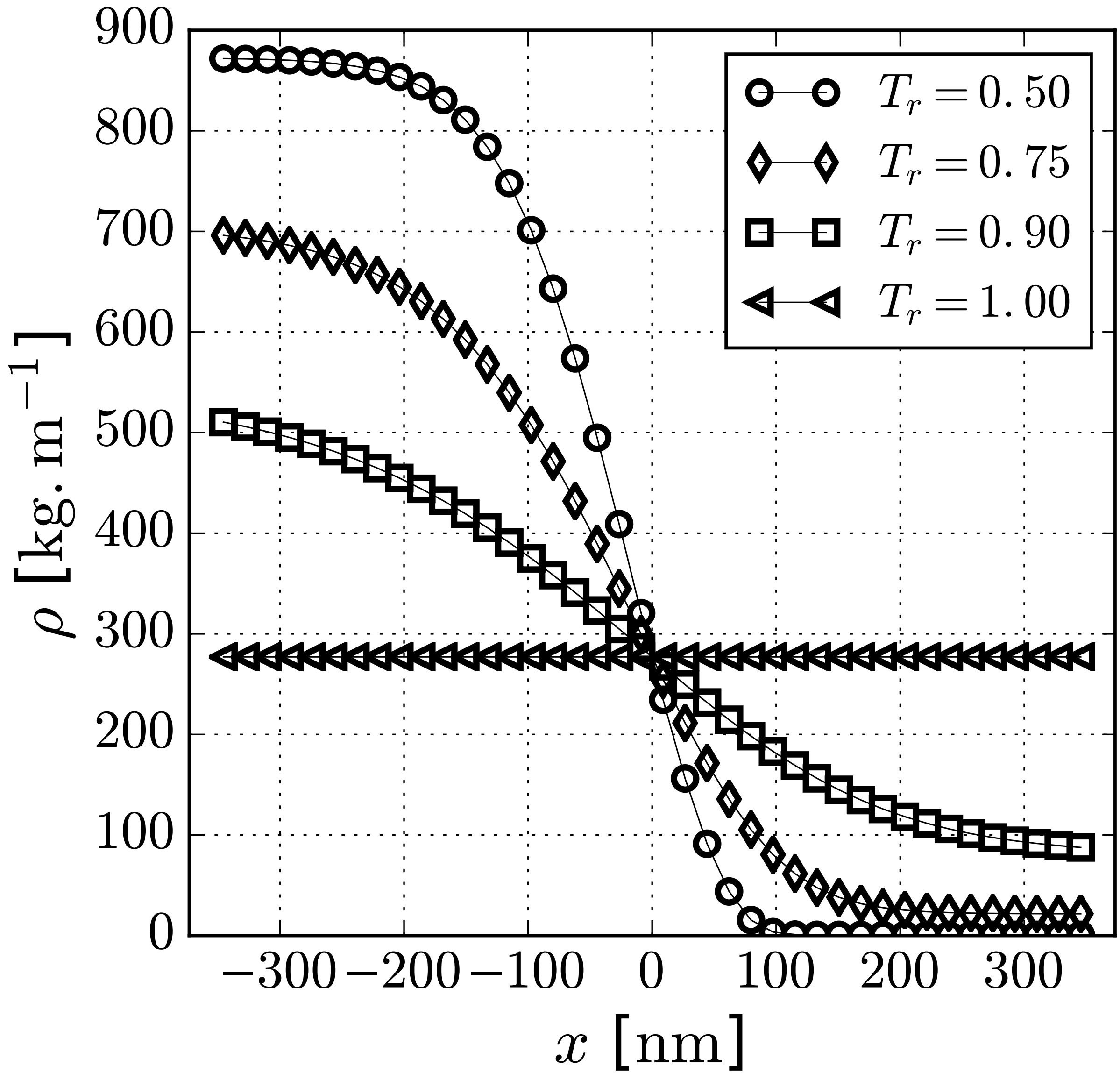

Physics of Fluids
ACCEPTED MANUSCRIPT
This is the author's peer reviewed, accepted manuscript. However, the online version of record will be different from this version once it has been copyedited and typeset.
PLEASE CITE THIS ARTICLE AS DOI: 10.1063/5.0048715

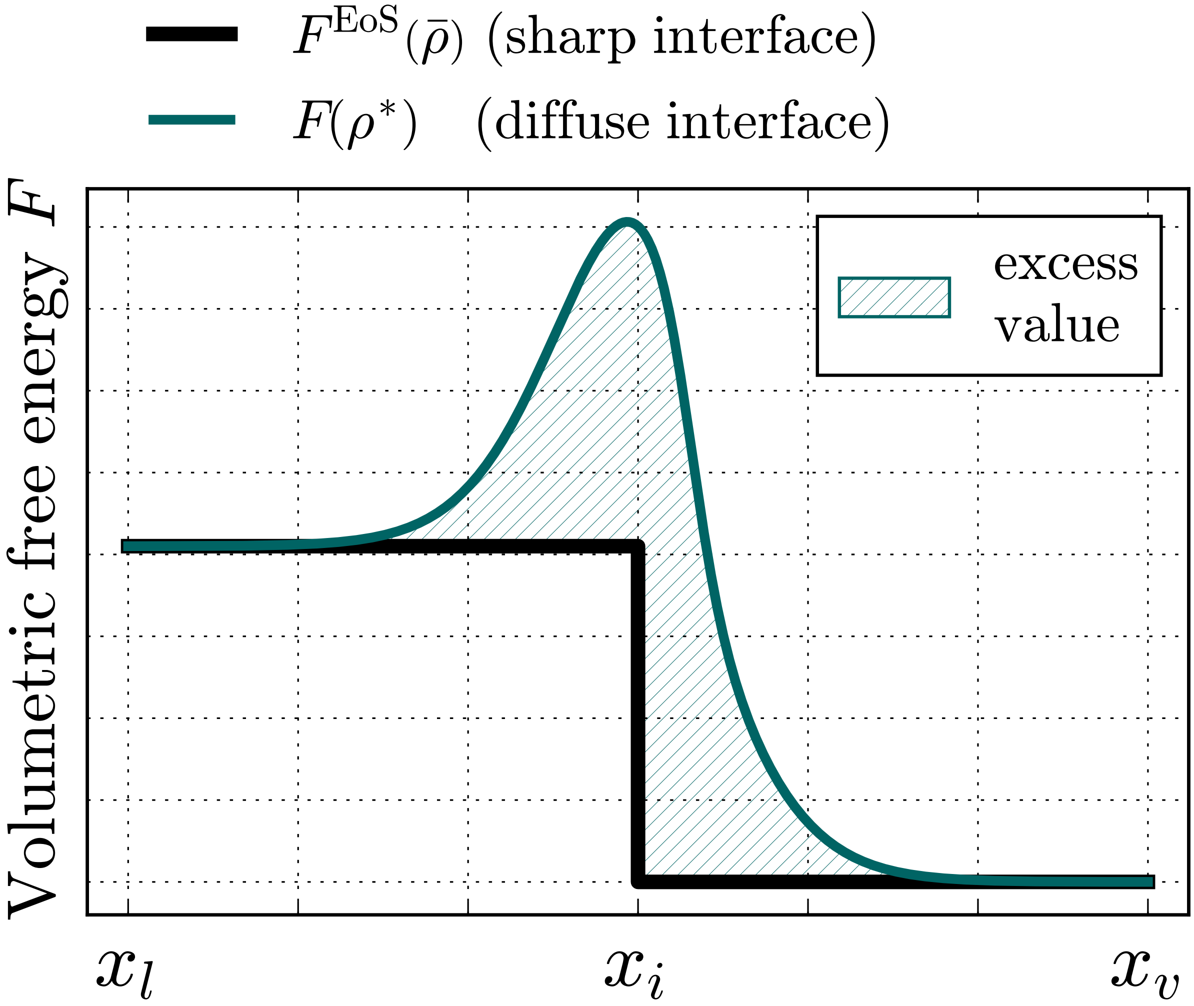

Physics of Fluids
ACCEPTED MANUSCRIPT
This is the author's peer reviewed, accepted manuscript. However, the online version of record will be different from this version once it has been copyedited and typeset.
PLEASE CITE THIS ARTICLE AS DOI: 10.1063/5.0048715

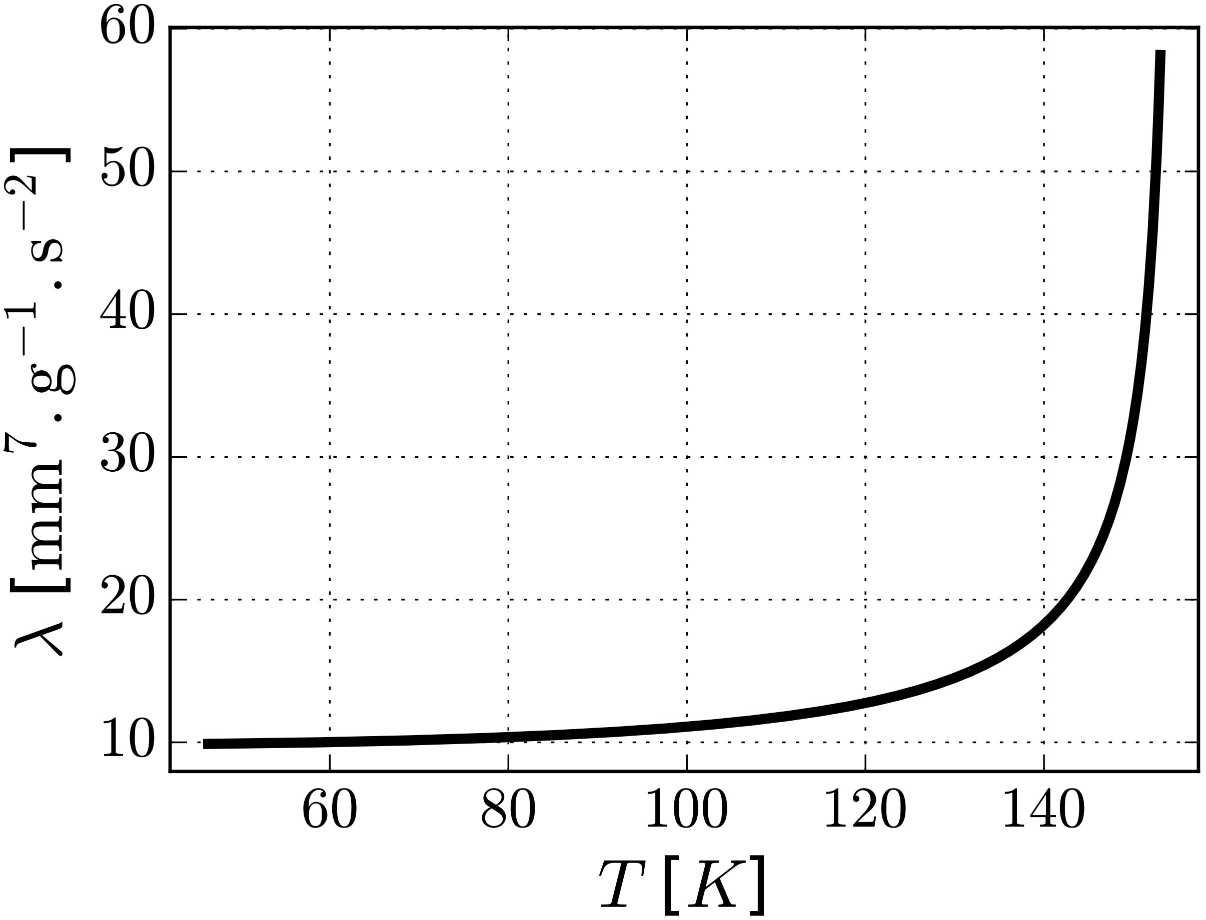

ACCEPTED MANUSCRIPT

Physics of Fluids

This is the author's peer reviewed, accepted manuscript. However, the online version of record will be different from this version once it has been copyedited and typeset.

PLEASE CITE THIS ARTICLE AS DOI: 10.1063/5.0048715

AIP Publishing

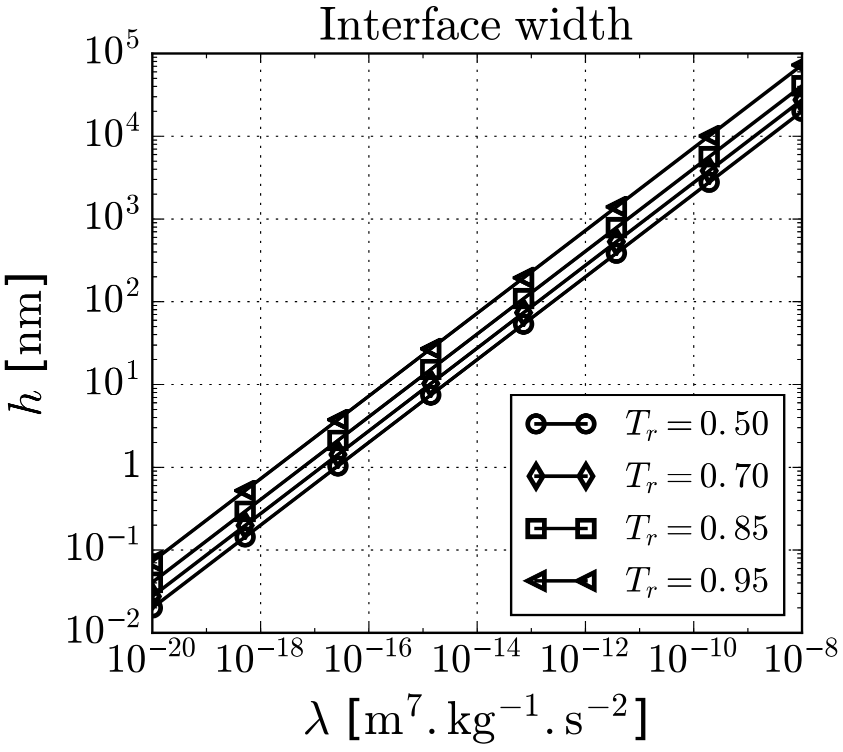

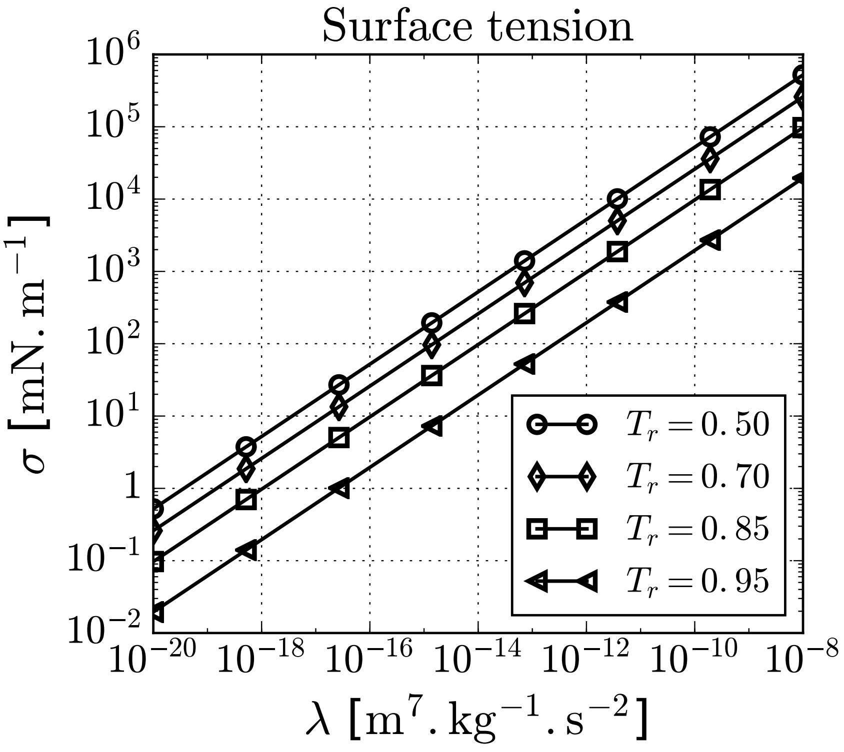

AIP Publishing

Physics of Fluids

ACCEPTED MANUSCRIPT

This is the author's peer reviewed, accepted manuscript. However, the online version of record will be different from this version once it has been copyedited and typeset.

PLEASE CITE THIS ARTICLE AS DOI: 10.1063/5.0048715

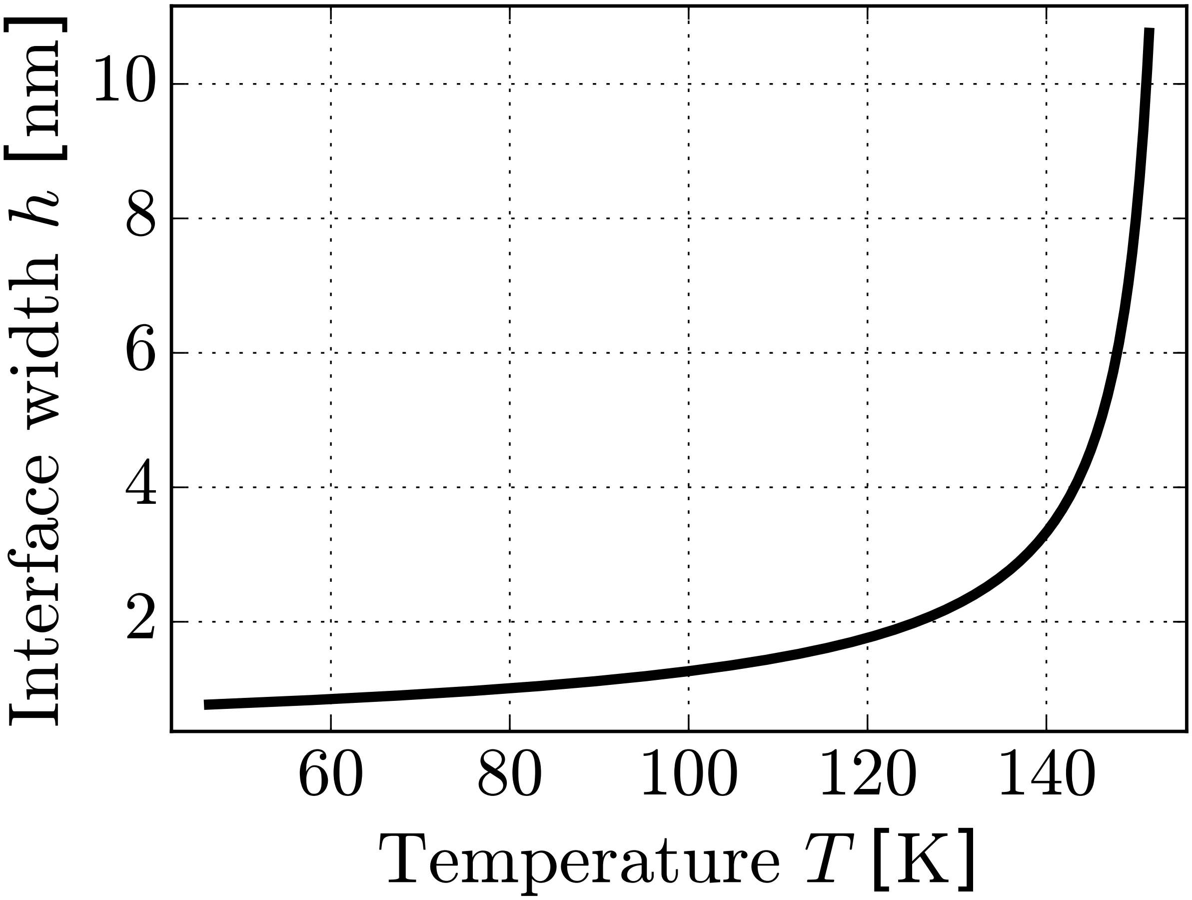

Physics of Fluids

ACCEPTED MANUSCRIPT

This is the author's peer reviewed, accepted manuscript. However, the online version of record will be different from this version once it has been copyedited and typeset.

PLEASE CITE THIS ARTICLE AS DOI: 10.1063/5.0048715

AIP Publishing

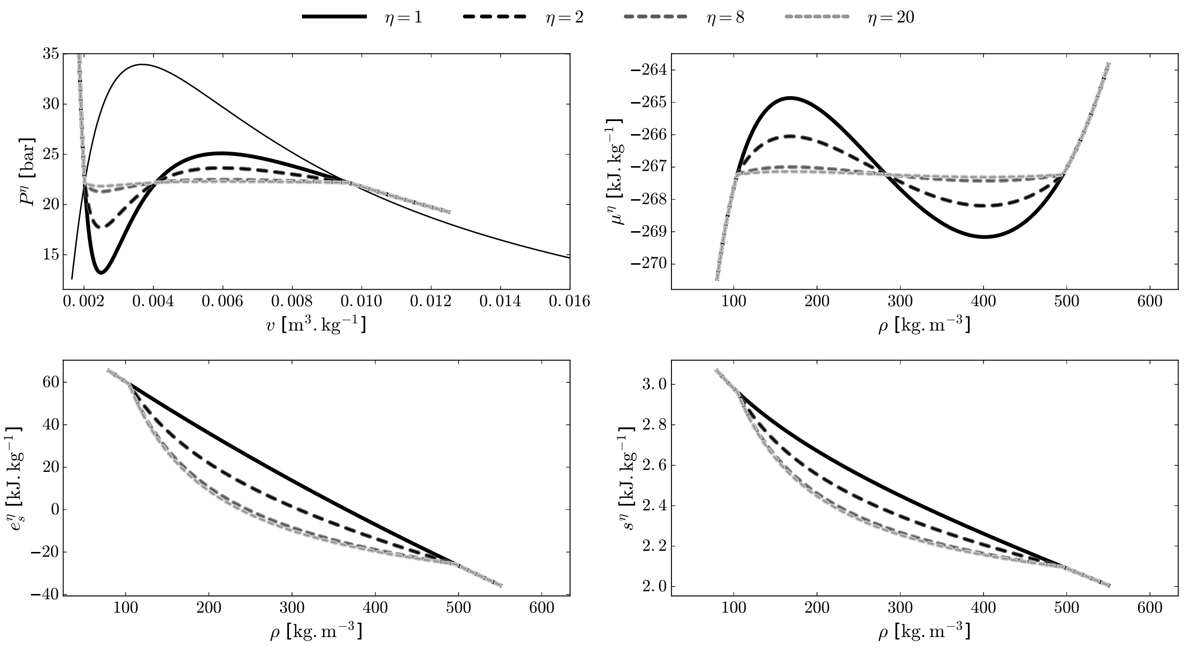

ACCEPTED MANUSCRIPT
Physics of Fluids
This is the author's peer reviewed, accepted manuscript. However, the online version of record will be different from this version once it has been copyedited and typeset.
PLEASE CITE THIS ARTICLE AS DOI: 10.1063/5.0048715
AIP Publishing

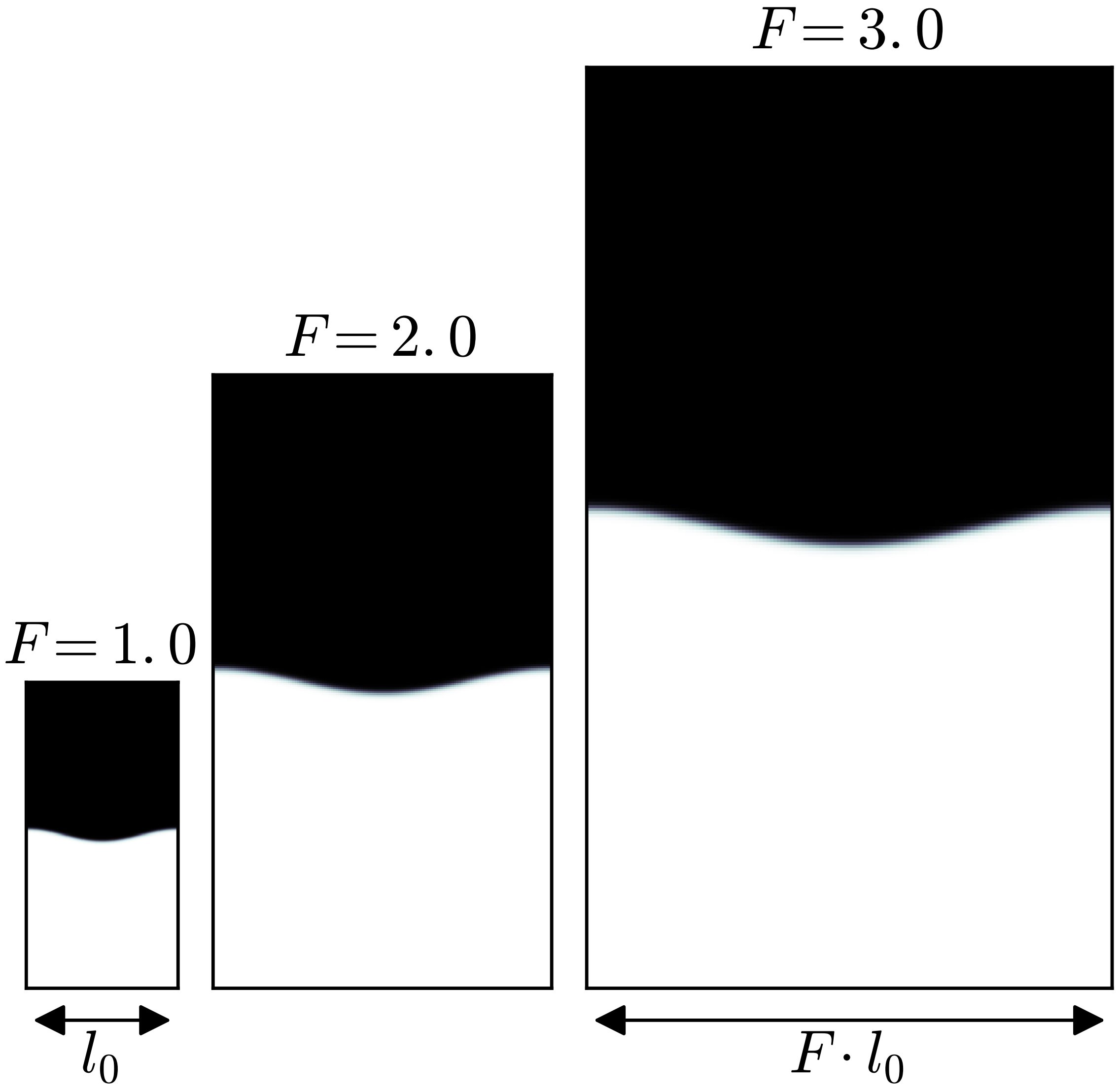

Physics of Fluids ACCEPTED MANUSCRIPT

This is the author's peer reviewed, accepted manuscript. However, the online version of record will be different from this version once it has been copyedited and typeset.
PLEASE CITE THIS ARTICLE AS DOI: 10.1063/5.0048715

oscillation has been extracted by monitoring the time evolution of the density at the center of the domain, with an example given for F = 50 in Fig. (13).

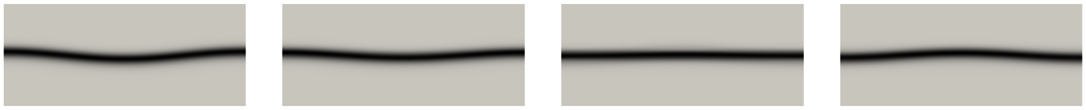

(a) $t = 0$ (b) $t = \tau/8$ (c) $t = 2\tau/8$ (d) $t = 3\tau/8$

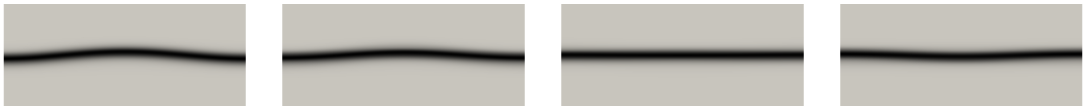

(e) $t = 4\tau/8$ (f) $t = 5\tau/8$ (g) $t = 6\tau/8$ (h) $t = 7\tau/8$

Figure 12: Zoom on the normalized density gradient profiles at different instants for the oscillation of an initially harmonically perturbed plane nitrogen N_2 interface with $T_{init} = 119.88$ K, $\lambda_0 = 1.0 \cdot 10^{-16}$ m^7.kg^{-1}.s^{-2} and F = 50

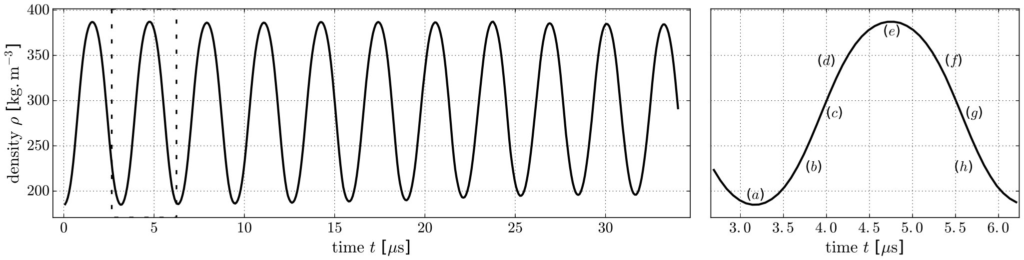

Figure 13: Time evolution of the density at the center of the domain for the oscillation of an initially harmonically perturbed plane nitrogen N_2 interface with $T_{init} = 119.88$ K, $\lambda_0 = 1.0 \cdot 10^{-16}$ m^7.kg^{-1}.s^{-2} and F = 50

From Fyfe et al. (1988) one gets that the expected frequency of the oscillations ω obeys Eq. (48) where ρ_u (resp. ρ_d) and h_u (resp. h_d) are the density and width of the upper (res. lower) fluid, σ the surface tension of the interface, g the gravity acceleration and k the wavenumber of the deformation. Noticeably, it does not depend on the amplitude of the initial deformation.

$$\omega^2 = \frac{(\rho_\mathrm{d} - \rho_\mathrm{u})\, gk + \sigma k^3}{\rho_\mathrm{d} \coth kh_\mathrm{d} + \rho_\mathrm{u} \coth kh_\mathrm{u}} \tag{48}$$

In our configuration, no gravity is considered, the upper and lower densities are the saturation densities ρ_v and ρ_l, only one period of a sine is used for the deformation therefore $k = 2\pi/l$ where l is the domain width i.e. the length of the interface when no perturbation is applied and the upper and lower widths h_u, h_d have been chosen

ACCEPTED MANUSCRIPT

Physics of Fluids

This is the author's peer reviewed, accepted manuscript. However, the online version of record will be different from this version once it has been copyedited and typeset.

PLEASE CITE THIS ARTICLE AS DOI: 10.1063/5.0048715

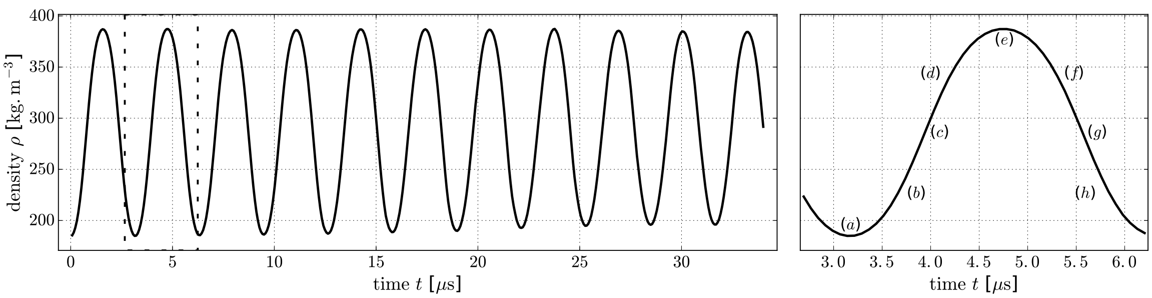

ACCEPTED MANUSCRIPT
Physics of Fluids
AIP Publishing
This is the author's peer reviewed, accepted manuscript. However, the online version of record will be different from this version once it has been copyedited and typeset.
PLEASE CITE THIS ARTICLE AS DOI: 10.1063/5.0048715

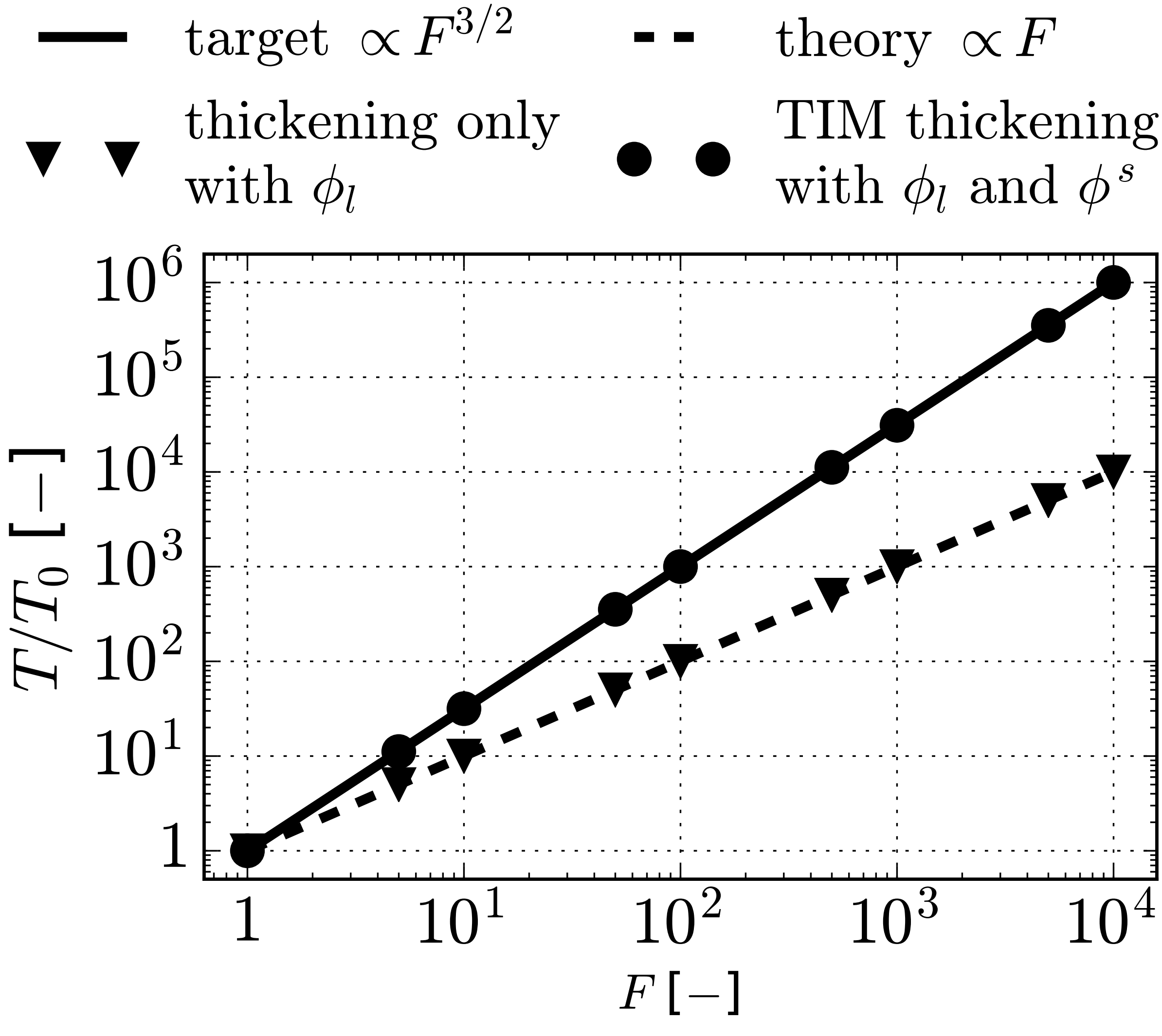

ACCEPTED MANUSCRIPT

Physics of Fluids

AIP Publishing

This is the author's peer reviewed, accepted manuscript. However, the online version of record will be different from this version once it has been copyedited and typeset.

PLEASE CITE THIS ARTICLE AS DOI: 10.1063/5.0048715

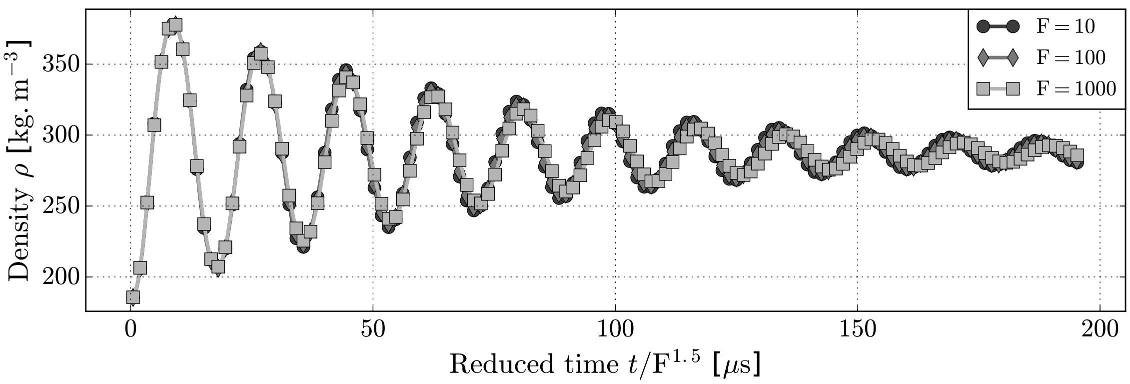

ACCEPTED MANUSCRIPT
Physics of Fluids
AIP Publishing
This is the author's peer reviewed, accepted manuscript. However, the online version of record will be different from this version once it has been copyedited and typeset.
PLEASE CITE THIS ARTICLE AS DOI: 10.1063/5.0048715

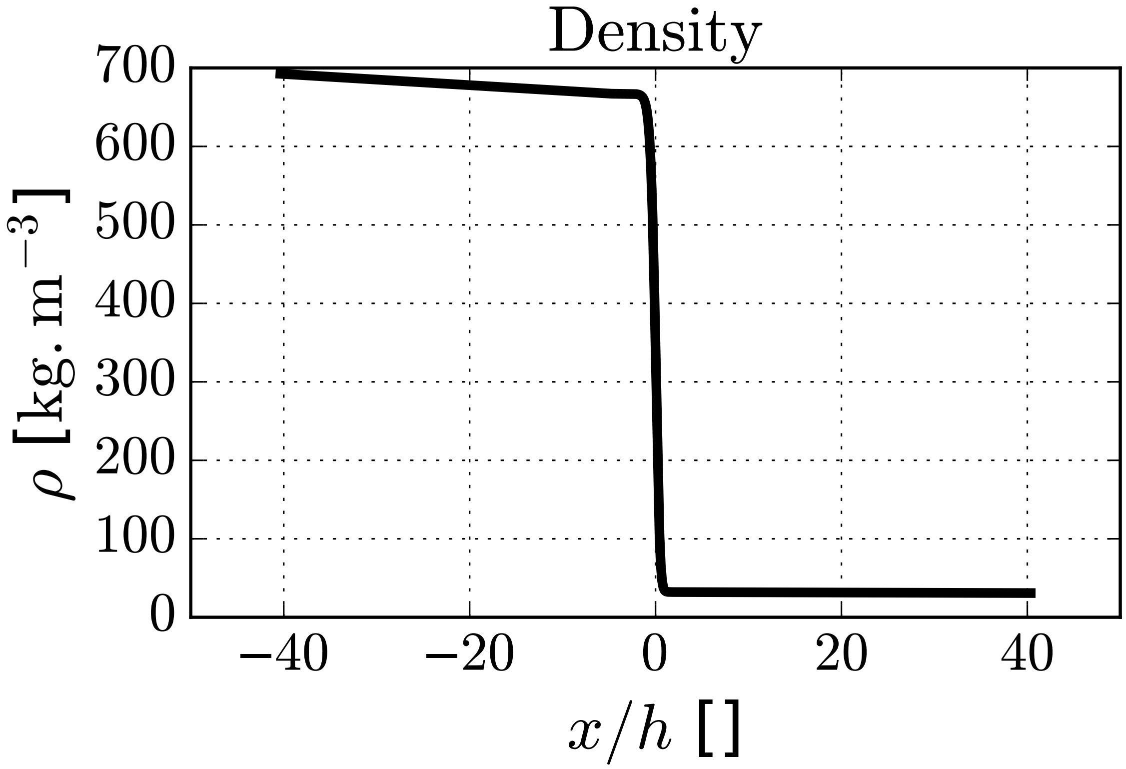

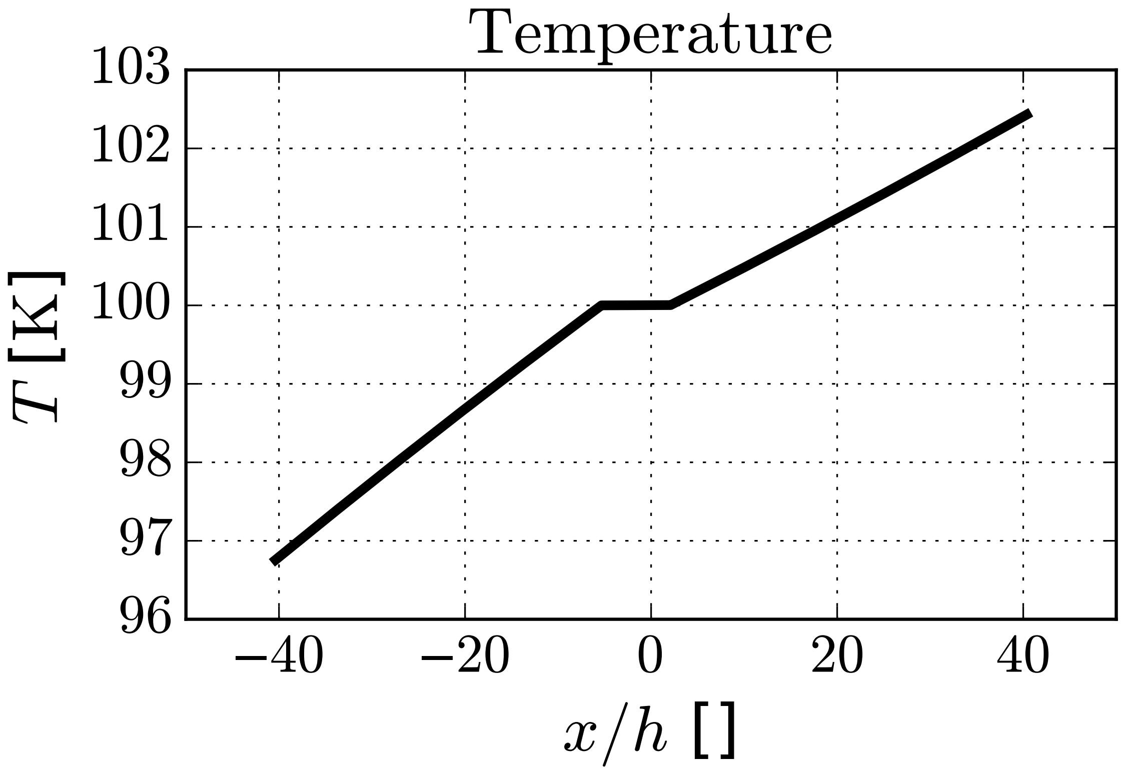

ACCEPTED MANUSCRIPT

Physics of Fluids

This is the author's peer reviewed, accepted manuscript. However, the online version of record will be different from this version once it has been copyedited and typeset.

PLEASE CITE THIS ARTICLE AS DOI: 10.1063/5.0048715

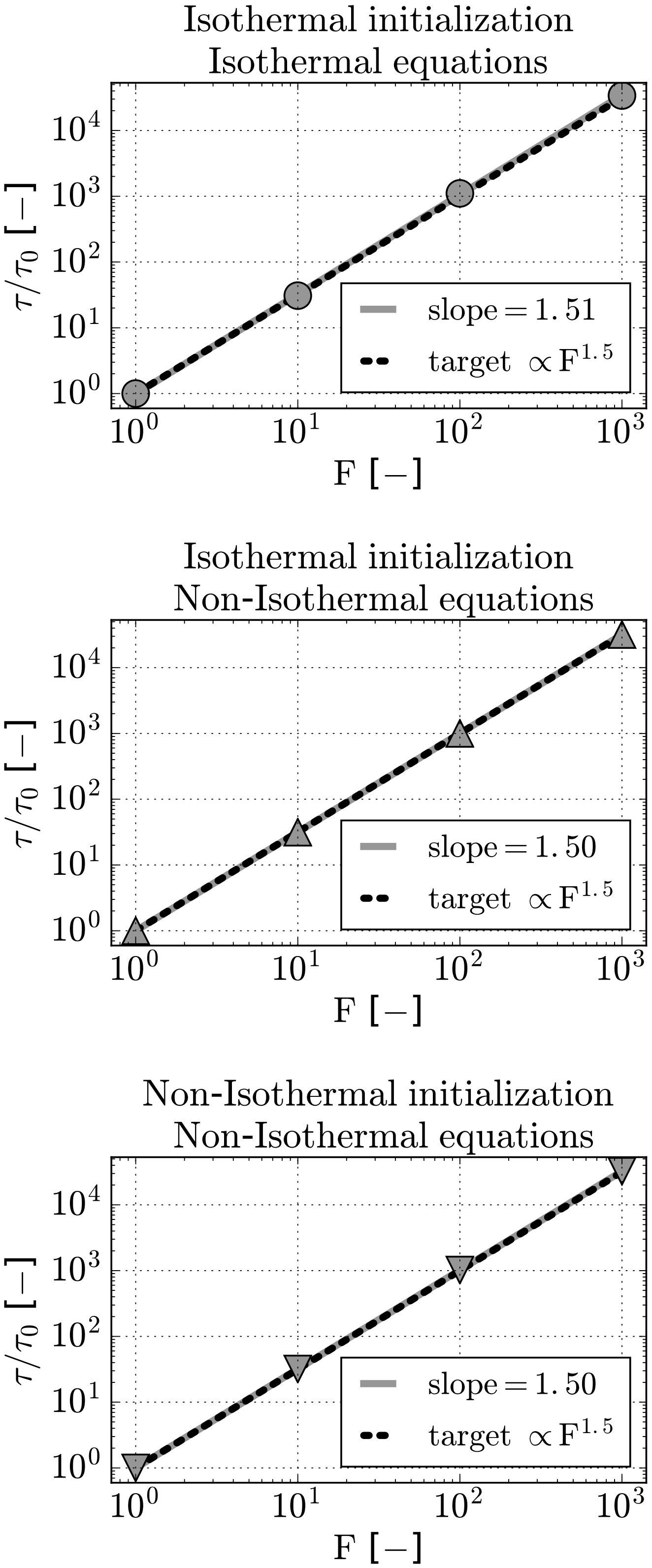

ACCEPTED MANUSCRIPT

Physics of Fluids

This is the author's peer reviewed, accepted manuscript. However, the online version of record will be different from this version once it has been copyedited and typeset.

PLEASE CITE THIS ARTICLE AS DOI: 10.1063/5.0048715

AIP Publishing

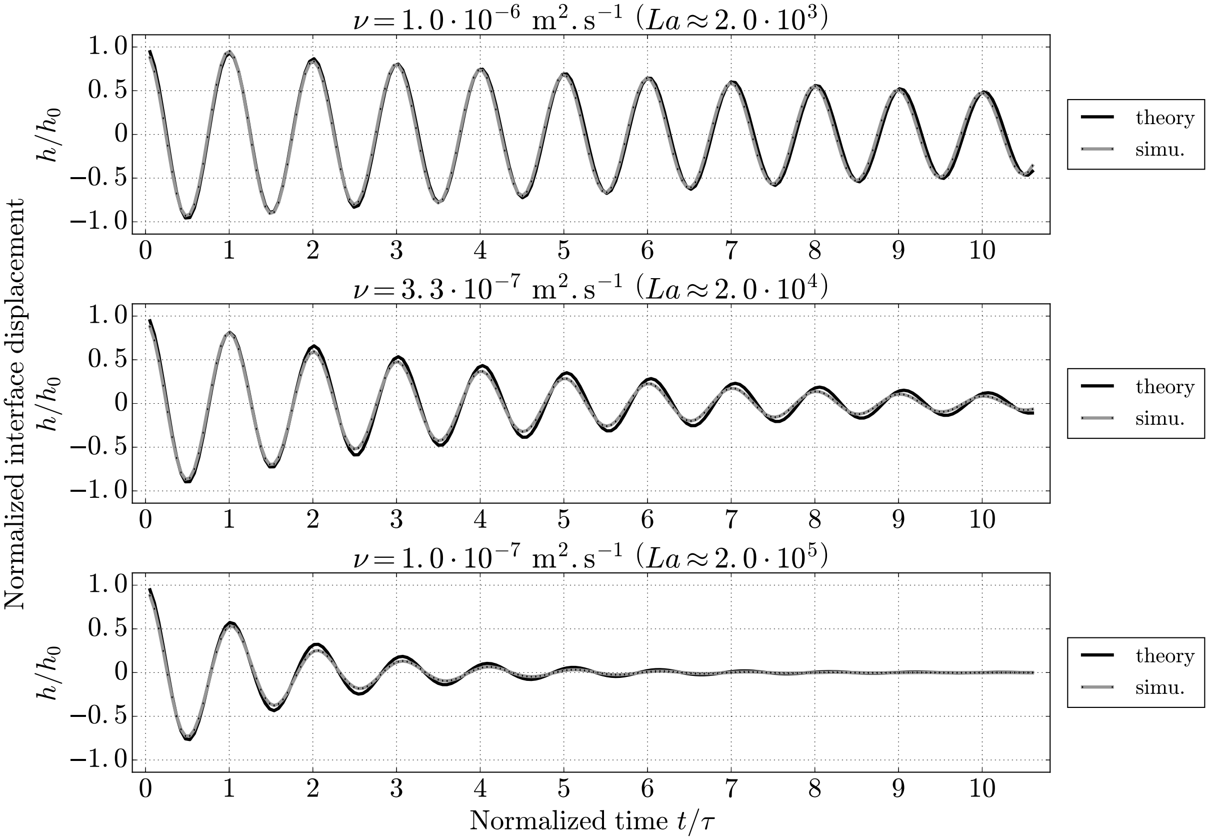

Physics of Fluids

ACCEPTED MANUSCRIPT

This is the author's peer reviewed, accepted manuscript. However, the online version of record will be different from this version once it has been copyedited and typeset.

PLEASE CITE THIS ARTICLE AS DOI: 10.1063/5.0048715

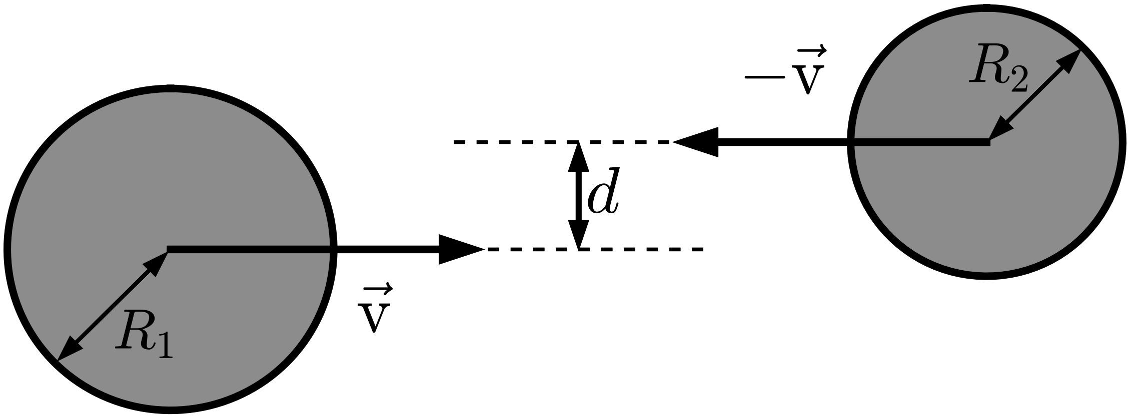

ACCEPTED MANUSCRIPT

Physics of Fluids

AIP Publishing

This is the author's peer reviewed, accepted manuscript. However, the online version of record will be different from this version once it has been copyedited and typeset.

PLEASE CITE THIS ARTICLE AS DOI: 10.1063/5.0048715

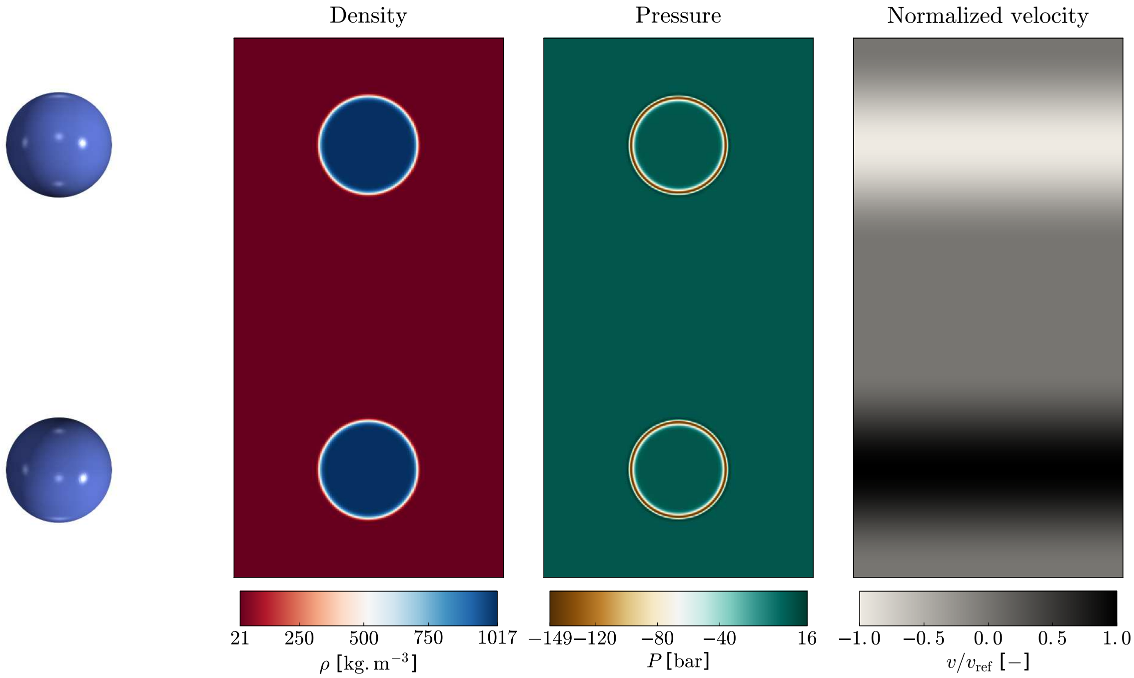

ACCEPTED MANUSCRIPT

Physics of Fluids

This is the author's peer reviewed, accepted manuscript. However, the online version of record will be different from this version once it has been copyedited and typeset.

PLEASE CITE THIS ARTICLE AS DOI: 10.1063/5.0048715

AIP Publishing

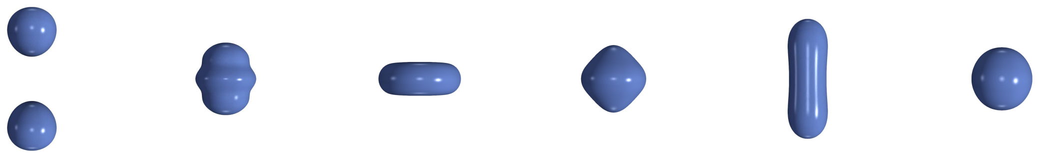

Figure 22: Head-on collision of liquid droplets, simulation results with oxygen droplets at $We = 20$ ($Re_l = 556$) using the TIM

Weber number $We = 40$ (v = 2.03 m.s^{-1}). For the most part, the scenario of the collision is well retrieved in the simulation. The persistence of a small satellite droplet between the post-collision departing droplets, which does not appear in the experiments, can however be noticed.

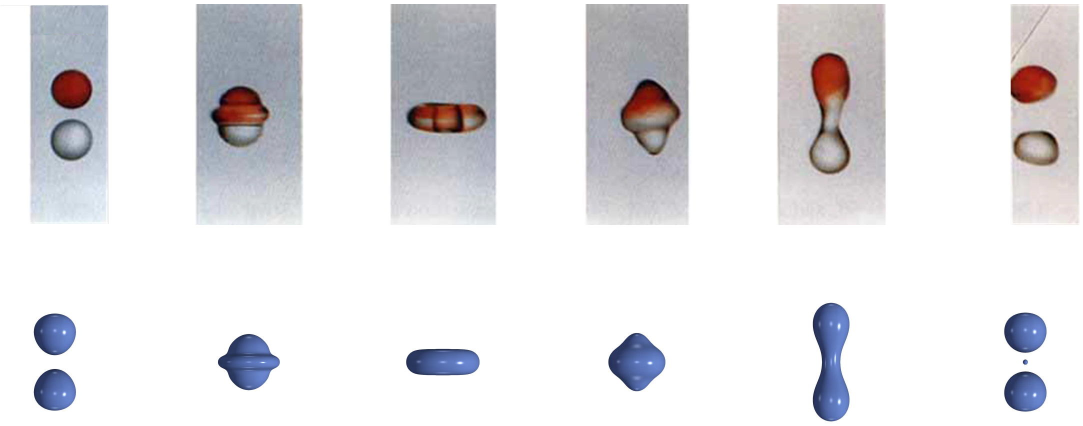

Figure 23: Head-on collision of liquid droplets, comparison between experiments with water droplets at $We = 23$ from Ashgriz & Poo (1990) and simulation results with oxygen droplets at $We = 40$ ($Re_l = 790$) using the TIM

The question of obtaining reflexive separation without satellite droplets does not seem to be directly addressed in the literature. Such outcomes have been observed experimentally for water in air in Ashgriz & Poo (1990) and numerically, still for water, using either LS methods in Tanguy & Berlemont (2005); Pan & Suga (2005) or VOF methods in Rieber & Frohn (1997). Most other results involving different fluids, either experimentally or numerically, showcase reflexive separation with creation of at least a very small droplet in the center. In Ashgriz & Poo (1990), the authors observed the same satellite-free reflexive separation over the range $19 \leqslant We \leqslant 23$.

To obtain a clearly defined single satellite droplet, reminiscent of the head-on collision at $We = 40$ from Ashgriz & Poo (1990), a third simulation at $We = 80$ (v = 2.87 m.s^{-1}) has been performed, the comparative results are

ACCEPTED MANUSCRIPT
Physics of Fluids
This is the author's peer reviewed, accepted manuscript. However, the online version of record will be different from this version once it has been copyedited and typeset.
PLEASE CITE THIS ARTICLE AS DOI: 10.1063/5.0048715
AIP Publishing

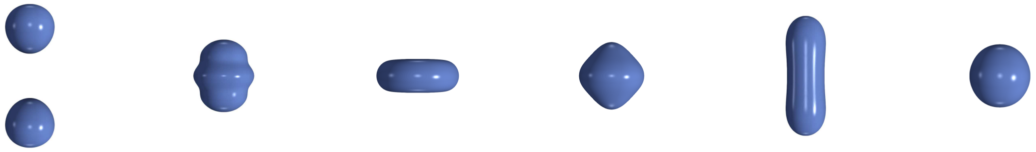

Figure 22: Head-on collision of liquid droplets, simulation results with oxygen droplets at $We = 20$ ($Re_l = 556$) using the TIM

Weber number $We = 40$ (v = 2.03 m.s^{-1}). For the most part, the scenario of the collision is well retrieved in the simulation. The persistence of a small satellite droplet between the post-collision departing droplets, which does not appear in the experiments, can however be noticed.

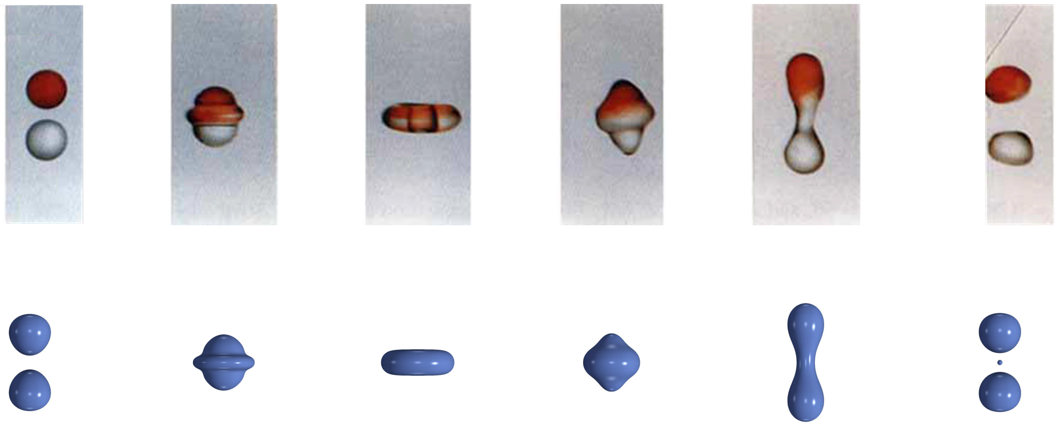

Figure 23: Head-on collision of liquid droplets, comparison between experiments with water droplets at $We = 23$ from Ashgriz & Poo (1990) and simulation results with oxygen droplets at $We = 40$ ($Re_l = 790$) using the TIM

The question of obtaining reflexive separation without satellite droplets does not seem to be directly addressed in the literature. Such outcomes have been observed experimentally for water in air in Ashgriz & Poo (1990) and numerically, still for water, using either LS methods in Tanguy & Berlemont (2005); Pan & Suga (2005) or VOF methods in Rieber & Frohn (1997). Most other results involving different fluids, either experimentally or numerically, showcase reflexive separation with creation of at least a very small droplet in the center. In Ashgriz & Poo (1990), the authors observed the same satellite-free reflexive separation over the range $19 \leqslant We \leqslant 23$.

To obtain a clearly defined single satellite droplet, reminiscent of the head-on collision at $We = 40$ from Ashgriz & Poo (1990), a third simulation at $We = 80$ (v = 2.87 m.s^{-1}) has been performed, the comparative results are

ACCEPTED MANUSCRIPT

Physics of Fluids

This is the author's peer reviewed, accepted manuscript. However, the online version of record will be different from this version once it has been copyedited and typeset.

PLEASE CITE THIS ARTICLE AS DOI: 10.1063/5.0048715

AIP Publishing

shown in Fig. (24).

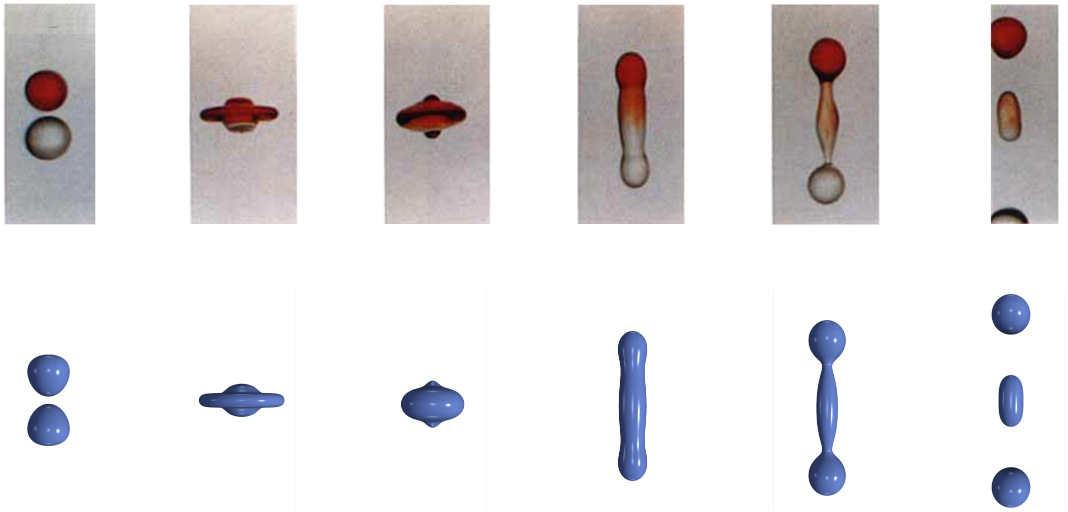

Figure 24: Head-on collision of liquid droplets, comparison between experiments with water droplets at $We = 40$ from Ashgriz & Poo (1990) and simulation results with oxygen droplets at $We = 80$ ($Re_l = 1100$) using the TIM

As it was the case in Fig. (23), a very strong agreement is obtained, in terms of behavior, between the simulation and the experiment. The relative sizes of the two departing and the stagnant satellite droplets are also well predicted.

5.2. *Periodic liquid jets*

5.2.1. *Case design*

A second application case is presented, motivated by the introduction of more complexity. The configuration consists in a symmetrical nitrogen mixing layer that takes the aspect of a liquid jet in its own vapor. The surrounding vapor is initially at rest whereas the liquid has a constant descending vertical velocity v_l. The simulations are performed on a regular cartesian mesh. The domain, as depicted in Fig. (25), is periodic vertically and non-reflecting boundary conditions are used on the left and right boundaries. The useful parameters used for the simulations are compiled in Tab. (10) where D_0 and w_0 are the reference jet diameter and interface width for the reference thickening coefficient $\mathrm{F}_0 = 1000$ and the mesh resolution $\Delta_{x0} = 0.133\ \mu\mathrm{m}$

Physics of Fluids

ACCEPTED MANUSCRIPT

This is the author's peer reviewed, accepted manuscript. However, the online version of record will be different from this version once it has been copyedited and typeset.

PLEASE CITE THIS ARTICLE AS DOI: 10.1063/5.0048715

AIP Publishing

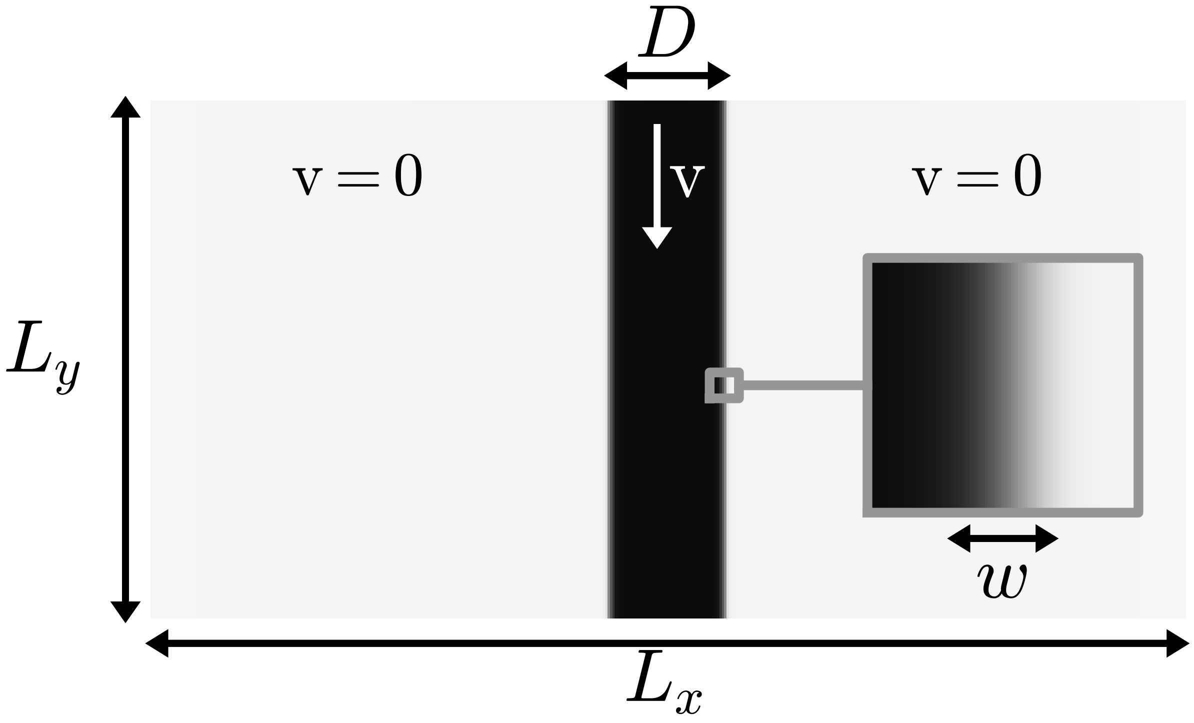

AIP Publishing

Physics of Fluids

ACCEPTED MANUSCRIPT

This is the author's peer reviewed, accepted manuscript. However, the online version of record will be different from this version once it has been copyedited and typeset.

PLEASE CITE THIS ARTICLE AS DOI: 10.1063/5.0048715

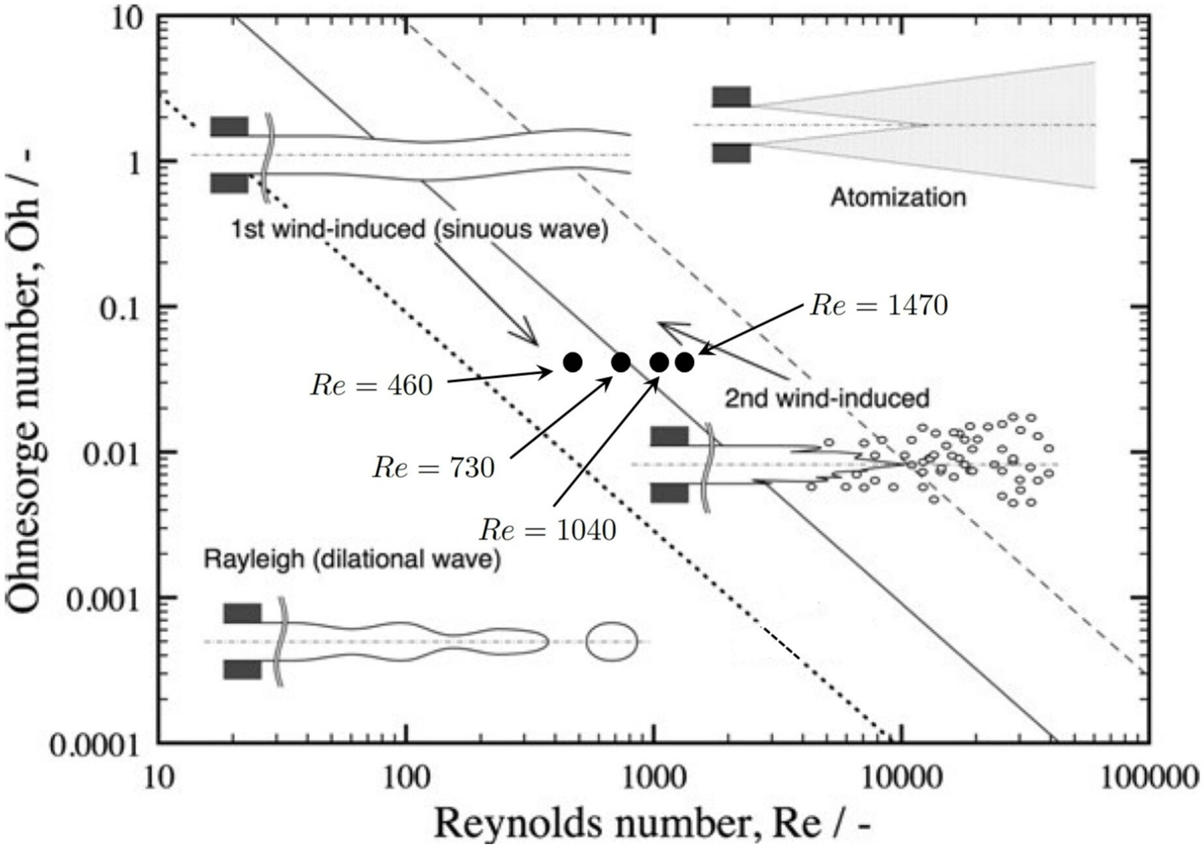

ACCEPTED MANUSCRIPT

Physics of Fluids

AIP Publishing

This is the author's peer reviewed, accepted manuscript. However, the online version of record will be different from this version once it has been copyedited and typeset.

PLEASE CITE THIS ARTICLE AS DOI: 10.1063/5.0048715

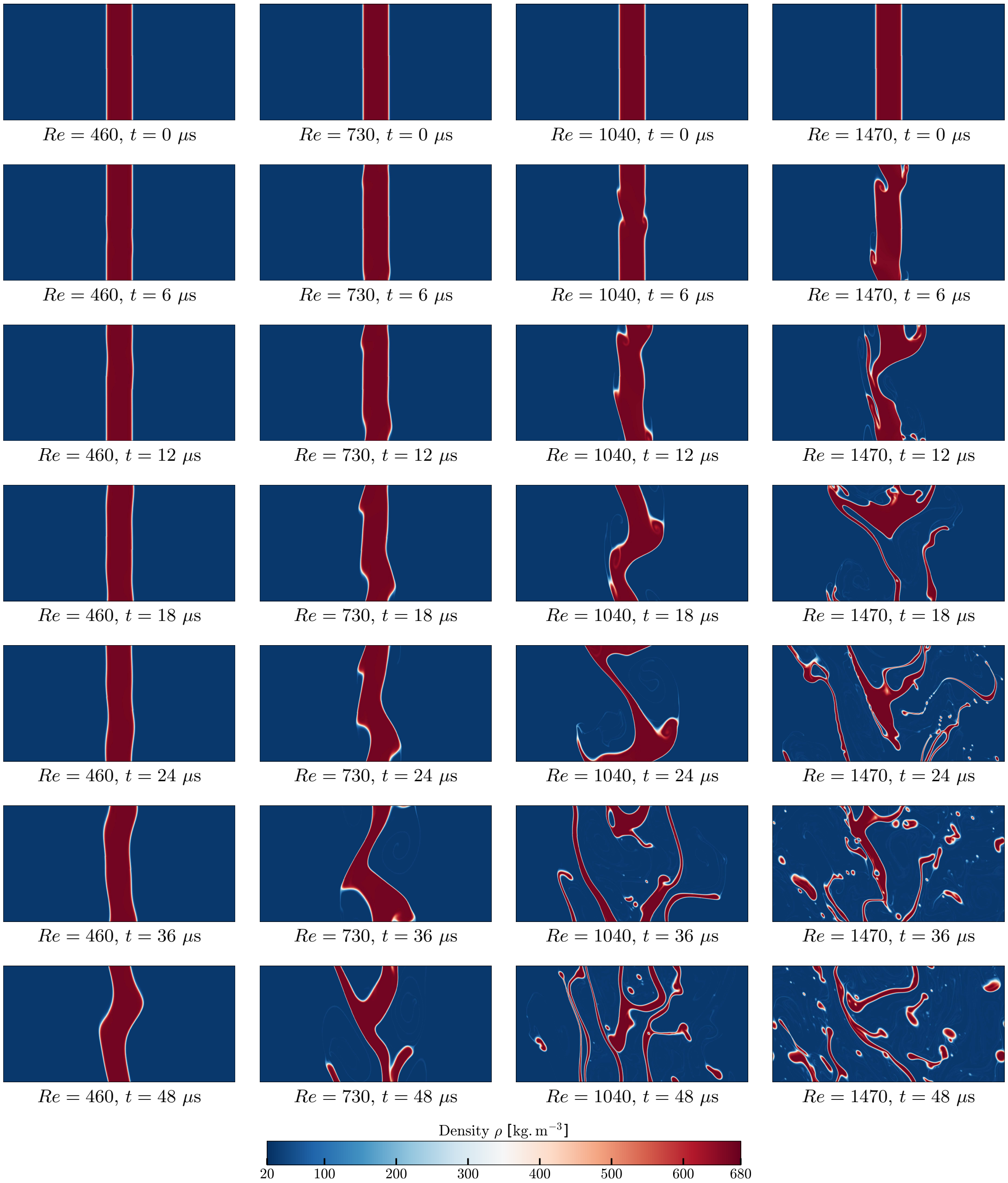

Figure 28: Evolution in time of the density profiles for two-dimensional periodic Nitrogen liquid jets in their vapor. Three cases have been carried out with the reference spatial resolution for different Weber numbers, from left to right: $Re = 460$, $Re = 730$, $Re = 1040$ and $Re = 1470$

ACCEPTED MANUSCRIPT

Physics of Fluids

AIP Publishing

This is the author's peer reviewed, accepted manuscript. However, the online version of record will be different from this version once it has been copyedited and typeset.

PLEASE CITE THIS ARTICLE AS DOI: 10.1063/5.0048715

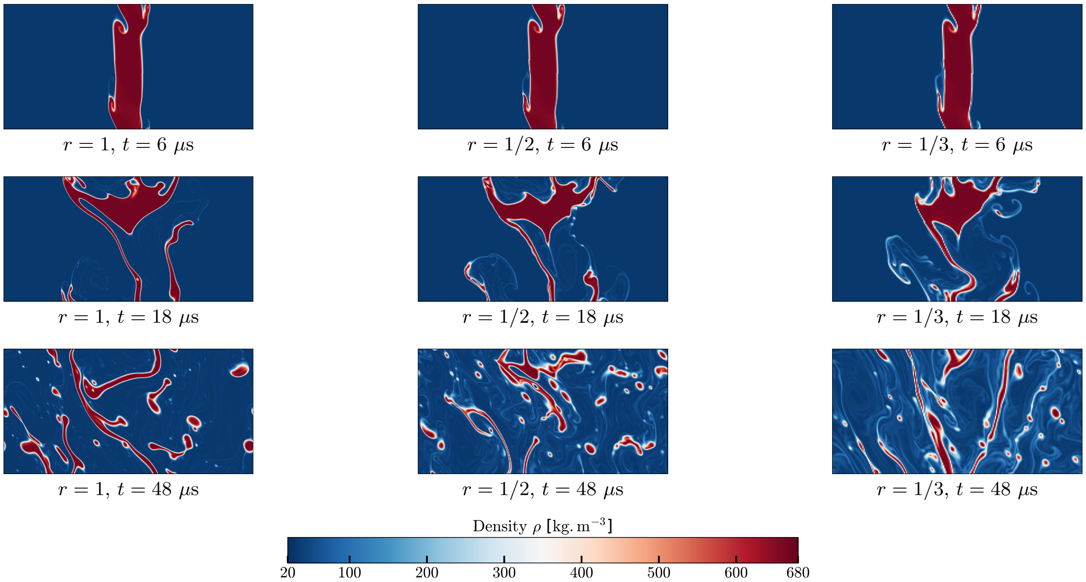

Figure 30: Evolution in time of the density profiles for two-dimensional periodic Nitrogen liquid jets in their vapor. Three cases have been carried out for $Re = 1470$ $(We = 4150)$ with the reference thickening factor $\mathrm{F} = 1000$ and three different spatial resolutions (*left*: reference $r = 1$, *center*: coarse $r = 1/2$, *right*: very coarse $r = 1/3$).

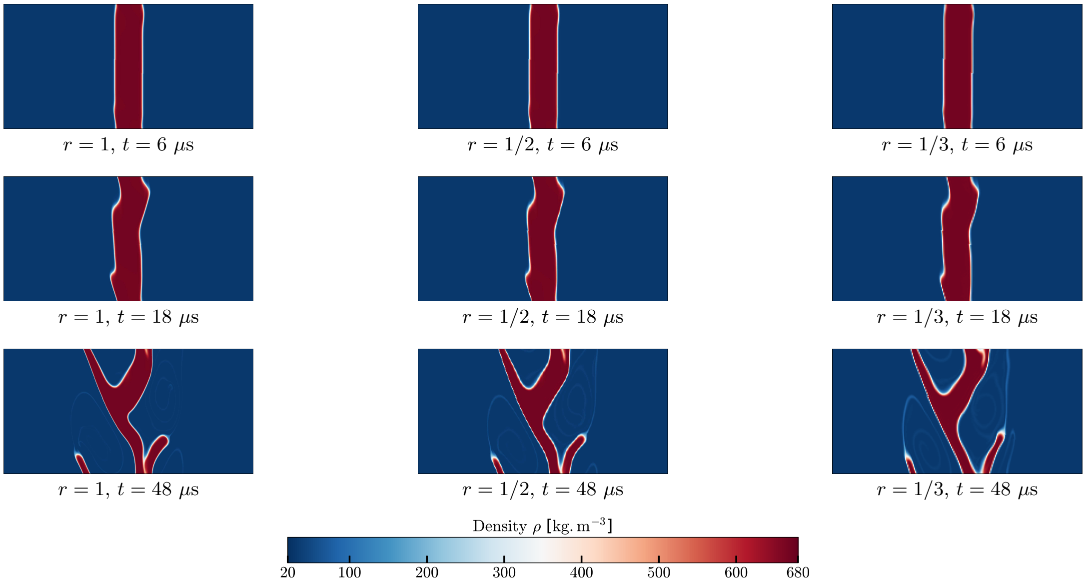

Figure 31: Evolution in time of the density profiles for two-dimensional periodic Nitrogen liquid jets in their vapor. Three cases have been carried out at $Re = 730$ $(We = 1030)$ with the reference thickening factor $\mathrm{F} = 1000$ and three different spatial resolutions (*left*: reference $r = 1$, *center*: coarse $r = 1/2$, *right*: very coarse $r = 1/3$)

ACCEPTED MANUSCRIPT

Physics of Fluids

This is the author's peer reviewed, accepted manuscript. However, the online version of record will be different from this version once it has been copyedited and typeset.

PLEASE CITE THIS ARTICLE AS DOI: 10.1063/5.0048715

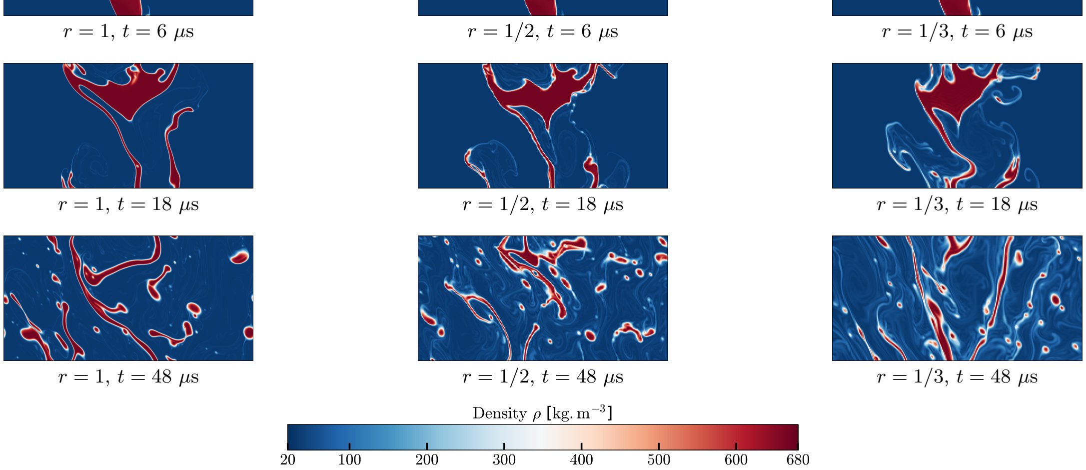

$r = 1,\ t = 6\ \mu$s
$r = 1/2,\ t = 6\ \mu$s
$r = 1/3,\ t = 6\ \mu$s

$r = 1,\ t = 18\ \mu$s
$r = 1/2,\ t = 18\ \mu$s
$r = 1/3,\ t = 18\ \mu$s

$r = 1,\ t = 48\ \mu$s
$r = 1/2,\ t = 48\ \mu$s
$r = 1/3,\ t = 48\ \mu$s

Figure 30: Evolution in time of the density profiles for two-dimensional periodic Nitrogen liquid jets in their vapor. Three cases have been carried out for $Re = 1470$ $(We = 4150)$ with the reference thickening factor $\mathrm{F} = 1000$ and three different spatial resolutions (*left*: reference $r = 1$, *center*: coarse $r = 1/2$, *right*: very coarse $r = 1/3$).

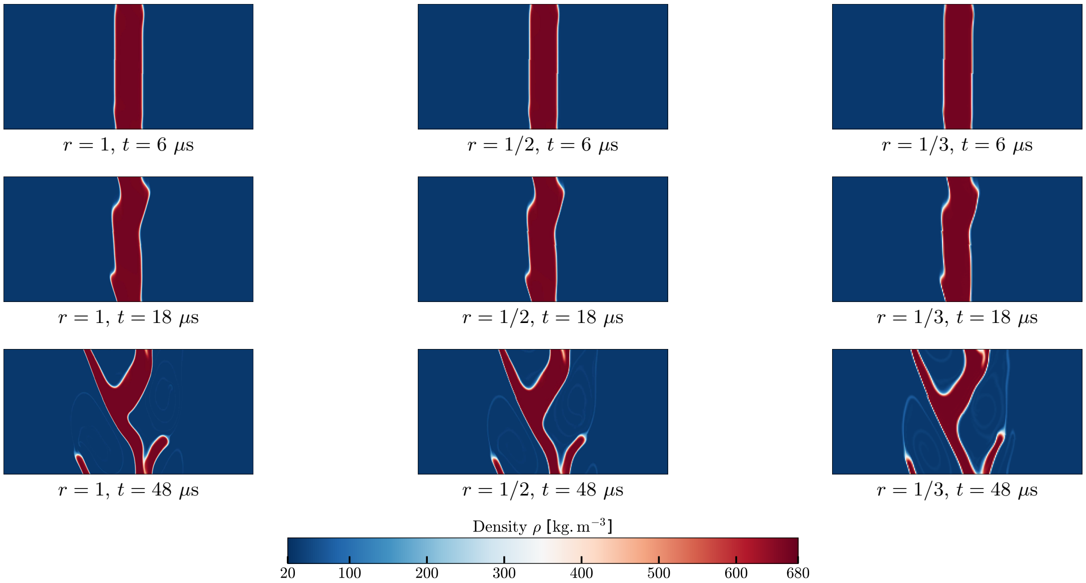

$r = 1,\ t = 6\ \mu$s
$r = 1/2,\ t = 6\ \mu$s
$r = 1/3,\ t = 6\ \mu$s

$r = 1,\ t = 18\ \mu$s
$r = 1/2,\ t = 18\ \mu$s
$r = 1/3,\ t = 18\ \mu$s

$r = 1,\ t = 48\ \mu$s
$r = 1/2,\ t = 48\ \mu$s
$r = 1/3,\ t = 48\ \mu$s

Figure 31: Evolution in time of the density profiles for two-dimensional periodic Nitrogen liquid jets in their vapor. Three cases have been carried out at $Re = 730$ $(We = 1030)$ with the reference thickening factor $\mathrm{F} = 1000$ and three different spatial resolutions (*left*: reference $r = 1$, *center*: coarse $r = 1/2$, *right*: very coarse $r = 1/3$)

Physics of Fluids ACCEPTED MANUSCRIPT

This is the author's peer reviewed, accepted manuscript. However, the online version of record will be different from this version once it has been copyedited and typeset.

PLEASE CITE THIS ARTICLE AS DOI: 10.1063/5.0048715

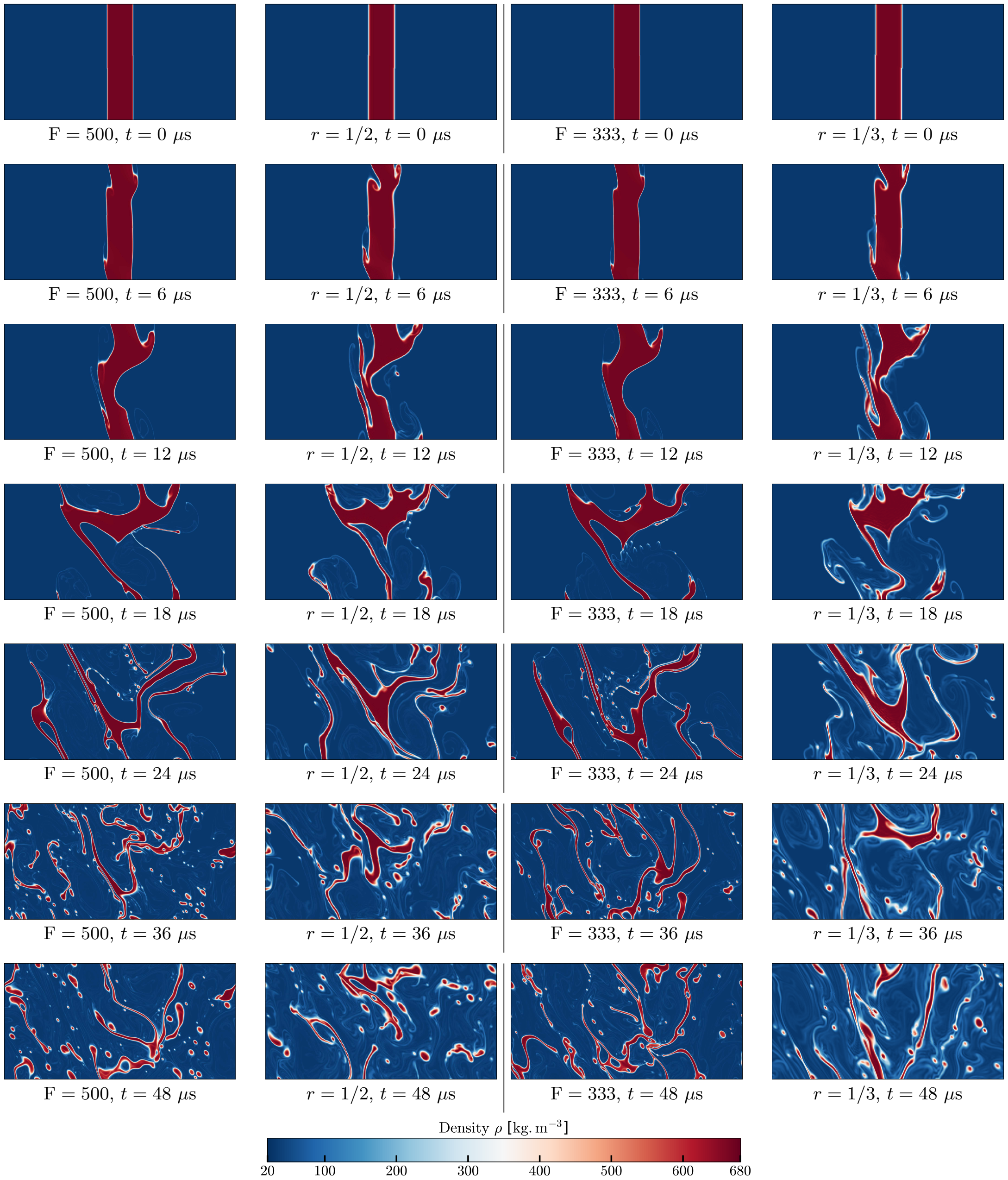
F = 500, $t = 0$ μs — $r = 1/2$, $t = 0$ μs — F = 333, $t = 0$ μs — $r = 1/3$, $t = 0$ μs

F = 500, $t = 6$ μs — $r = 1/2$, $t = 6$ μs — F = 333, $t = 6$ μs — $r = 1/3$, $t = 6$ μs

F = 500, $t = 12$ μs — $r = 1/2$, $t = 12$ μs — F = 333, $t = 12$ μs — $r = 1/3$, $t = 12$ μs

F = 500, $t = 18$ μs — $r = 1/2$, $t = 18$ μs — F = 333, $t = 18$ μs — $r = 1/3$, $t = 18$ μs

F = 500, $t = 24$ μs — $r = 1/2$, $t = 24$ μs — F = 333, $t = 24$ μs — $r = 1/3$, $t = 24$ μs

F = 500, $t = 36$ μs — $r = 1/2$, $t = 36$ μs — F = 333, $t = 36$ μs — $r = 1/3$, $t = 36$ μs

F = 500, $t = 48$ μs — $r = 1/2$, $t = 48$ μs — F = 333, $t = 48$ μs — $r = 1/3$, $t = 48$ μs

Figure 33: Evolution in time of the density profiles for two-dimensional periodic Nitrogen liquid jets in their vapor at $Re = 1470$ $(We = 4150)$. Two thickening factors and two mesh resolutions are used to get the same interface resolutions of five points (F = 500 / $r = 1/2$, *left images*) and three points (F = 333 / $r = 1/3$, *right images*)